ALMA MATER STUDIORUM – UNIVERSITA' DI BOLOGNA

SECONDA FACOLTA' DI INGEGNERIA
CON SEDE A CESENA

CORSO DI LAUREA
IN INGEGNERIA AEROSPAZIALE E ASTRONAUTICA
Classe 20

Sede di Forlì

TESI DI LAUREA

In Dinamica e Controllo d'Assetto LM

SAFETY SYSTEMS FOR SMALL SATELLITES

UNCONTROLLED TUMBLING MOTION

CANDIDATO
Marco Bosco

RELATORE
Prof. Paolo Tortora

CORRELATORE
Ing. Valentino Fabbri

Anno Accademico 2011/2012

Sessione II

It is difficult to say what it is impossible,

for the dream of yesterday is the hope of today

and the reality of tomorrow

(Robert H. Goddard)

Abstract

Titolo: Sistemi di Sicurezza per Piccoli Satelliti in Fase di Tombolomento

L'argomento di questo lavoro di tesi riguarda lo studio e la simulazione di nuove soluzioni per il sottosistema di determinazione e controllo d'assetto (ADCS) del micro-satellite ALMASat-EO in fase di progetto da parte di una collaborazione tra il laboratorio di microsatelliti e microsistemi spaziali dell'Università di Bologna e ALMASpace S.r.l..

In particolare, ci si è concentrati su una delle fasi di missione più critiche per un satellite che è la fase successiva al rilascio dal lanciatore fino alla stabilizzazione del satellite. Tale fase detta di tombolamento risulta particolarmente critica se il satellite si trova a ruotare con una velocità angolare elevata dovuta a separazioni non nominali dal lanciatore. Pertanto è stato studiato un sistema passivo di smorzamento delle velocità angolari che utilizza l'effetto di isteresi magnetica di barre realizzate in lega NiFe ad alta percentuale di Ni; un filtro di Kalman esteso (EKF) di stima della velocità angolare che fa uso delle letture di piccole celle solari posizionate su ogni faccia del satellite e un filtro di Kalman multi-rate per combinare tutte le misure disponibili per ricostruire in modo accurato (come da specifiche di missione) l'assetto del satellite.

Il sistema passivo di smorzamento è stato largamente studiato e validato tramite simulazioni nel lavoro di preparazione alla tesi e in questo lavoro è stato individuato il materiale specifico delle barre, contattando anche i fornitori, e sono state svolte ulteriori analisi su una possibile interazione magnetica con il sistema magnetico di controllo attivo. Gli algoritmi di stima della velocità angolare e dell'assetto sono invece stati implementati e sviluppati interamente in questo lavoro. Inoltre sono stati introdotti nel simulatore, sviluppato in ambiente MATLAB/Simulink, i modelli delle celle solari e del giroscopio a tre assi. Diverse simulazioni sono state poi eseguite per validare le nuove soluzioni introdotte nel ADCS e avere un'indicazione sull'accuratezza dei filtri di stima.

Table of Contents

List of Figures

List of Tables

1. Introduction

Non-nominal separation from the launcher or failures during the mission can lead the satellite to tumble with high angular velocity. In this case the available electric power can be limited since the solar arrays do not work properly and the batteries are the only source of power.

Thus, the aim of this work is to find safety systems in case of non-nominal separations. In order to achieve this goal, new solutions for the satellite Attitude Determination and Control Subsystem (ADCS) are considered. This field has been thoroughly explored since the dawn of the space age but new solutions are continuously studied and proposed in order to best achieve the several spacecraft mission goals. In order to investigate and validate the ADCS, several simulations are performed in MATLAB/Simulink. MATLAB is used in numerous institutions and space agencies and companies in order to model and analyze the real systems. The Simulink interface for MATLAB gives the ADCS designers a graphical interface to the simulation platform, and it is well suited for implementing easy-to-use simulation toolboxes.

The ADCS is designed for ALMASat-EO which is a satellite developed by the Microsatellite and Space Microsystems Laboratory of the University of Bologna in Forlì and the commercial spin-off of the same laboratory named ALMASpace S.r.l. ALMASat-EO belongs to micro-satellite class and it has $35\,kg$ of mass and $30 \times 30 \times 60\,cm$ of volume.

1.1. Background and Motivation

In February, 13th 2012, ALMASat-1, the first satellite of ALMASat family, was released in orbit by the VEGA launcher in its maiden flight. A non-nominal separation occurred due to a problem in the satellite separation mechanism leading the satellite to tumble with an unexpected high angular velocity. Then, due to the presence of maximum peak power trackers (MPPT) for power control and regulation, the solar arrays need to be illuminated for a few seconds before they

can supply electric power. Thus, ALMASat-1 could only be powered by batteries and it was switched to stand-by mode to save the limited available power. Two magnetic coils per axis were mounted on ALMASat-1 but they could not be used to damp the overall angular velocity since there was no sufficient power. The atmosphere drag torque can be considered the only way to dissipate the rotation kinetic energy. However this also leads to the satellite orbital decay. Thus, new solutions for the next micro-satellite ALMASat-EO ADCS need to be studied.

1.2. Thesis outline

The thesis is organized as follows:

Chapter 2. ALMASat-EO. ALMASat-EO mission goals and the satellite design is described. Then a description of attitude sensors as well as solar cells is given.

Chapter 3. Simulator. In order to study and analyze the satellite mission, a simulator tool is needed. Thus, in this section, the MATLAB/Simulink based simulation tool is described, with particular attention to some toolboxes.

Chapter 4. Hysteresis rods. The passive magnetic angular rate damping system, studied in the previous work, is briefly described and new considerations are developed.

Chapter 5. Rate estimation using solar cells. A new solution to estimate the satellite angular rate during tumbling motion is investigated and statistically validated by means of Monte Carlo simulations. A non-conventional arrangement of the solar cells is also studied and fully validated by means of Monte Carlo simulations.

Chapter 6. Attitude determination. Here, the attitude determination subsystem is studied. A multi-rate Kalman filter which combines all the available measurements is implemented in the simulator to test its performance and statistically validated by means of Monte Carlo simulations.

Chapter 7. Conclusion. Summary of the thesis with concluding remarks and recommendations for future work.

2. ALMASat-EO

Through the collaboration between the Microsatellite and Space Microsystems Laboratory of the University of Bologna in Forlì and the commercial spin-off of the same laboratory named ALMASpace S.r.l, in 2007 the ALMASat-EO microsatellite project started. The main goal of the mission is the manufacturing of a spacecraft for Earth Observation in particular to satisfy the increasing demand of weather monitoring and surveillance.

The main structure and orbital parameters are reported in Table 1:

ALMASat-EO	Value	Unit
Dimensions	30 × 30 × 60	cm
Mass	35	kg
Inertia matrix	$diag([0.951\ 0.97\ 0.946])$	kgm^2
Orbital height	686	km
Orbital eccentricity	0	°
Orbital RAAN	−23.5	°
Orbital inclination	98.161	°

Table 1. ALMASat-EO main structure and orbital parameters.

The main payload mounted on board ALMASat-EO is the optical system, able to take images of the Earth's surface with an area of about 150 km^2. The camera will be placed in a tray-based structure where the upper 6-trays will contain the main on-board equipment and the remaining portion will be equipped with the technological payloads. The Attitude and Orbit Determination and Control System (AODCS), the communication system and the On-Board computer and Data Handling (OBDH) represent the main subsystems, necessary to the guarantee spacecraft control and to accomplish the mission purposes.

The need to obtain images of the Earth requires observing the sub-satellite point under optimal lighting conditions. This is why the AODCS sub-system requirements are mainly due to the characteristics of the installed optical payload and its own working mode.

ALMASat-EO AODCS will include two pairs of sun sensors, two redundant three-axis magnetometers and one Earth sensor as spacecraft attitude sensors system, three pairs of orthogonal magnetic coils, and a set of four redundant momentum/reaction wheels as attitude control actuators. In addition, a cold-gas micro-propulsion system will be mounted on-board in order to modify the launch vehicle orbit and insert ALMASat-EO into its nominal orbit.

The on-board attitude sensors and actuators are managed by digital electronic boards entirely developed by the team. The AODCS is implemented in the On-Board Computer and will handle both the attitude reconstruction (by using the sensor readings) and attitude control functions (by controlling the actuators) [1]. Motivated by these challenging needs, a MATLAB/Simulink-based simulation tool has been developed in order to test the ADCS.

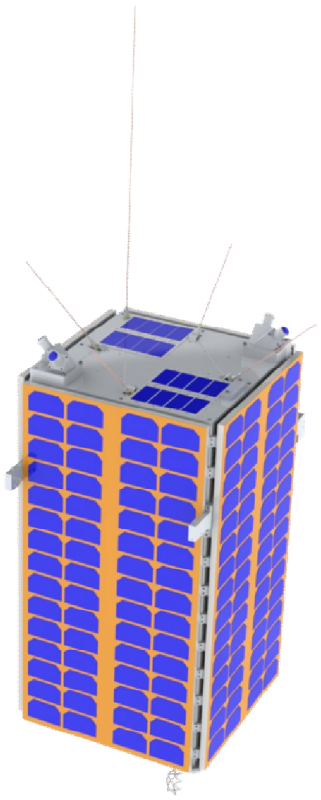

Figure 1. ALMASat-EO

2.1. Sensors

All presented attitude sensors, except the gyroscope, are reference sensors. Reference sensors give a vector to some object which position is known. The rotation between the local body frame, and the frame in which the known vector is given, can then be computed. With only a single measurement, the rotation around the measured vector is unknown. It is therefore necessary either to have two different measurements at least, or to use information from the past. The most common way to incorporate measurement history, is to combine the measurements in a Kalman filter [2]. In this case, the estimation of the angular velocity is required to propagate the attitude forward in time. It can be obtained using a three-axis gyroscope which is an inertial sensor. In Table 2, a summary of typical satellite sensors is reported. Sensors have continued to improve in performance while getting smaller and less expensive [3].

Sensor	Accuracy (deg)	Weight (kg)	Power (W)	Pros	Cons
Gyroscope (IMU)	0.003/hr to 1/hr	1 to 15	10 to 200	high bandwidth	expensive, drifts with time
Sun sensor	0.005 to 3	0.1 to 2	0 to 3	cheap, simple, reliable	no measurement in eclipse
Star sensor	0.0003 to 0.01	2 to 5	5 to 20	very accurate	expensive, heavy complex
Horizon sensor	0.1 to 1 (scanner) 0.1 to 0.25 (static)	1 to 4 0.5 to 3.5	5 to 10 0.3 to 5	accurate	orbit dependent, poor in yaw
Magnetometer	0.5 to 3	0.3 to 1.2	< 1	cheap, continuous coverage	low altitude only

Table 2. Typical ADCS Sensors.

2.1.1. Magnetometer

Magnetometers are widely used as spacecraft attitude sensors for a variety of reasons: they are vector sensors, providing both the direction and magnitude of magnetic field; they are reliable, lightweight, and have low power requirements; they operate over a wide temperature range and they have no moving parts. However, because the Earth's magnetic field strength decreases with distance from Earth as $1/r^3$, the use of magnetometers is generally limited to spacecraft below $1000\ km$ [4].

The magnetometer consists of three orthogonal sensor elements which measure the Earth's magnetic field in three axes in the sensor frame. If the magnetometer is aligned with the satellites axes, or the rotation between the body and sensor frame is known, the magnetic field in the body frame is obtained. The accuracy of the magnetometer is limited mainly by three factors: disturbance fields due to spacecraft electronics, modeling errors in the IGRF model and external disturbances such as ionospheric currents [2].

The mostly used magnetometers are induction magnetometers which are based on Faraday's law of magnetic inductance. An electromotive force, E is induced in a conducting coil placed in a time-varying magnetic flux, $d\phi_B/dt$ such that the line integral of E along the coil is the voltage, V:

$$V = \oint E \cdot dl = -\frac{d\phi_B}{dt}$$

The two types of induction magnetometers are search-coil and fluxgate magnetometers. In a search-coil magnetometer, a solenoidal coil of N turns surrounds a ferromagnetic core with magnetic permeability μ, and cross-sectional area A. The produced voltage is given by:

$$V = -AN\mu(dB_\perp/dt)$$

where $B_\perp$ is the field component along the solenoidal axis [4].

The fluxgate magnetometer is a transducer which converts a magnetic field into an electric voltage. Fluxgates are configured with windings through which a current is applied. If there is no component of the magnetic field along the axis of the winding, the flux change detected by the winding is zero. If there is a field component present,

the flux in the core changes from a low level to a high level when the material goes from one saturation level to another. From Faraday's law, a changing flux produces a voltage at the terminals of the winding proportional to the rate of change of the flux [2].

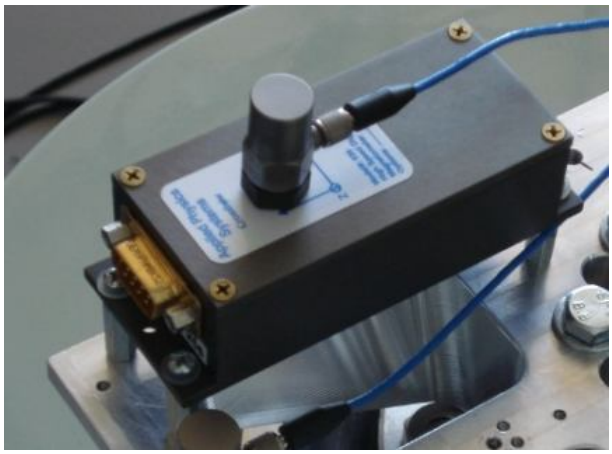

Figure 2. ALMASat-EO magnetometer

2.1.2. Sun sensor

Sun sensors are the most widely used sensor type for attitude determination. The Sun sensor owes its versatility to several factors [4]. Unlike the Earth, the angular radius of the Sun is nearly orbit independent and sufficiently small ($0.267°$ at $1\ AU \cong 1.5 \cdot 10^8\ km$) that for most applications a point-source approximation is valid. Moreover, the Sun is sufficiently bright to permit the use of simple, reliable equipment with minimal power requirements. Lastly, Sun sensors measurements are also used to protect sensitive equipment, to provide a reference for on-board attitude control, and to position solar power arrays. Sun sensors requires a clear field-of-view and thus, they are usually mounted near the ends of the spacecraft to obtain an unobstructed filed-of-view. Obviously, Sun sensor measurements are not available during eclipse and this is the only drawback of this sensor. There are three basic classes of Sun sensors: analog sensors, Sun presence sensors and digital sensors.

Analog sensors are frequently called cosine detectors because they are based on the sinusoidal variation of the output current of a silicon solar cell with Sun angle. However, for high incidence angles, the output current is not accurately described by a

sinusoidal function. Thus, sensor calibration is required to obtain an accurate relation between the Sun angle and the output current. Moreover, these sensors are affected by temperature variations and albedo effect.

Digital sensors provide an encoded, discrete output which is a function of the Sun angle. The Sun image is refracted by a material of index of refraction n, which may be unit, and illuminates a pattern of slits. The slits are divided into a series of rows with a photocell beneath each row. The orientation of the Sun is provided using a Gray code. The accuracy of these sensors depends on the number of bits.

Sun presence detectors do not provide a Sun angle measurement, they only provide a constant output signal whenever the Sun is in the field-of-view of the sensor.

The Sun sensor used for ALMASat mission is an analogic Sun sensor providing a digital output (see Figure 3). It has a large filed-of-view ($130°$) and it is realized using commercial components and hence, it is a low-cost sensor.

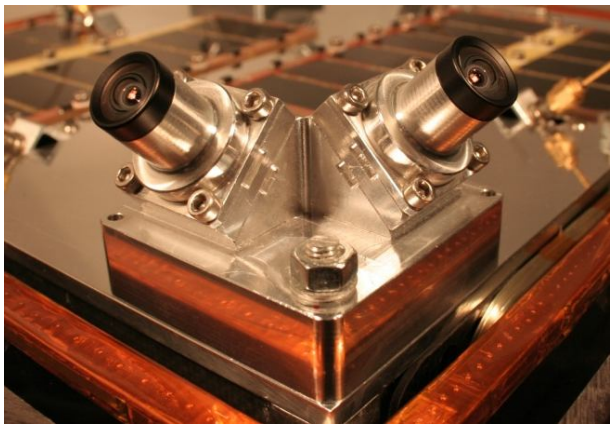

Figure 3. ALMASat-EO Sun sensor

2.1.3. Earth horizon sensor

Earth horizon sensors determine where the Earth is relative to the spacecraft. Since, to a near Earth satellite, the Earth covers up to 40% of the sky, detecting only the presence of the Earth is normally insufficient; thus, they are designed to locate the Earth's horizon. The majority of these sensors are infrared devices that detect the contrast between the cold of deep space and the heat of the Earth's atmosphere, exploiting the narrow $14 - 16\ \mu m$ CO_2 band. They are unaffected by night or by the

presence of terminator, they avoid reflection problems and the Sun interference problems are also reduced in the infrared. However, albedo sensors have some advantages over the infrared sensors, including lower cost, faster response time and higher signal-to-noise ratio because the radiated intensity is higher in the visible spectrum than in the infrared.

Most horizon sensors consist of four basic components: a scanning mechanism, an optical system, a radiance detector and signal processing electronics [4]. They are normally categorized by the scanning mechanism: there are body-mounted horizon sensors and scanning horizon sensors. The former, also called static horizon sensors, are simple narrow field-of-view fixed-head types, used on spinning spacecraft to measure Earth phase and chord angles which, together with orbit and mounting geometry, define two angles to the nadir vector.

Scanning horizon sensors use a rotating mirror or lens to replace the spinning spacecraft body [3]. The optical system of a horizon sensor consists of a filter to limit the observed spectral band and a lens to focus the target image on the radiance detector. Radiance detectors used to detect the presence of a horizon and they are based on the operating principles of the thermistor, like a bolometer, thermocouple, like a thermopile, or pyroelectric crystal, like pyroelectric detectors.

The sensor field-of-view scans across the Earth disc and gives outputs corresponding to the Earth-to-space and space to Earth discontinuities. An automatic threshold detection circuit, wherein the threshold of edge detection is kept at an optimum percentage of the peak signal, is used to minimize the errors in the measurement of the scanned Earth chord width. The measurements given by the Earth horizon sensor are based on the following equations:

$$\cos\rho = \cos\gamma\cos\eta + \sin\gamma\sin\eta\cos(\Omega/2)$$

$$\Omega = \omega(t_{LOS} - t_{AOS})$$

where ρ is the Earth angular radius, γ is the sensor mounting angle, η is the nadir angle, ω is the sensor spin rate, t_{LOS} and t_{AOS} are the measured loss-of-signal (i.e. light-to-dark transition) and acquisition-of-signal (i.e. dark-to-light transition) time, respectively.

Figure 4. ALMASat-EO FLIR TAU thermal sensor

2.1.4. Gyroscope

Gyroscope is an inertial sensor that measures angular rotation about its input axis with respect to inertial space. The sensing of such motion could utilize the angular momentum of a spinning rotor, the Coriolis effect on a vibrating mass, or the Sagnac effect on counter-propagating light beams in a ring laser or an optical fiber-coil [5].
Recently, due to the improving performance of Micro-ElectroMechanical Systems (MEMS) sensors, there has been increased interest in using MEMS gyroscopes in ADCS systems. MEMS technologies provide a mean to interface the digital electronic world, dominated by the integrated-circuit, IC, with the analog physical world. MEMS gyroscopes have advantages of being low-cost, light mass, and low power consumption. In the case of employing MEMS gyroscopes in ADCS, several challenges arise. Significant scale factors, nonlinearities, misalignment, noise and temperature varying biases currently limits use for high precision applications. Thus, precisely modeling and compensating for these errors is very important.

2.2. Solar cell

Solar cells functioning is based on the photovoltaic effect, consisting in an energy conversion process which generates electrical energy from light energy. The

explanation relies on ideas from quantum theory. Light is made up of packet of energy, called photons, whose energy depends only upon the frequency, or color, of the light. The energy of visible photons is sufficient to excite electrons, bound into solids, up to higher energy levels where they are more free to move. The solar cell contacts (bus bar) drive the excited electrons through an external circuit before they can relax.

The solar cell can be considered as a two terminal device which conducts like a diode in the dark and generates a voltage (photovoltage) when charged by the Sun. It is a thin slice of semiconductor material and the surface is treated to reflect as little visible light as possible and hence, it appears dark blue or black. A pattern of metal contacts is imprinted on the surface to make electrical contact (fingers).

The photocurrent generated by a solar cell under illumination at short circuit is dependent on the incident light. To relate the photocurrent density, J_{sc}, to the incident spectrum, we need the cell's quantum efficiency, QE. $QE(E)$ is the probability that an incident photon of energy E will deliver one electron to the external circuit. Then:

$$J_{sc} = q \int b_s(E) QE(E) dE$$

where $b_s(E)$ is the incident spectral photon flux density, QE is the number of photons of energy in the range E to $E + dE$ which are incident on unit area in unit time and q is the electronic charge. QE depends upon the absorption coefficient of the solar cell material, the efficiency of charge separation and the efficiency of charge collection in the device but it does not depend on the incident spectrum. Figure 5 shows a Gallium-Arsenide (GaAs) solar cell QE spectrum in comparison with the spectrum of solar photons. QE and spectrum can be given as functions of either photon energy or wavelength, λ. Energy is a more convenient parameter for the physics of solar cells [6]. The relationship between E and λ is defined as:

$$E = \frac{hc}{\lambda}$$

where $h = 6.626 \cdot 10^{-34}\ J$ is the Planck's constant and $c = 2.9979 \cdot 10^{8}\ m/s$ is the speed of light in vacuum.

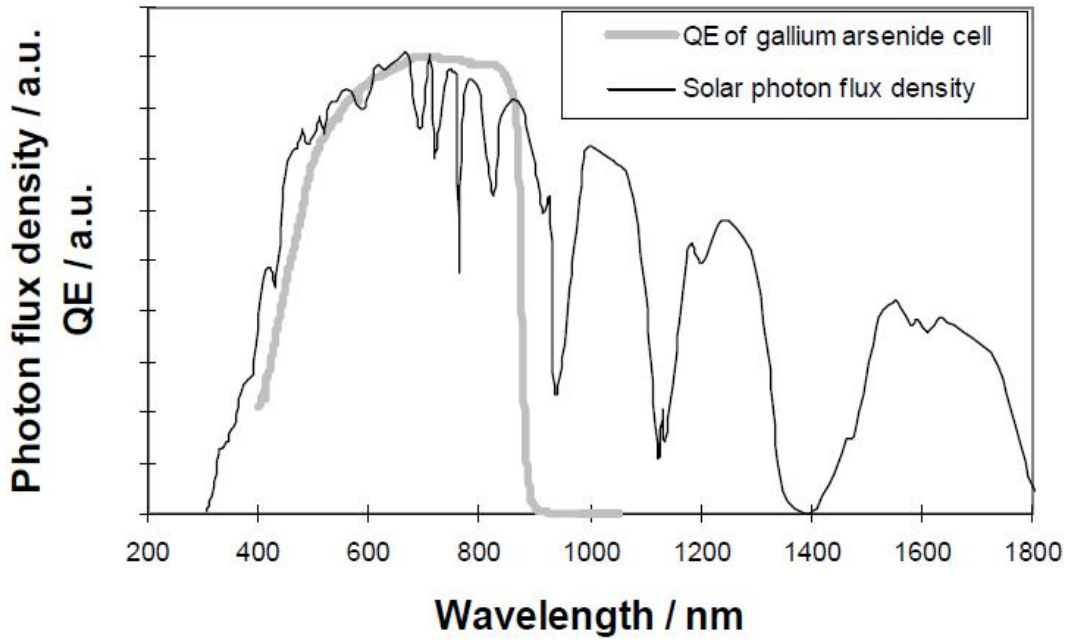

Figure 5. Quantum efficiency of GaAs cell compared to the solar spectrum. The vertical scale is in arbitrary units, for comparison. The short circuit photocurrent is obtained by integrating the product of the photon flux density and QE over photon energy. It is desirable to have a high QE at wavelengths where the solar flux density is high [6].

The solar cell can be modeled as a current generator in parallel with an ideal diode and series and shunt resistances (see Figure **6**) to take into account power dissipation through the resistance of the contacts and through leakage currents around the sides of the device (see [7] and [8]).

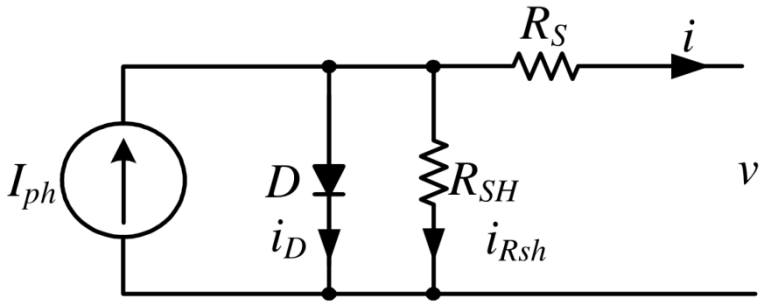

Figure 6. Equivalent circuit of a solar cell

This equivalent circuit can be simplified by neglecting the shunt resistor (see [9] and [10]). In [10], an improved model of a solar cell that make use only of parameters provided by manufacturers datasheets and, moreover, does not require any numerical methods, is developed. The current is given by the difference between the short circuit

current, I_{sc}, and the dark current, I_{dark}, which can be expressed as a function of the voltage, V:

$$I = I_{sc} - I_{dark}(V) = I_{sc}\left[1 - c_1\left(e^{\frac{V}{c_2 V_{oc}}} - 1\right)\right]$$

Conversely, the voltage can be expressed as a function of the current as:

$$V = c_2 V_{oc} ln\left(1 + \frac{\left(1 - \frac{I}{I_{sc}}\right)}{c_1}\right)$$

where V_{oc} is the open circuit voltage and c_1 and c_2 are coefficients:

$$c_1 = \left(1 - \frac{I_{MPP}}{I_{sc}}\right) e^{-\frac{V_{MPP}}{c_2 V_{oc}}}$$

$$c_2 = \left(\frac{V_{MPP}}{V_{oc}} - 1\right) / ln\left(1 - \frac{I_{MPP}}{I_{sc}}\right)$$

where I_{MPP} and V_{MPP} are the maximum power point current and voltage respectively. The solar cell power, P, is given by:

$$P = I \cdot V$$

P reaches a maximum at the cell's maximum power point. This occurs at voltage V_{MPP} and current I_{MPP} as shown in Figure 7. The fill factor, FF, is defined as the ratio:

$$FF = \frac{I_{MPP} V_{MPP}}{I_{sc} V_{oc}}$$

and it describes the 'squareness' of the $I - V$ curve.

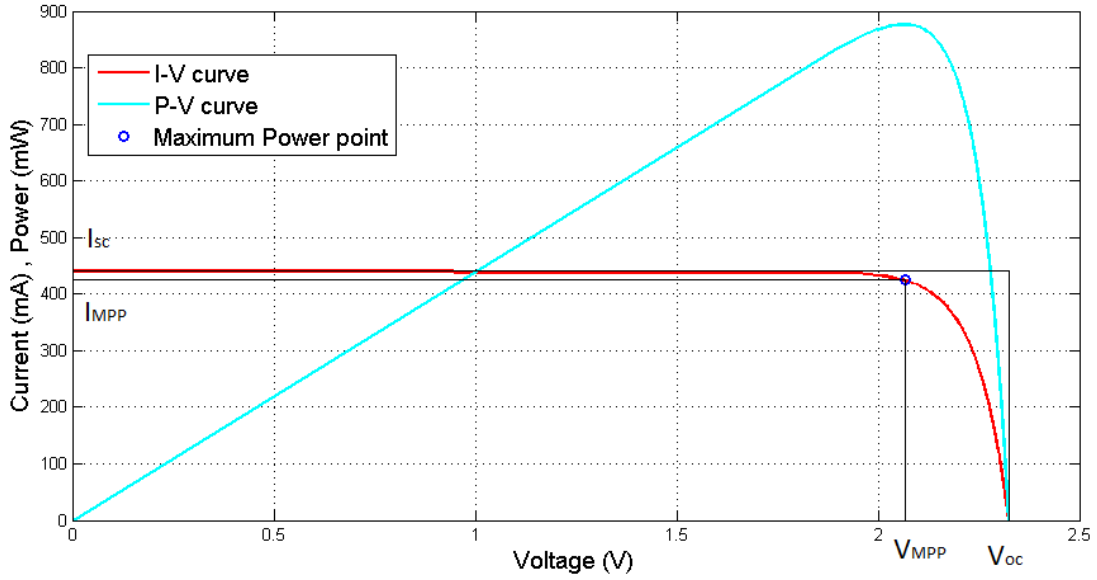

Figure 7. Solar cell current voltage (red) and power voltage (cyan) characteristics. Power reaches the maximum at V_{MPP} The maximum power is given by the area of the inner rectangle. The outer rectangle has an area equal to $I_{SC}V_{OC}$. If the fill factor was equal to 1, the current voltage curve would follow the outer rectangle.

The efficiency, η, of the cell is the ratio between the maximum power generated by the solar cell and the solar flux normal to the cell, E, times the surface area, S:

$$\eta = \frac{I_{MPP}V_{MPP}}{E \cdot S}$$

Solar cells convert radiant flux to electrical power and can be used to estimate the angle between the normal vector to the cell plane and the Sun line of sight (LOS) vector, by measuring the intensity per area on the solar cell surface, which is related to the angle of incident irradiance:

$$P(\alpha) = \eta S E \cos\alpha$$

where $P(\alpha)$ is the electrical power generated by the solar cell, η is the solar cell efficiency, S is the solar cell surface area, E is the incident irradiance and α is the angle of incident irradiance.

Solar cells are typically mounted such that measurements are available in six directions which are opposite facing in pairs. Typically a minimum of six solar cells are used, looking in the positive and negative directions of each axis in the body reference frame.

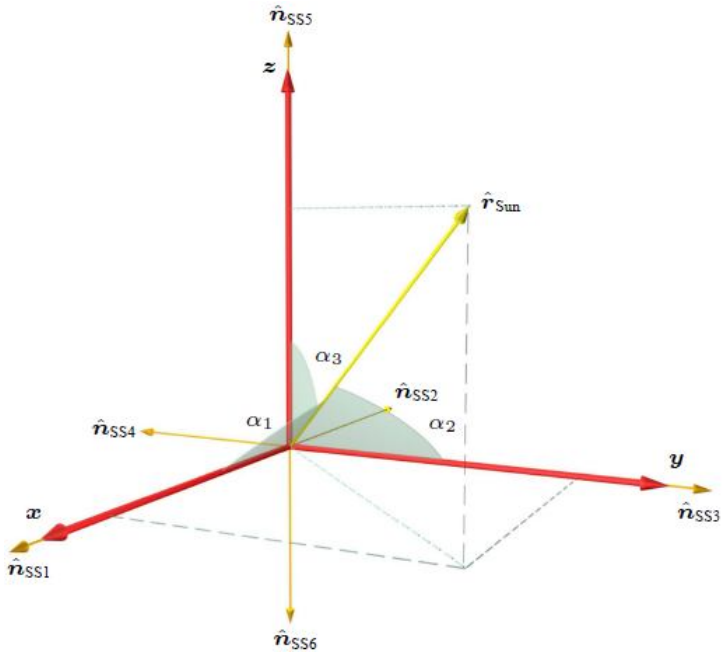

Figure 8. Projections of the sun LOS vector measured by solar cells mounted in opposite looking directions along three orthogonal axes.

Figure 8 shows the geometry of the Sun LOS vector $\hat{r}_{Sun}$ in a configuration, where six solar cells are mounted in pairs in opposite directions and along three orthogonal axes. The solar cells are represented by the normal vectors $\hat{n}_{SSi}$ of each cell SS1 through SS6.

Two solar cells used as coarse Sun sensor will be mounted on each ALMASat-EO face. They are 28% triple junction GaAs solar cell produced by AzurSpace. The datasheet is reported in Appendix A and the main parameters used in the simulator for solar cells are reported in Table 3.

Solar cell	Value	Unit
Average Short Circuit Current I_{sc}	441.1	mA
Short Circuit Current Temperature Gradient $\Delta I_{sc}/\Delta T$ ↑	0.28	$mA/$℃
Reference Temperature T_{ref}	28	℃
Calibrated Irradiance E_{cal}	1367	W/m^2
Surface Area	26.31	cm^2

Table 3. ALMASat-EO solar cell main parameters. They refer to beginning of life (BOL). Properties degradation due to aging are reported in the datasheet.

Solar cells are characterized by the current-voltage, $I-V$ and power-voltage, $P-V$ curves. These curves are then parameterized by angle of the incident irradiance (see

Figure 9), temperature (see Figure 10) and aging (see Figure 11) of the solar cell. In fact, solar cell performance is degraded by space radiation made up of high energy particles which hit the solar cells reducing their efficiency. Figure 9 clearly shows the decrease of short circuit current, I_{sc}, when the angle of incidence increases. Figure 10 shows the slight increase of I_{sc} with temperature and the decrease of open circuit voltage, V_{oc}, with temperature. Thus, choosing solar cells in short circuit mode reduces the solar cell output dependence on temperature. Finally, Figure 11 shows the solar cell $I - V$ curve at beginning of life (BOL) and at end of life (EOL).

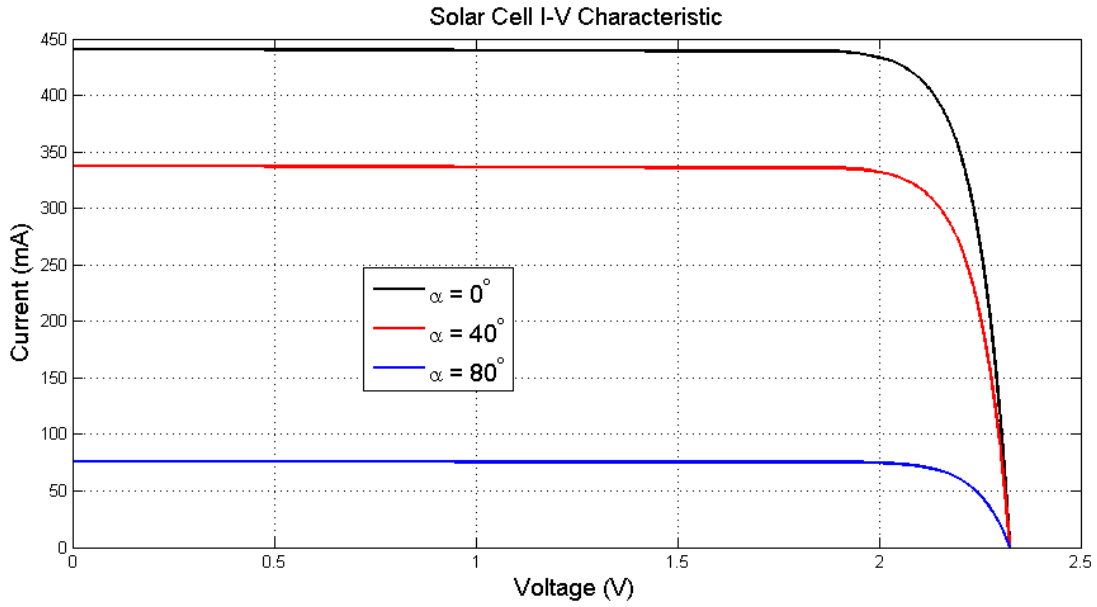

Figure 9. Solar cell current voltage curve dependence on angle of incident irradiance.

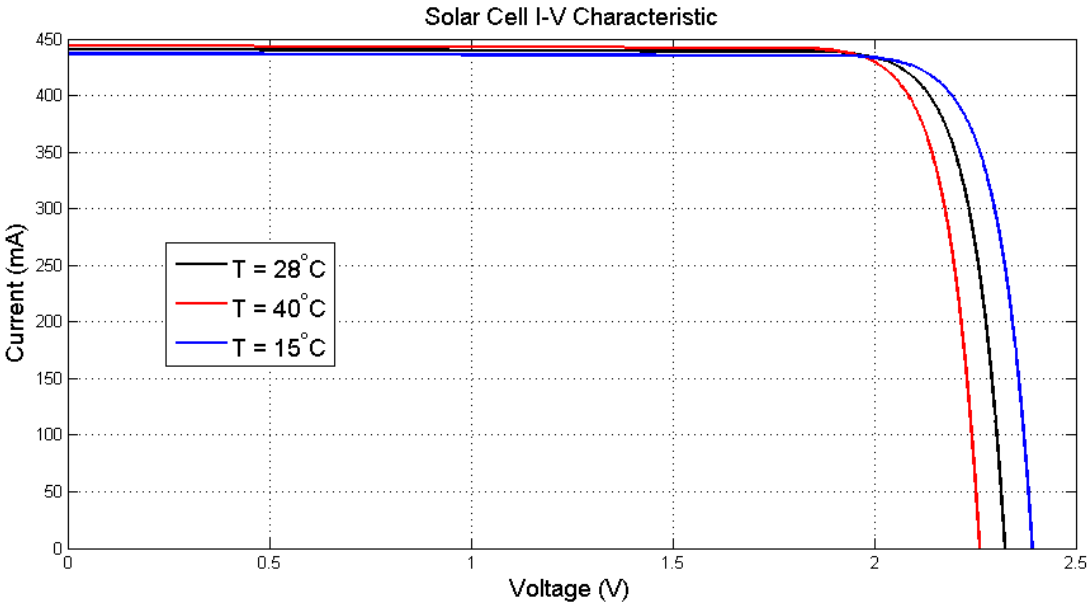

Figure 10. Solar cell current voltage curve dependence on temperature.

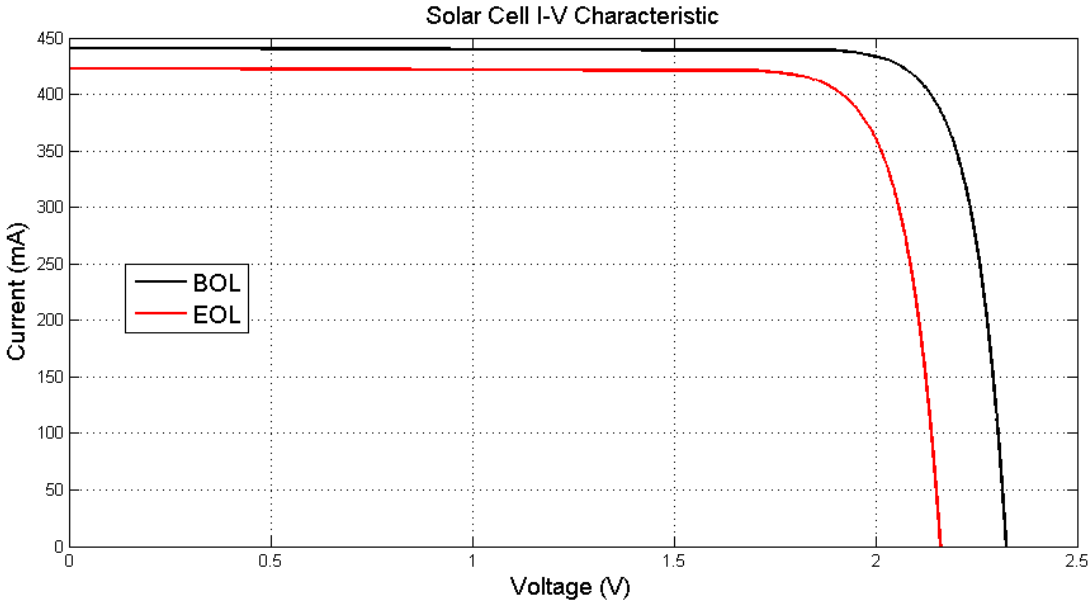

Figure 11. Solar cell current voltage curve dependence on aging.

3. Simulator

The simulator is MATLAB/Simulink-based software and several mathematical models are implemented in order to simulate the space environment. Also, a numerical integrator is used to propagate the orbital motion and to predict the ALMASat-EO attitude. The simulator events are managed by a finite state machine and each state represents a mission event.

The attitude dynamics is described by Euler's equation and the kinematic equation for the quaternion. The former is used to calculate the true satellite angular velocity, ω:

$$J\dot{\omega} = M_{ext} - \frac{dh}{dt} - \omega \times (J\omega + h)$$

where M_{ext} is the total amount of external torques acting on the satellite (gravity gradient, aerodynamic, magnetic and solar radiation pressure torque), h is the net angular momentum due to the rotation of the reaction or momentum wheels relative to the spacecraft and J is satellite inertia matrix.

The kinematic equation for the quaternion q describes the satellite attitude:

$$\dot{q} = \frac{1}{2}\Omega q$$

where Ω is a 4×4 matrix containing the satellite angular velocity components in the inertial reference frame:

$$\Omega = \begin{bmatrix} 0 & r & -q & p \\ -r & 0 & p & q \\ q & -p & 0 & r \\ -p & -q & -r & 0 \end{bmatrix}$$

with $\omega = [p\ q\ r]$.

On-board orbit propagation is performed by SGP4 model (see [11]). It was developed by Ken Cranford in 1970 and is used for near-Earth satellites (the orbital period of ALMASat-EO is around 98 minutes). Simplified perturbations models are a set of five mathematical models (SGP, SGP4, SDP4, SGP8 and SDP8) used with two-line mean element (TLE) sets, produced by NORAD, to compute satellite orbital position and velocity. Simplified General Perturbations (SGP) models apply to near earth objects

with an orbital period of less than 225 minutes; conversely, Simplified Deep Space Perturbations (SDP) models apply to objects with an orbital period greater than 225 minutes. These models consider secular and periodic variations due to Earth oblateness, solar and lunar gravitational effects, gravitational resonance effects, and orbital decay using a drag model.

The numerical integrator characterizes the analysis output in terms of accuracy and precision. A 4^{th}-order Runge-Kutta (RK4) method has been selected in the MATLAB/Simulink-based simulator. A fixed-step size solver has been used in simulations in order to limit the step-size and improve the accuracy of the results during the mission in order to fully describe the orbital dynamics and the attitude motion of ALMASat-EO.

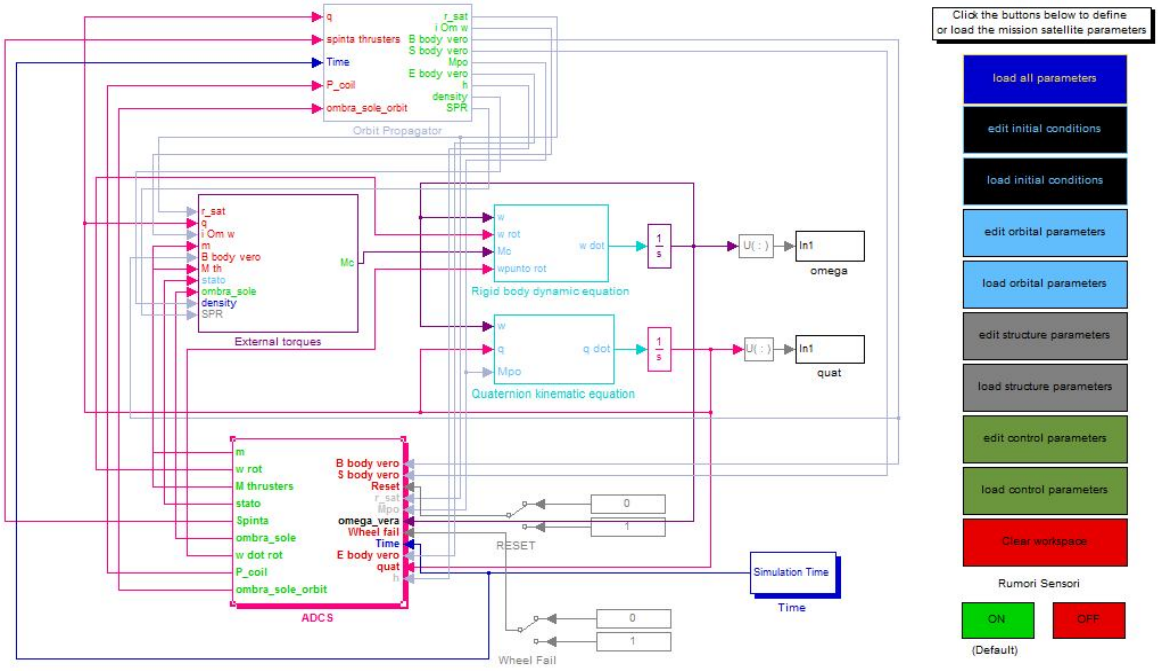

Figure 12. ALMASat-EO simulator

3.1. Reference systems

Three main reference systems are employed [1]:

- an ECI (Earth Centered Inertial) reference system (C1, C2, C3), with: C1, C2 in the equatorial plane and C3 parallel to the Earth's spin axis;

- an orbital reference system (τ, h, r) where: the angular momentum, $h = r \times v$ is directed along the positive orbit normal, r is the radial direction from the centre of the Earth to the spacecraft and τ is defined as $h \times r$, in the orbital plane, in the same direction of the velocity vector v for circular orbits (and of the velocity vector at perigee and apogee for eccentric orbits);
- a body-fixed reference system on ALMASat-EO, so that X is the longitudinal axis aligned to the satellite velocity for a circular orbit, Y is aligned to the orbit normal and Z is aligned to the nadir.

The rotation matrix between the reference systems 1 and 2 aforementioned is immediate once the spacecraft centre of mass position is known by numerical integration of the equations of motion. The rotation matrix between the reference systems 2 and 3 assumes that if the ALMASat-EO body axes are aligned to the orbital axes, the rotation matrix reduces to the unity matrix ($X \equiv \tau$, $Y \equiv h$ and $Z \equiv r$). By introducing the Euler angles 1-2-3 (Roll = φ, Pitch = ϑ and Yaw = ψ) one can represent all rotations of ALMASat-EO with respect to the orbital reference frame.

3.2. Earth magnetic field model

The Earth magnetic field, B can be expressed as the gradient of a scalar potential, V:

$$B = -\nabla V$$

where V can be conveniently expressed in spherical harmonics as [4]:

$$V(r, \theta, \phi) = a \sum_{n=1}^{k} \left(\frac{a}{r}\right)^{n+1} \sum_{m=0}^{n} (g_n^m \cos m\phi + h_n^m \sin m\phi) P_n^m(\theta)$$

where a is the equatorial radius of the Earth; g_n^m and h_n^m are called Gaussian coefficients; r, θ and ϕ are the geocentric distance, co-elevation, and east longitude from Greenwich; and $P_n^m(\theta)$ are the associated Legendre functions. The $n = 1$ terms are called dipole; the $n = 2$ terms are called quadrupole and so on. One set of

Gaussian coefficients to degree $n = 8$ and order $m = 8$ comprises the International Geomagnetic Reference Field (IGRF).

3.3. Magnetometer model

The magnetometer model takes the Earth's magnetic field vector, computed from IGRF model and rotated in the body reference frame by the attitude matrix, and adds noise to create a realistic measure, $\tilde{B}_b$. A bias vector term due to the presence of permanent magnets or possible magnetic fields created by on-board electronics can be considered. The output noise level of the magnetometer in root mean square (*rms*) is given by the datasheet and modeled by a zero-mean Gaussian random noise with the specified variance. The misalignment and scale factor (given in the datasheet) inaccuracies are added with a gain block which is $I_{3\times3} + G$, where the diagonal values of G are the percent error in scale factor and the off-diagonal values of G are the percent error of misalignment. A saturation block is used to limit the dynamic range of the magnetometer. Temperature dependency should not be included in the model, if the chosen sensor has internal temperature compensation.

3.4. Sun position propagator

In order to compute on-board the Sun direction vector in an inertial reference frame for attitude estimation, a less computational burdensome solution than a Keplerian propagator is required. For small eccentricities, the true anomaly, ν may be expressed directly as a function of the mean anomaly, M by a power series expansion derived by Ruppe [4]:

$$\nu = M + 2e\sin M + \frac{5}{4}e^2\sin 2M + \mathcal{O}(e^3)$$

This expression is derived combining Kepler's equation:

$$M = E - e\sin E$$

with Gauss' equation:

$$\tan\left(\frac{\nu}{2}\right) = \left(\frac{1+e}{1-e}\right)^{1/2} \tan\left(\frac{E}{2}\right)$$

where E is the eccentric anomaly.

3.5. Eclipse model

In order to model properly the satellite mission conditions, determining the period when the spacecraft is in eclipse is essential. In fact, during this period Sun sensor readings are not available, the solar cells and arrays output currents are zero and the satellite temperature drops. Thus, eclipse can influence attitude and angular rate estimation and batteries are the only power source.

To determine the conditions under which eclipse occurs, first the length C of the shadow cone for the Earth is computed as:

$$C = \frac{R_\oplus \cdot S}{(R_\odot - R_\oplus)} = 1.385 \cdot 10^6\ km$$

where $R_\oplus = 6378.140\ km$ is the mean radius of the Earth, $R_\odot = 6.9599 \cdot 10^5\ km$ is the radius of the photosphere (i.e. the visible surface) of the Sun and $S = 1\ AU \cong 1.5 \cdot 10^8\ km$ is the distance from the Earth to the Sun.

To develop specific eclipse conditions, let $r_\odot$ be the versor from the spacecraft to the center of the Sun and $D_\odot$ the corresponding distance and let $r_\oplus$ be the versor from the spacecraft to the center of the Earth and $D_\oplus$ the corresponding distance. The angular radius of the Sun, $\rho_\odot$, the angular radius of the Earth, $\rho_\oplus$, and the angular separation, θ, between the Sun and the Earth as viewed from the spacecraft, are given by:

$$\rho_\odot = \sin^{-1}(R_\odot / D_\odot)$$

$$\rho_\oplus = \sin^{-1}(R_\oplus / D_\oplus)$$

$$\theta = \cos^{-1}(r_\odot \cdot r_\oplus)$$

The total eclipse condition can be then expressed as [4]:

$$S < D_{\odot} \text{ or } D_{\odot} < S + C \text{ and } \rho_{\oplus} - \rho_{\odot} > \theta$$

3.6. Sun sensor model

The Sun sensor model takes the Sun position vector in the inertial reference system calculated by the Sun position propagator and it is rotated in the body reference system by the attitude matrix:

$$S_b = A_{bi} S_i$$

Then the Sun position vector in the body reference system is rotated again in the sun sensor lens –fixed system. Now it is possible to calculate the azimuth Az and co-elevation $Coel$ as a function of the Sun position vector components from the following relations [12]:

$$S_x^{ji} = -\sin Coel^{ji} \cos Az^{ji}$$

$$S_y^{ji} = \cos Coel^{ji}$$

$$S_z^{ji} = \sin Coel^{ji} \sin Az^{ji}$$

where the superscript ji denotes the Sun sensor. There are four Sun sensors which are located as illustrated in Figure 13.

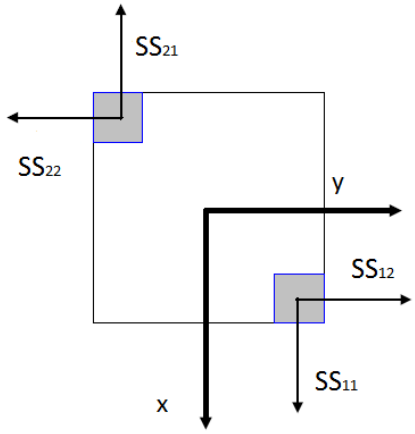

Figure 13. Sun sensors location

The Sun is in the field-of-view of the Sun sensor if $Coel^{ji} \leq 65°$. Then the standard deviation σ_ε of the noise which will be added to the Sun position vector to simulate a real measurement is calculated as [12]:

$$\sigma_{\varepsilon^{ji}} = a + bCoel^{ji}$$

with $a = 0.01°$ and $b = 0.09°/50°$. This comes from the assumption that the noise is a linear function depending only on the co-elevation. Then, the noise is added to the angles Az^{ji} and $Coel^{ji}$:

$$\tilde{A}z^{ji} = Az^{ji} + \varepsilon^{ji}$$

$$\tilde{C}oel^{ji} = Coel^{ji} + \varepsilon^{ji}$$

where ε^{ji} is a zero-mean Gaussian random noise with the variance $\sigma^2_{\varepsilon^{ji}}$. The Sun sensor measurements are then calculated using the equations reported above. The measurement vectors of each Sun sensor are rotated again in the spacecraft reference system and the Sun position measurement vector is given by a weighted mean of the four Sun sensors readings. Obviously, a measurement from each Sun sensor is considered valid if the Sun is in the sensor field-of-view and the spacecraft is not in eclipse.

3.7. Earth horizon sensor model

The Earth horizon sensor model takes as input the position of the satellite along its orbit, computed by integration of the equations of orbital motion with the initial condition defined by the orbital parameters. Then it is rotated in the body reference system by the attitude matrix, and noise is added to create a realistic measure of the nadir vector, $\tilde{E}_b$. Measurement of the nadir vector, involves various types of errors which can be classified generally as random and systematic errors. Random errors come from the noise of the detector, amplifier and processing electronics, change in the alignment of sensor axis and drifts in the amplifiers due to aging or environmental changes. Systematic errors are due to seasonal Earth horizon variations, variations in height of CO_2 band and Earth oblateness. The output noise of the Earth horizon sensor

is modelled adding a zero-mean Gaussian random noise with the variance given in the datasheet. The simulated measurement can be considered valid if the Earth is in the field-of-view (FOV) of the sensor. From geometric considerations, the condition is satisfied if:

$$\alpha < \beta + FOV/2$$

where α is the angle between the normal to the satellite face where the Earth horizon sensor is placed ($-Z$ in ALMASat-EO) and the nadir vector in the body reference frame, FOV is the Earth horizon sensor field-of-view, which is equal to $37°$ for ALMASat-EO Earth horizon sensor, and β is half of the Earth cone angle with respect to the spacecraft orbital position and it is defined as:

$$\beta = \sin^{-1}\left(\frac{R_\oplus}{R_\oplus + h}\right) = 64.5°$$

where $R_\oplus = 6378.140\,km$ is the Earth mean radius and $h = 686\,km$ is the orbit height.

3.8. Solar cell model

The model is based on the cosine law which describes the ratio between the solar cell measured current $I_{meas,i}$ and the maximum current $I_{max,i}$ generated when the incident light hits the solar cell orthogonally:

$$\frac{I_{meas,i}}{I_{max,i}} = \cos\alpha_i$$

The standard algorithm of estimating the Sun LOS vector $\hat{r}_{SunEst}$ is:

$$\frac{E_{inc}}{E_{cal}}\hat{r}_{SunEst} = \begin{bmatrix} \frac{I_{meas,1}}{I_{max,1}} - \frac{I_{meas,2}}{I_{max,2}} \\ \frac{I_{meas,3}}{I_{max,3}} - \frac{I_{meas,4}}{I_{max,4}} \\ \frac{I_{meas,5}}{I_{max,5}} - \frac{I_{meas,6}}{I_{max,6}} \end{bmatrix}$$

where E_{inc} is the incident irradiance, equal to $1353\,W/m^2$ in space, and E_{cal} is the calibrated irradiance. This algorithm is error-prone when the Earth albedo induces current in the solar cells. Earth albedo is the main source of error in solar cell measurements; conversely, digital Sun sensors are mostly insensitive to this phenomenon. The amount of solar irradiance reflected by the Earth towards the satellite, influences the power generated by solar cells. Moreover, due to the geometry of the Earth, the albedo irradiance is multi-directional, unlike the solar irradiance which may be assumed to be anti-parallel to the Sun LOS vector. This assumption holds because the distance to the Sun is large relative to the Sun radius for Earth orbiting satellites. Earth albedo can be modeled using the Earth's reflectivity data measured by the Earth Probe satellite for the Total Ozone Mapping Spectrometer (TOMS) project or it can be directly measured using albedo sensors. Earth albedo induced currents can be compensated assuming that the solar cell which generates the highest current is illuminated by solar irradiance only. The maximum current algorithm is based on this assumption and it is given by [13]:

$$\frac{E_{inc}}{E_{cal}}\hat{r}_{SunEst,1} = \begin{cases} \frac{I_{meas,1}}{I_{max,1}} & \text{if } \frac{I_{meas,1}}{I_{max,1}} > \frac{I_{meas,2}}{I_{max,2}} \\ -\frac{I_{meas,2}}{I_{max,2}} & \text{otherwise} \end{cases}$$

$$\frac{E_{inc}}{E_{cal}}\hat{r}_{SunEst,2} = \begin{cases} \frac{I_{meas,3}}{I_{max,3}} & \text{if } \frac{I_{meas,3}}{I_{max,3}} > \frac{I_{meas,4}}{I_{max,4}} \\ -\frac{I_{meas,4}}{I_{max,4}} & \text{otherwise} \end{cases}$$

$$\frac{E_{inc}}{E_{cal}}\hat{r}_{SunEst,3} = \begin{cases} \frac{I_{meas,5}}{I_{max,5}} & \text{if } \frac{I_{meas,5}}{I_{max,5}} > \frac{I_{meas,6}}{I_{max,6}} \\ -\frac{I_{meas,6}}{I_{max,6}} & \text{otherwise} \end{cases}$$

In order to model these measured currents, the true Sun position in the body reference frame is needed to calculate both the temperature and the current on each face. It is given by a Sun position propagator (see 3.4) and then it is rotated in the body reference frame using the attitude matrix A_{bi} which describes the orientation of the satellite with respect to the inertial reference frame:

$$S_{body} = A_{bi} S_{ine}$$

Then the position of the Sun with respect to each solar cell, mounted on each spacecraft face can be described using the director cosines:

$$\alpha_i = \cos^{-1}\left(S_{body} \cdot \hat{n}_i\right)$$

where $\hat{n}_i$ is the versor normal to each face. Now, the output measured from each solar cell can be calculated applying the current cosine law and knowing the maximum current, which is the short circuit current when $\alpha_i = 0°$. In order to improve the modeling of the solar cells current outputs, a temperature dependence is considered. The temperature correction on the current is given by the following relation:

$$I_T = I + \frac{dI}{dT}\left(\tilde{T} - T_{ref}\right)$$

where I_T is the solar cell current considering the temperature effect, dI/dT is the short circuit current variation with respect to temperature variations, $\tilde{T}$ is the measured temperature on the solar cell and T_{ref} is the reference temperature. Both dI/dT and T_{ref} can be found in the solar cell datasheet (see Appendix A and Table 3). The current temperature is measured by a temperature sensor which can be modeled as:

$$\tilde{T} = T + \nu$$

where T is the true temperature and ν is a zero-mean Gaussian noise which satisfies:

$$E\{\nu\} = 0$$

$$E\{\nu\nu^T\} = \sigma^2 I_3$$

where the standard deviation $3\sigma = \pm 2$ ℃. The true temperature is calculated by a thermal model as described in 3.9.

Noises should also be added to these modeled measured currents to simulate real solar cell's current output:

$$\tilde{I}_T = I_T + \nu$$

where ν is a zero-mean Gaussian noise defined as before with $3\sigma = \pm 0.104\, mA$. Small errors due to the inaccuracy of the cosine model approximation when α_i is close to $\pm 90°$ should also be taken into account. In fact, when α_i approaches to $\pm 90°$, half the Sun has sunk below the solar cell and does not produce electrical current, and half the Sun is shining on the solar panel producing current. However, experiments made on solar cells showed that when $\alpha_i > \pm 85°$ the measured currents are very low. Thus, it is assumed that if $\alpha_i > 85°$ (the opposite value is not taken into account since the arccosine function output is defined in the range $[0, 180°]$) then $\alpha_i = 90°$ so that a zero current is modeled in this case. Lastly, Sun eclipse should also be incorporated in this model because solar cell measurements are not available during this period (see 3.5).

3.9. Temperature model

Once in space, the satellite is subjected to direct sunlight, sunlight reflected off of the Earth (albedo) and infrared (IR) energy emitted from Earth's atmosphere. Thus, the equation of heat balance for the satellite can be expressed as [14]:

$$mc\frac{dT}{dt} = Q_{ins} + Q_{IR,Earth} + Q_{albedo} - Q_{out}$$

where m is the satellite mass, c is the specific heat capacity, dT/dt is the variation of satellite temperature with time, Q_{ins}, $Q_{IR,Earth}$ and Q_{albedo} are the incoming heat flows due to direct sunlight, Earth albedo and Earth IR radiation and Q_{out} is the outgoing heat flow due to radiation. They can be expressed as:

$$Q_{ins} = \alpha \phi_{\odot} A_{sat} \cos\theta$$

where $0 \leq \alpha \leq 1$ is the solar absorptivity coefficient, $\phi_{\odot} = 1353\, W/m^2$ is the solar heat flux, A_{sat} is the satellite surface hit by radiation and θ is the angle between the normal to the surface and the Sun direction with respect to the same surface;

$$Q_{IR,Earth} = \alpha \phi_{\oplus} A_{sat} F_{sat,Earth}$$

where $\phi_{\oplus} = 236\, W/m^2$ is the mean Earth heat flux and:

$$F_{sat,Earth} = \frac{1}{2}\left[1 - \sqrt{1 - \left(\frac{R_{\oplus}}{R_{\oplus} + h}\right)^2}\right]$$

is the view factor of the satellite with respect to the Earth;

$$Q_{albedo} = 0.3 \alpha A_{sat} F_{sat,Earth} a$$

where $0 \leq a \leq 1$ is a multiplicative factor which takes into account the illumination of the Earth surface;

$$Q_{out} = \varepsilon A_{sat} \sigma (T_{sat}^4 - T_0^4)$$

where $0 \leq \varepsilon \leq 1$ is the emissivity factor, $\sigma = 5.67051 \cdot 10^{-8}\, W/m^2 K^4$ is the Stefan Boltzmann's constant, T_{sat} is the satellite temperature and $T_0 = 4\, °K$ is the deep space temperature.

In order to consider also the heat exchange between the spacecraft surfaces, the satellite has been modeled using ten nodes: six of them are located in the middle of each face and the other four nodes are placed in the middle of each solar panel [11]. Then the heat exchange between nodes due to radiation and conduction are calculated as:

$$Q_{irr} = \sum_x \varepsilon_j A_j F_{jx} \sigma \left(T_x^4 - T_j^4\right)$$

$$Q_{cond} = \sum_x \frac{k A_{jx}}{d_{jx}} \left(T_x - T_j\right)$$

where j is the considered node, x are the other nodes, k is the material thermal conductivity, A_{jx} and d_{jx} are respectively the surface and the distance between node j and node x.

Then, this model accepts as inputs, the orbital parameters and the satellite orbital propagation calculated by the simulator (see Simulator) and it integrates the heat balance equation starting from a guess value (typically $T = 300\,°K$).

3.10. Gyroscope model

The gyroscope model takes the angular velocity, ω computed from the integration of the Euler's equation of motion and adds noise to create a realistic measured, $\tilde{\omega}$. Two types of noise are added to the signal, Angle Random Walk (ARW) and bias drift. ARW is the high frequency noise term that have correlation time much shorter than the sample time and it causes random error in angle with distribution, which is proportional to the square root of the elapsed time. It is modelled as a zero-mean Gaussian random noise with a variance given by the manufactures datasheet or determined by Allan variance technique. The Allan variance, an accepted IEEE standard for gyroscope specifications, is a time domain analysis technique that can be used to find the characteristics of the noise processes in an instrument. The Allan variance technique uses a clustering method. It divides the data into clusters of specific length and averages the data in each cluster. It then computes the variance of each successive cluster average to form the Allan variance. Each noise source has a different correlation time. By choosing the correct correlation time or cluster length, the desired noise source variance can be calculated [15]. The bias drift is modeled as the integration of a white noise called Rate Random Walk (RRW) with a variance given by the datasheet or determined by Allan variance technique. The integrator is initialized at the initial bias of the hardware. These terms can be seen in mathematical model of the gyro:

$$\tilde{\omega} = \omega + \beta + \xi_{sf} + \xi_{\mathrm{ma}} + \eta_{\mathrm{v}}$$

$$\dot{\beta} = \eta_u$$

where β is the bias drift, ξ_{sf} is the gyro scale factor error, ξ_{ma} is the gyro misalignment error, η_v is the ARW and η_u is the RRW. As stated above, η_v and η_u are independent zero-mean Gaussian white-noise processes with:

$$E[\eta_{\mathrm{v}}(\mathrm{t})\eta_{\mathrm{v}}^{\mathrm{T}}(\tau)] = \sigma_v^2\delta(t-\tau)I_{3\times3}$$

$$E[\eta_{\mathrm{u}}(\mathrm{t})\eta_{\mathrm{u}}^{\mathrm{T}}(\tau)] = \sigma_u^2\delta(t-\tau)I_{3\times3}$$

where $E[\,]$ denotes expectation and $\delta(t-\tau)$ is the Dirac delta function.

Scale factor is the ratio of the change in output to the input. It is generally evaluated as a slope of the straight line that can be fit by the least square method to the input-output data. Axes misalignment is the error from the imperfection of mounting the sensors. It often results in a non-orthogonality of the axes. As a result, each axis is affected by measurements of the other two axes in the body frame. Since axes misalignments are a manufacturing imperfection can therefore easily be detect and compensated by calibration [5].

The equations above are implemented in Simulink to model the gyroscope. The gyro noise sources are scaled by $T_s^{-0.5}$ as suggested in literature. The sample time, T_s is used to correct the units of ARW $\left(°/\sqrt{s}\right)$ and RRW $\left(°/\sqrt{s^3}\right)$ to $°/s$ and $°/s^2$ respectively. The misalignment inaccuracies are added with a gain block in the model. The gain is $I_{3\times3} + G$, where the diagonal values of G are the percent error in scale factor and the off-diagonal values of G are the percent error of misalignment [15]. The dynamic range of the gyroscope hardware is modeled by a saturation block. The gyroscope Simulink model illustrated in Figure 14. A three-axis gyro ADIS16400 is considered for simulations and its complete datasheet is reported in Appendix A. The main parameters values are reported in Table 4:

Gyroscope	Value	Unit
Dynamic Range	$\pm75, \pm150, \pm300$	$°/s$
Scale Factor	$0.05, 0.025, 0.0125$	$°/s$
Initial Bias Error	±3	$°/s$
Bias Stability	0.007	$°/s$
ARW	2	$°/\sqrt{hr}$
3 dB Bandwidth	330	Hz

Dimensions	23 × 23 × 23	mm
Mass	16	g
Power	0.35	W

Table 4. Three-axis gyroscope ADIS16400 main parameters

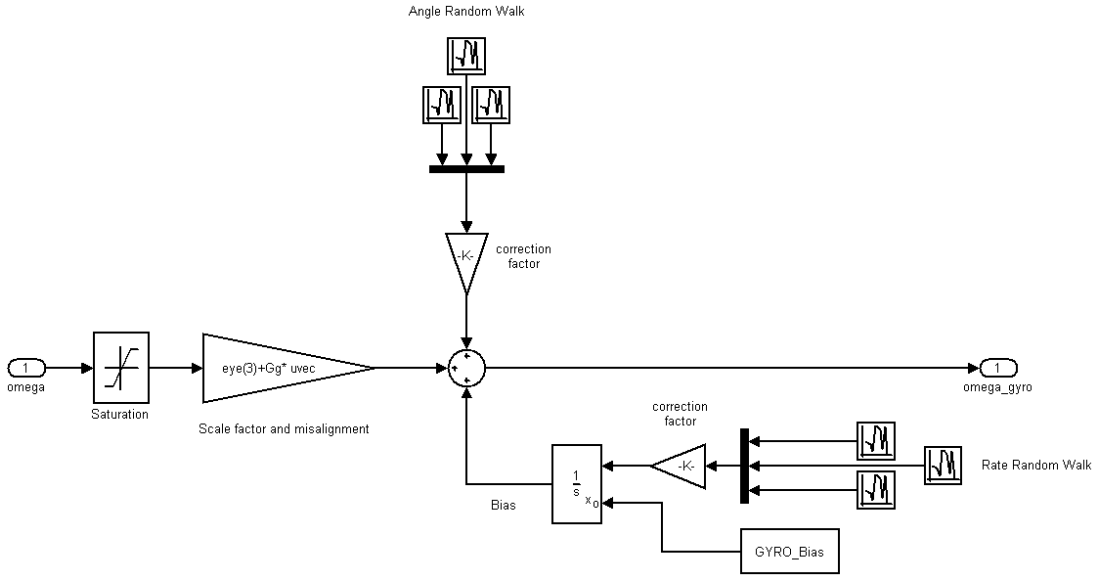

Figure 14. Three-axis gyroscope Simulink model

4. Passive magnetic system for angular rate damping

In [16], a passive magnetic attitude control system for high angular velocity damping was studied by means of simulations performed in the MATLAB/Simulink-based simulator for ALMASat missions. The system consists of hysteresis rods placed along all three axes to dissipate the high rotation kinetic energy caused by a non-nominal separation from the launcher. A preliminary study was carried on in [16] and then the manufacturer was selected and contacted.

The selected soft magnetic material is MUMETALL, also called Permalloy, available at SISRAM S.p.A., the Italian distributor of VACUUMSCHMELZE (VAC). MUMETALL belongs to the category NiFe alloys with high percentage of Ni (72-83 % Ni). The alloys in this group are currently the softest magnetic materials available. They are characterized by high initial and maximum permeability and low coercivity but have relatively low saturation polarization. The low coercivity is strongly required since it makes the material easily magnetized by the Earth magnetic field.

This material is available for small amounts in shape of strips with thickness, $t = 1\ mm$ and width, $w = 150\ mm$. The most important magnetic, mechanical, physical properties and the chemical composition of this Nickel Iron alloy are reported in Table 5 and Table 6:

Magnetic properties	Saturation induction $B_s = 0.8\ T$
	Coercivity force $H_c = 1.5\ A/m$
Mechanical properties	Young modulus $E = 170\ GPa$
Physical properties	Density $\rho = 8.7\ g/cm^3$
	Curie Temperature $T_C = 400$ °C

Table 5. MUMETALL properties

	Ni	**Cu**	**Mo**	**Fe**	**others**
MUMETALL	76.6 %	4.5 %	3.3 %	14.7 %	Mn, Si

Table 6. MUMETALL chemical composition in weight percentage

MUMETALL is characterized by a S-shaped hysteresis loop, which is illustrated in Figure 15 for the typical magnetic field range $[-40, 40]\ A/m$ during ALMASat-EO mission.

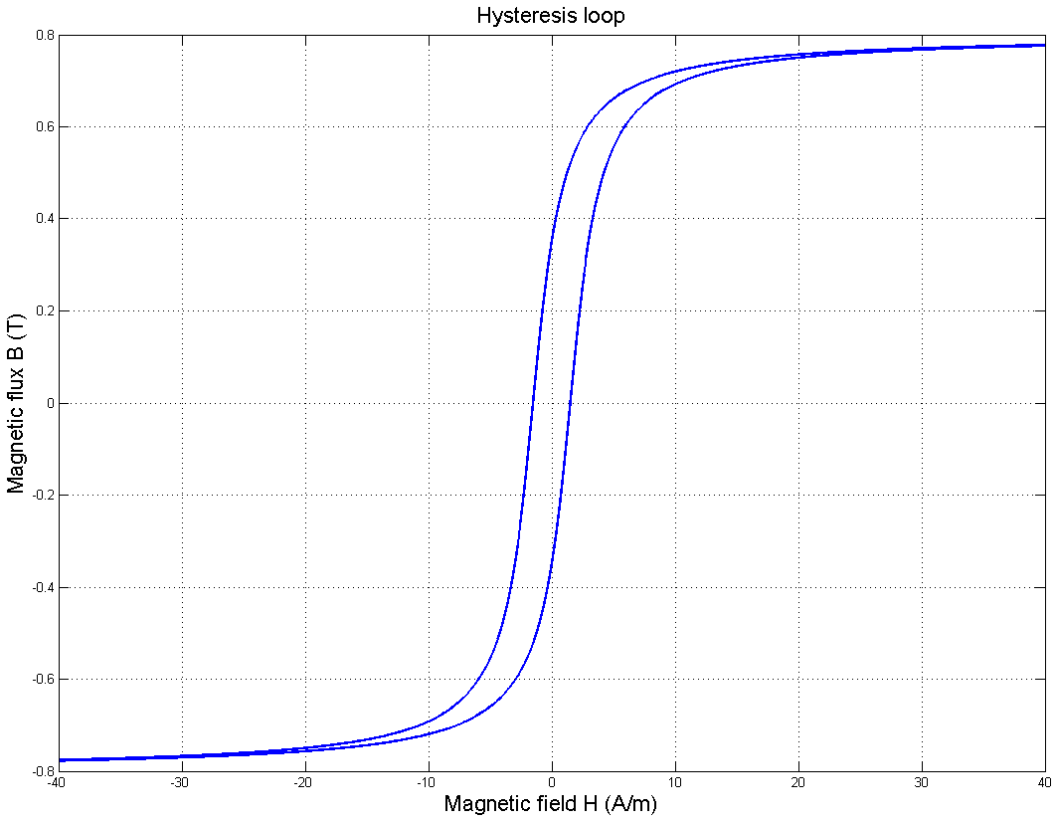

Figure 15. MUMETALL ideal hysteresis loop in the range [-40, 40] A/m

The soft magnetic material need to be subjected to a final heat treatment to set the optimum magnetic properties. This final magnetic heat treatment step takes place after final shaping. The high temperature annealing for MUMETALL takes from 2 to 5 hours at $1000 - 1100\ ℃$ and the cooling in furnace should arrive to $< 300\ ℃$. The heat treatment should be done in H_2 atmosphere. In fact, hydrogen is the preferred protective gas. It prevents scaling and interacts chemically with the metal, for instance removing impurities. Alternatively, nitrogen can be used but the magnetic quality is generally lower when compared to heat treatments under hydrogen although it is cheaper.

Now, the magnetic interaction of the hysteresis rods on the active magnetic attitude control system is studied starting from the conclusions reached in [16]. The magnetic interaction was studied by means of Monte Carlo simulations, starting from a

random distribution of the initial angular velocity norm on the three components and considering the time needed to reach a specific satellite condition. In particular three scenarios were investigated. In the first scenario, the interaction between the magnetic control law *–Bdot*, performed by magnetic coils, and the effect of the hysteresis rods during the detumbing motion is studied. Then, in the second scenario the interaction between the magnetic control law *-Bdot* and the effect of the hysteresis rods during the satellite spin up is investigated. Finally, in the third scenario, the interaction between the magnetic coils and the hysteresis rods during the satellite stabilization up to the three-axis control state is studied. The results, in terms of time, obtained considering an attitude control system with and without hysteresis rods were compared in order to find out a possible magnetic interaction between the hysteresis rods and the active magnetic attitude control system. The results showed that the hysteresis rods effect is negligible in the first and in the second scenario. The results obtained for the third scenario are analyzed in this work.

Further investigations showed that the large time difference between the configuration with and without hysteresis rods in three-axis control is due to an error in the estimation of $cos(\theta)$, where θ is the pitch angle. This variable is generally estimated using the attitude matrix computed by the *TRIAD* algorithm used for attitude determination in ALMASat-1. However, when the measured sun vector and the measured geomagnetic vector are aligned or the satellite is in eclipse, the computed attitude matrix becomes singular and $cos(\theta)$ cannot be estimated in this way. In this case, the attitude determination subsystem estimates $cos(\theta)$ supposing that the angle ψ between the satellite y-axis and the versor normal to the orbital plane is small. Using this hypothesis, it is possible to estimate $cos(\theta)$ by using only the geomagnetic vector measurements since the z-x plane in the body frame and in the reference frame are supposed to be parallel and rotated by θ. If the hypothesis on ψ is not true, then the estimation of $cos(\theta)$ is slightly inaccurate. Since one of the conditions for three-axis control is $\cos\theta \geq 0.99$, where θ is the estimated pitch angle, the inaccuracy in the estimation of $cos(\theta)$, during the verification of the conditions before the three-axis control, leads to a time delay in three-axis control engagement. Thus, the large time difference between the two configurations is due to this attitude estimation problem which may be solved using more attitude sensors measurements (Sun sensor,

magnetometer, Earth horizon sensor, solar cells and gyroscopes) combined in a multi-rate Kalman filter for attitude estimation in all conditions (two vectors alignment and eclipse period). The small time differences between the two configurations are due to hysteresis rods but they are of order of few minutes and hence, negligible.

Figure 16 shows that the estimated $cos(\theta)$ is smaller than 0.99 (see first data tip in Figure 16) then the three-axis control does not act on the satellite at that time. This is due to the error in the hypothesis of small ψ. In fact, although the estimated pitch angle $\theta = \tan^{-1}(sin(\theta)/cos(\theta))$, where $sin(\theta)$ and $cos(\theta)$ are functions of geomagnetic vector measurements, passes through zero, the estimated $cos(\theta)$ is smaller than 0.99. The three-axis control acts on the satellite only if the condition $cos(\theta) > 0.99$ is fulfilled (see second data tip in Figure 16). In conclusion, considering the results reported in [16] and what stated above, the influence of the hysteresis rods on the active magnetic control system is negligible.

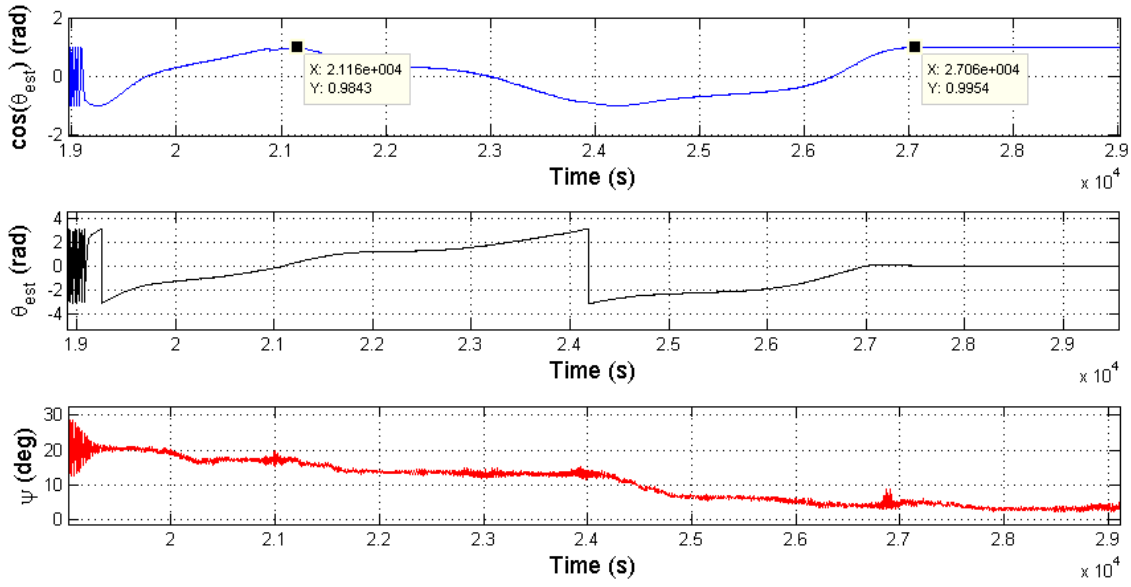

Figure 16. Time history of the cosine of the estimated pitch angle (top), the estimated pitch angle (middle) and the true angle ψ between the satellite y-axis and the versor normal to the orbital plane (bottom) during three-axis stabilization requirements check.

5. Angular rate estimation using solar cells

Solar cells in short circuit mode can be used as simple Sun sensors which work by measuring the current output. They are lower price, mass and power consumption than digital Sun sensors. Thus, they can be used for coarse three-axis attitude determination in safety mode [13]. Moreover, they can be used for angular rate estimation in the event of an unexpected gyroscope failure or when the gyroscopes are saturated by high angular rate of the spacecraft. For instance, in [17], the problem of estimating the angular rate of a satellite in tumbling motion, based on sequential measurements of a single directional vector (Sun direction measurement), is solved by a deterministic algorithm that provides a coarse angular velocity estimate used to initialize an extended Kalman filter (EKF). In [18], an algorithm for angular rate determination using varying solar array currents over an entire orbital period is implemented to graphically determine an average spin frequency. By taking the current data over the given time period and converting it to the frequency domain, a clear spike represents the most frequently occurring rate. In this work, the angular rate estimation of a tumbling spacecraft in safety mode (when low power consumption is required) is performed by an EKF, as described in [19], using sequential readings of solar cells instead of Earth's magnetic field. This filter has been already implemented for ALMASat-1 mission as the only solution to estimate the angular velocity using sequential readings of Earth's magnetic field since no gyroscopes were mounted on board. Furthermore, in case of failure of digital Sun sensors, sequential readings of solar cells can be used for attitude determination together with magnetometer data using a single-point algorithm like *TRIAD*, implemented for ALMASat-1 mission, or filtering algorithms like an EKF or an unscented Kalman filter (UKF) where the uncertainty of the measurement can be incorporated.

5.1. Extended Kalman filter for angular rate estimation

In this section, a summary of the extended Kalman filter implemented to estimate the satellite angular velocity using sequential sensor readings is reported.

The satellite is assumed to be in tumbling motion, such that there are no internal torques acting on the satellite. Because the attitude matrix is assumed unknown, the external disturbance torques are represented in the mathematical model by a zero mean stationary process noise. The Euler's equation describing the rigid body dynamics can be written as:

$$\dot{\omega} = J^{-1}(-\omega \times J\omega) + \xi$$

where ω is the satellite angular velocity, J is the inertia matrix and ξ is a zero-mean Gaussian process noise with power spectral density Q.

The relation between the satellite angular velocity and the measurements variation is given by the filter observation model:

$$\frac{db}{dt} = \frac{\partial b}{\partial t} + \omega \times b$$

where the left hand side (lhs) of the equation is the temporal derivative of the measurement vector and the right hand side (rhs) is the measurement time variation in a body-fixed frame.

For most orbits, the lhs, which is generated only by the change in position of the satellite (minimal during the short sampling interval) and by the slow Earth rotation, is negligible relative to both terms on the rhs of that equation. Therefore, we can set $db/dt \cong 0$ which yields:

$$\frac{\partial b}{\partial t} \approx -\omega \times b = [b \times]\omega$$

where $[b \times]$ is the cross product matrix. The proposed estimator is an extended Kalman filter. The filter's state vector x_k consists of the three satellite angular velocity vector components in the inertial reference frame:

$$x_k = \left[\omega_x \; \omega_y \; \omega_z\right]^T$$

The state propagation is performed by the following non linear state equation, assuming a sampling interval $\Delta t = t_{k+1} - t_k$:

$$x_{k+1} = \Phi_k x_k + u_k$$

where Φ_k is the linearized dynamics state transition matrix and u_k is the stationary zero-mean process white noise. The time propagation of the state estimate can be performed via numerically integrating Euler's equations between consecutive sampling times. However this method requires a high computation effort. This is why the linearized dynamics state transition matrix is used. It can be approximated by :

$$\Phi_k = I + F_k \Delta t$$

where I is the 3×3 identity matrix and the Jacobian matrix F_k is computed as:

$$F_k = \frac{\partial f}{\partial x}\Big|_{x=\hat{x}} = \begin{bmatrix} 0 & \frac{(J_{yy} - J_{zz})\hat{x}_3}{J_{xx}} & \frac{(J_{yy} - J_{zz})\hat{x}_2}{J_{xx}} \\ \frac{(J_{zz} - J_{xx})\hat{x}_3}{J_{yy}} & 0 & \frac{(J_{zz} - J_{xx})\hat{x}_1}{J_{yy}} \\ \frac{(J_{xx} - J_{yy})\hat{x}_2}{J_{zz}} & \frac{(J_{xx} - J_{yy})\hat{x}_1}{J_{zz}} & 0 \end{bmatrix}$$

The sensor reading vector at time t_k is related to the known reference vector via:

$$\tilde{b}_k = b_k + \nu_k$$

where ν_k is the sensor stationary measurement noise:

$$\nu_k \sim N(0, \sigma^2)$$

where σ^2 is the variance of the measurement noise. To derive the filter's measurement equation, the body-referenced temporal derivative is approximated using a first-order backward finite difference, computed using two successive sensor readings. Thus, the observation equation is written as:

$$z_k = H_k x_k + n_k$$

where $H_k = [\tilde{b}_k \times]\Delta t$ is the time-varying observation matrix, $z_k = \tilde{b}_k - \tilde{b}_{k+1}$ is the effective measurement vector, and $n_k = \nu_k - \nu_{k-1}$ is the effective measurement noise.

5.2. Simulations

First, the model of solar cells is validated comparing the Sun position estimated using the solar cells current outputs to the true Sun position in the body reference frame computed by the Sun position propagator. Then the satellite angular velocity is estimated using the extended Kalman filter (EKF), described in [19] and summarized in 5.1, where the magnetometer readings are replaced by the solar cells measurements sampled at a frequency of $2\ Hz$.

The satellite is in detumbling motion with a random initial angular velocity norm ranging from $0°/s$ to $100°/s$ randomly distributed between the three vector components. Eclipse is also taken into account to investigate its effects on the angular velocity estimation filter. During the eclipse, the filter is switched off in order to avoid divergence. In order to consider different eclipse period lengths, a random orbital right ascension of the ascending node (RAAN) is chosen. Moreover, to consider different eclipse period starting time instants, the satellite initial position along its orbit is randomly chosen, considering a random epoch time τ:

$$\tau = \text{launch date} + rand \cdot T_{orb}$$

where $rand$ is a random number between 0 and 1.

Each simulation lasts one orbital period, T_{orb}, plus an initialization time period equal to $2000\ s$ in order to ensure solar cells temperature convergence. The orbital period is given by:

$$T_{orb} = 2\pi\sqrt{\frac{a^3}{\mu}} = 5908.6\ s \cong 98.5 \text{ minutes}$$

where $a = 7064\ km$ is the orbital semi-major axis and $\mu = 398600.44150\ km^3/s^2$ is the Earth gravity constant.

The estimated angular velocity is compared to the true angular velocity computed by integration of the rigid body dynamics equation in order to check the filter performance. To improve the filter convergence, which is very important in real-time estimation, a high initial covariance matrix P_0 is considered. Since the initial angular

velocity estimation is $\hat{\omega}_0 = [0\ 0\ 0]\ rad/s$ and the maximum initial angular velocity norm is equal to $100°/s = 1.7453\ rad/s$, the initial covariance matrix P_0 is:

$$P_0 = 1.7453^2\ rad^2/s^2 \cdot I_{3\times3}$$

The process noise covariance matrix Q_k and the measurement noise covariance matrix R_k values come from filter tuning considerations. In particular, they are chosen equal to:

$$Q_k = 10^{-5}\ rad^2/s^2 \cdot I_{3\times3}$$

$$R_k = 10^{-3} \cdot I_{3\times3}$$

Monte Carlo simulations are run in order to statistically validate the filter performance. The analysis statistic over the 1000 simulations of the estimated angular velocity is performed considering the mean and the standard deviation of the error on each angular velocity component. Moreover, in order to have a statistical parameter which describes the error on the angular velocity norm, the root sum square of the standard deviation of the error on each component is considered:

$$\Sigma_{error} = \sqrt{\sigma_x^2 + \sigma_y^2 + \sigma_z^2}$$

5.3. Results of simulations

In this section the results of Monte Carlo simulations and investigations on results are reported.

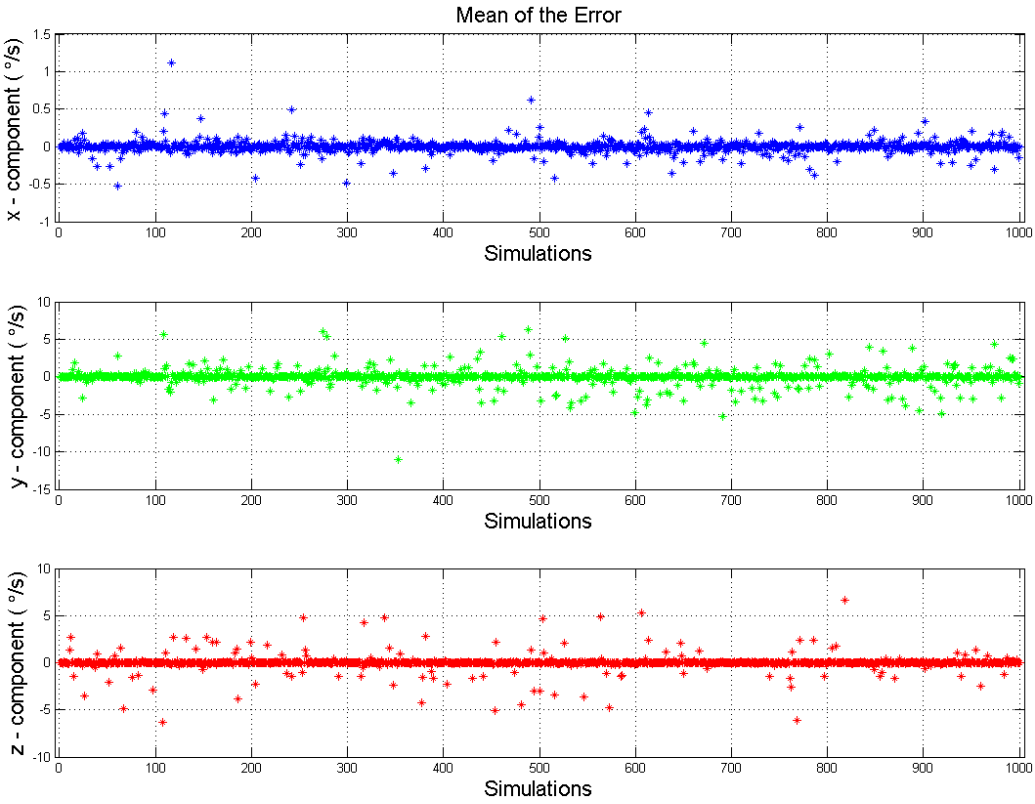

Figure 17. Mean of the error in Monte Carlo simulations

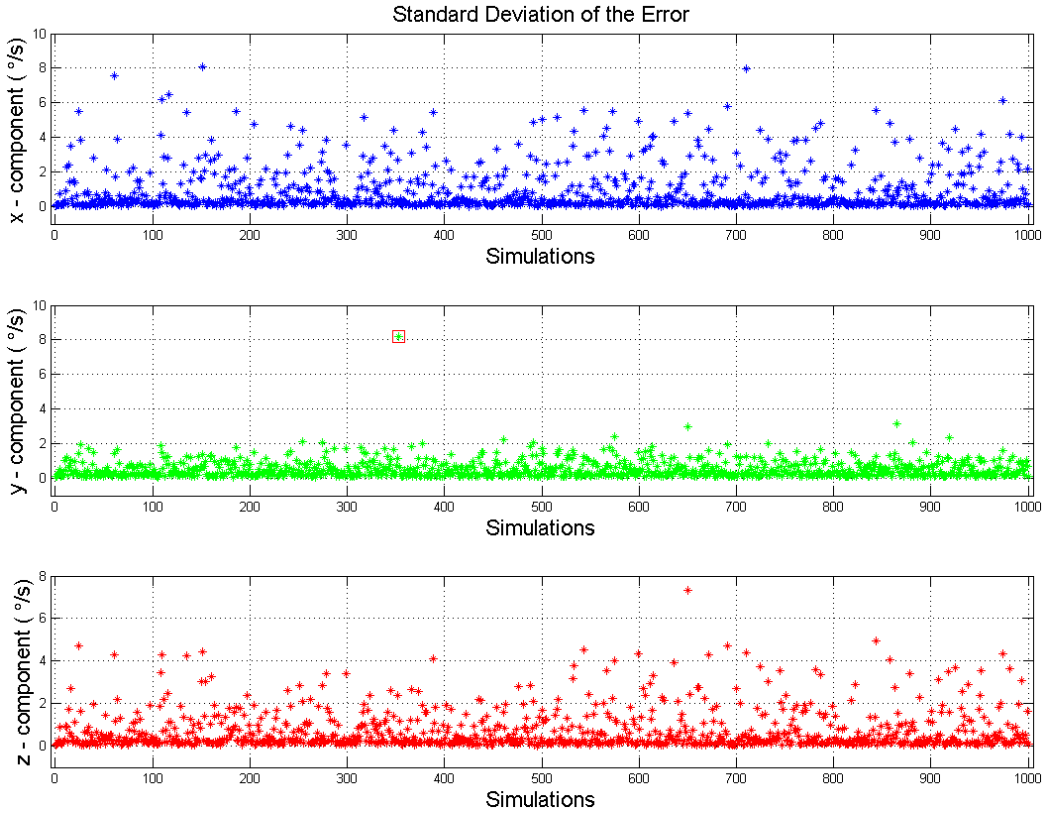

Figure 18. Standard deviation of the error in Monte Carlo simulations

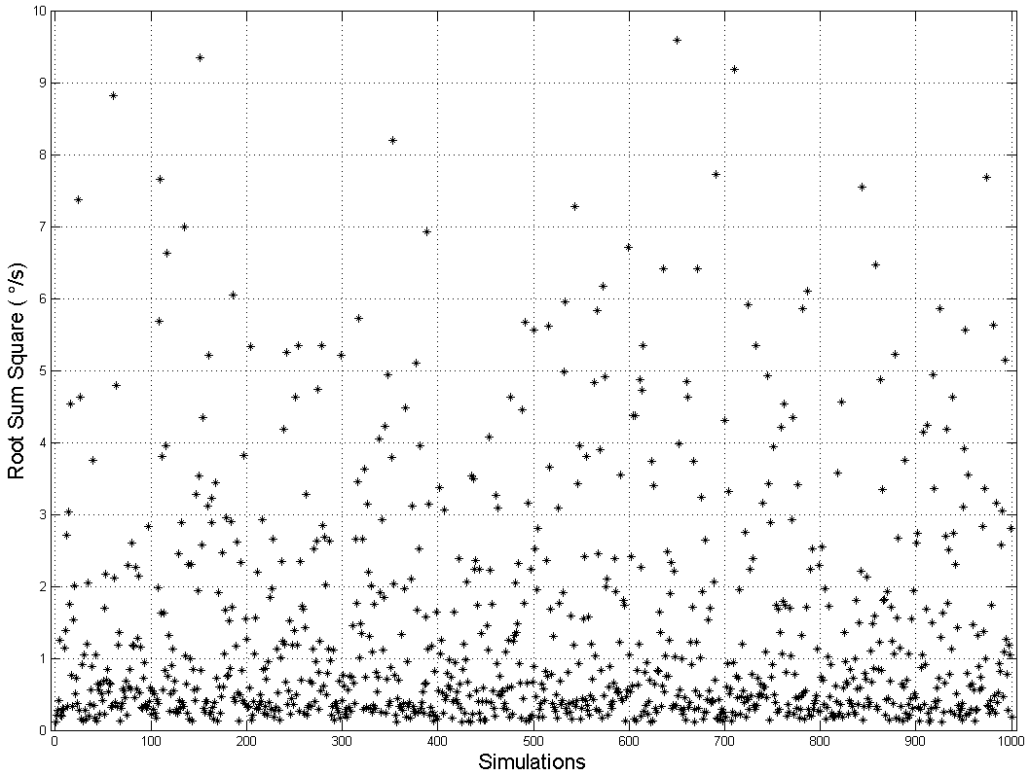

Figure 19. Root sum square of the standard deviation of the error in Monte Carlo simulations

In Figure 17 the mean of the error over 1000 simulations is shown. Most of the points are concentrated around zero, which means that a good performance of the estimation filter is achieved. However in the top panel of Figure 17, where the mean of the error of the angular velocity on x-component is illustrated, some relatively large values can be identified. This is due to slow filter convergence after an eclipse period. Thus, a filter re-initialization is needed to ensure a fast filter convergence which is essential in real-time estimation. The initial state vector estimate is chosen equal to the state vector estimated before the eclipse since it is the best available guess. The result is shown in Figure 20. The filter converges rapidly (in $20\,s$) after the eclipse period (between $t \cong 3100\,s$ and $t \cong 5200\,s$), illustrated in Figure 20 by the shaded region, thanks to the re-initialization of the error covariance matrix P_k.

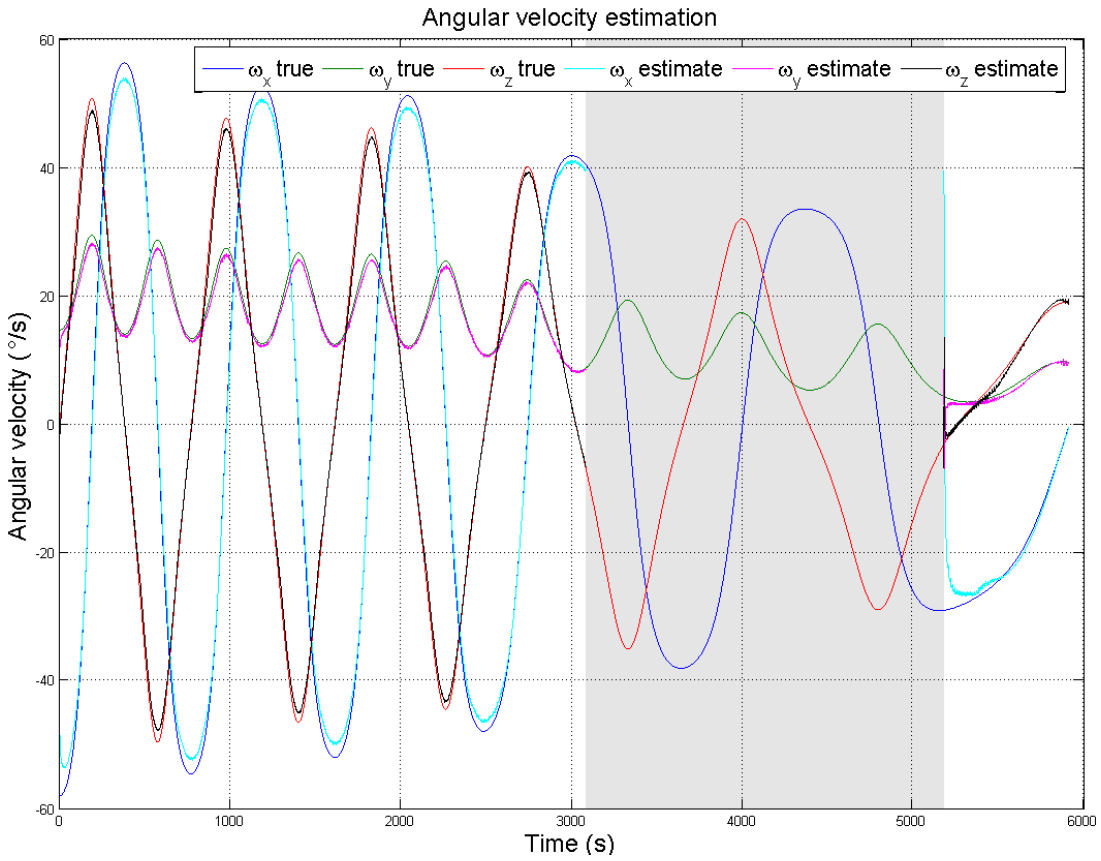

Figure 20. Angular velocity estimation after an eclipse period. The shaded region illustrates the eclipse period.

By looking at the y-axis scale in Figure 17, it is possible to notice that the mean of the error of the angular velocity on the y-component and z-component are larger than those on the x-component. This difference is due to ALMASat-EO inertia matrix (see Table 1) and to the smaller accuracy of filter estimation for high angular velocity. A spacecraft can tumble with a predominant high angular velocity around the maximum and minimum principal axis of inertia for stability considerations (see [4]). Thus, since ALMASat-EO y-axis is the maximum principal axis of inertia and z-axis is the minimum, ALMASat-EO cannot tumble with a predominant high angular velocity around the x-axis. Moreover, since the measurements sampling frequency is $2\ Hz$, the filter estimation is not very accurate for high angular velocities but it is still acceptable for our purposes. A larger sampling frequency, in the order of $5\ Hz$ or $10\ Hz$, leads the filter to diverge, as tested by means of simulations, because the measurement noise is too high. Other Monte Carlo simulations showed that the difference in terms of mean of error along the components does not occur if a spacecraft with all three equal principal axes of inertia is considered, as expected. Figure 21 and Figure 22 show the

angular velocity estimation for two simulations where the mean of the error along the y-component and z-component is larger than the average.

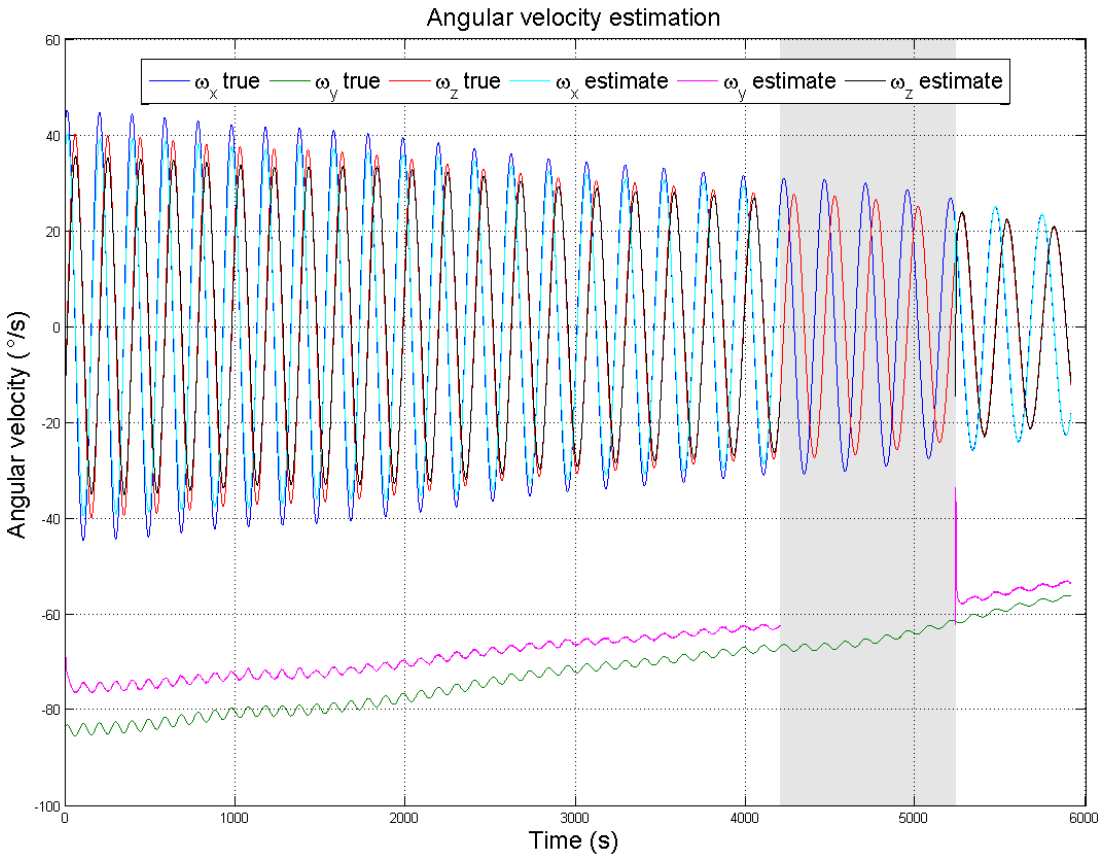

Figure 21. Angular velocity estimation for high angular velocity on y-axis. The shaded region illustrates the eclipse period.

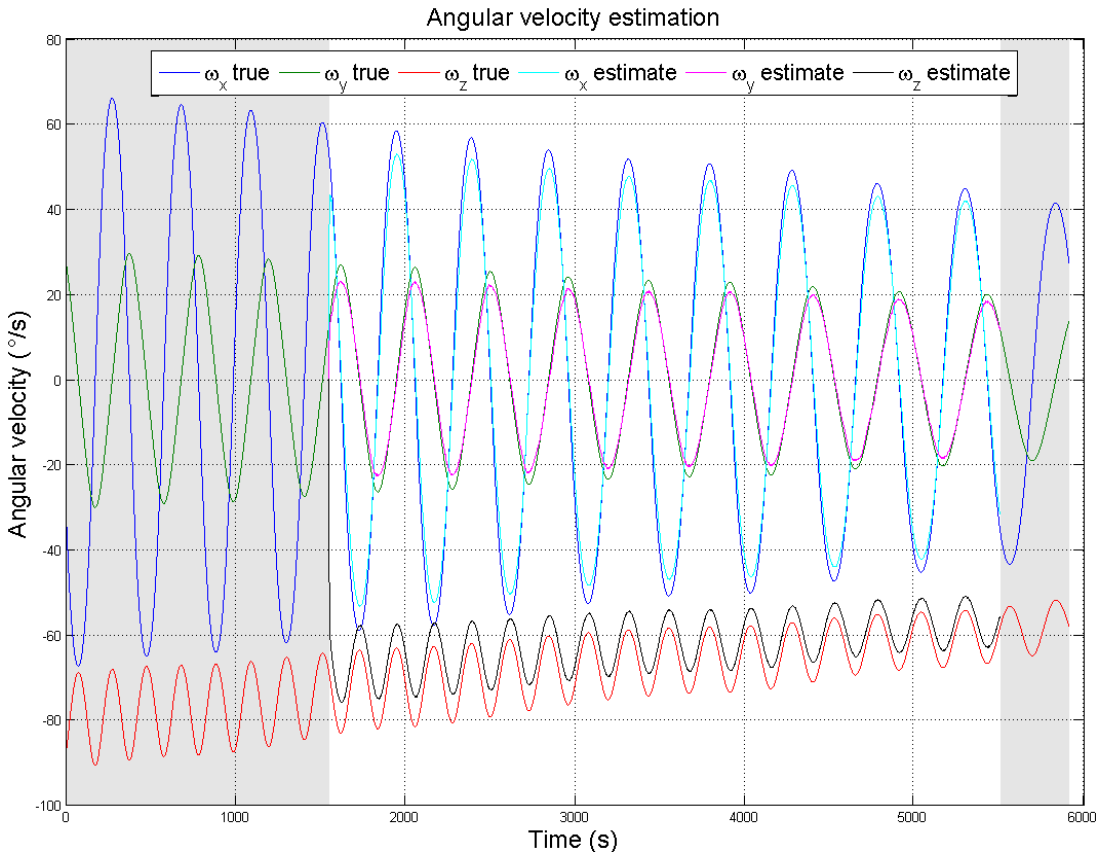

Figure 22. Angular velocity estimation for high angular velocity on z-axis. The shaded region illustrates the eclipse period.

By looking at the particular cases highlighted by the standard deviation of the error in Figure 18, where the obtained values are much higher than the average (see the red rectangle on the y-component panel), one can conclude that this is due to a particular combination between the Sun position in body axes and the angular motion of the satellite. Solar cell measurements cannot estimate accurately the Sun position if the co-elevation angle of the Sun rays on the solar cells is larger than $85°$ since the cosine current law is not valid and the output current cannot be disentangled from the noise, as explained in 3.8. In the considered simulation, two of the Sun line-of-sight (LOS) vector components (x and z-component) are estimated to be zero in the time range $3300\,s \leq t \leq 4700\,s$ due to this problem. This means that the measured LOS unity vector x and z-component are constant and equal to zero and the y-component is equal to one due to the unity norm constraint (see Figure 23). In this case, it is better not to normalize the Sun LOS vector, so that an accurate Sun LOS vector y-component can be estimated (see Figure 24).

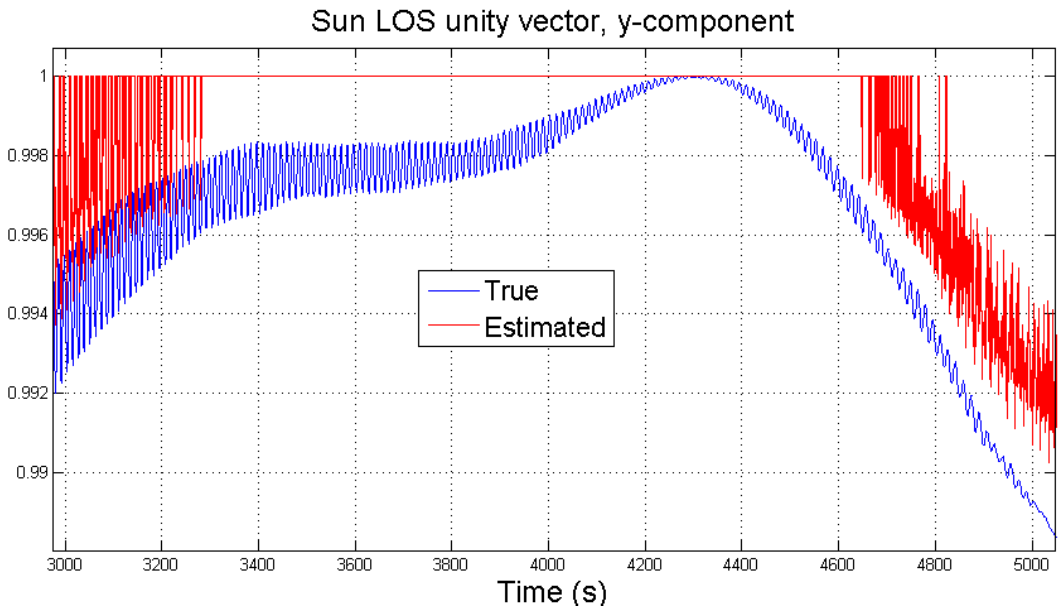

Figure 23. Sun LOS unity vector y-component. The estimation is not accurate due to the unity norm constraint.

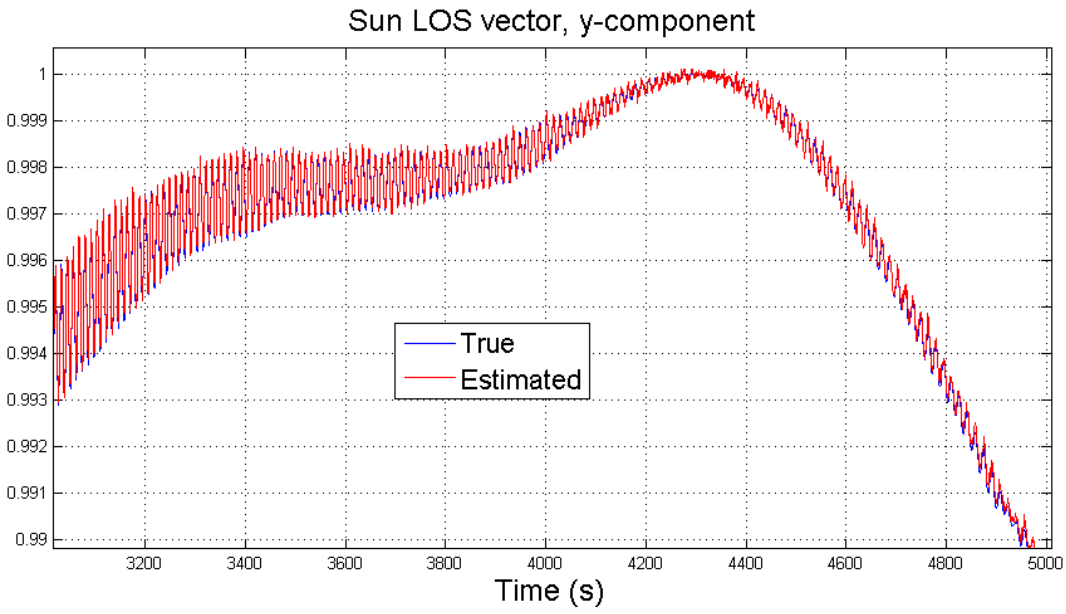

Figure 24. Sun LOS vector y-component. The estimation is accurate since the unity norm constraint is not applied.

However the filter is not able to correctly estimate the angular velocity (see Figure 25). This can be simply explained considering a satellite spinning around the y-body-axis. In this case, the time-varying measurement of the Sun LOS vector component on the x or z-axis is needed in order to estimate this angular velocity. From a mathematical point of view, this can be seen in the filter observation model: in fact, if the measurement is constant in time, we have:

$$\frac{\partial b}{\partial t} = [b \times]\omega = 0$$

which leads after few iterations to a null innovation i_k vector and thus the estimate x_k is constant:

$$i_k = z_k - H_k x_k^-$$

$$x_k = K_k i_k + x_k^-$$

where z_k is the measurement vector, H_k is the observation matrix, x_k^- is the previous estimate and K_k is the Kalman gain.

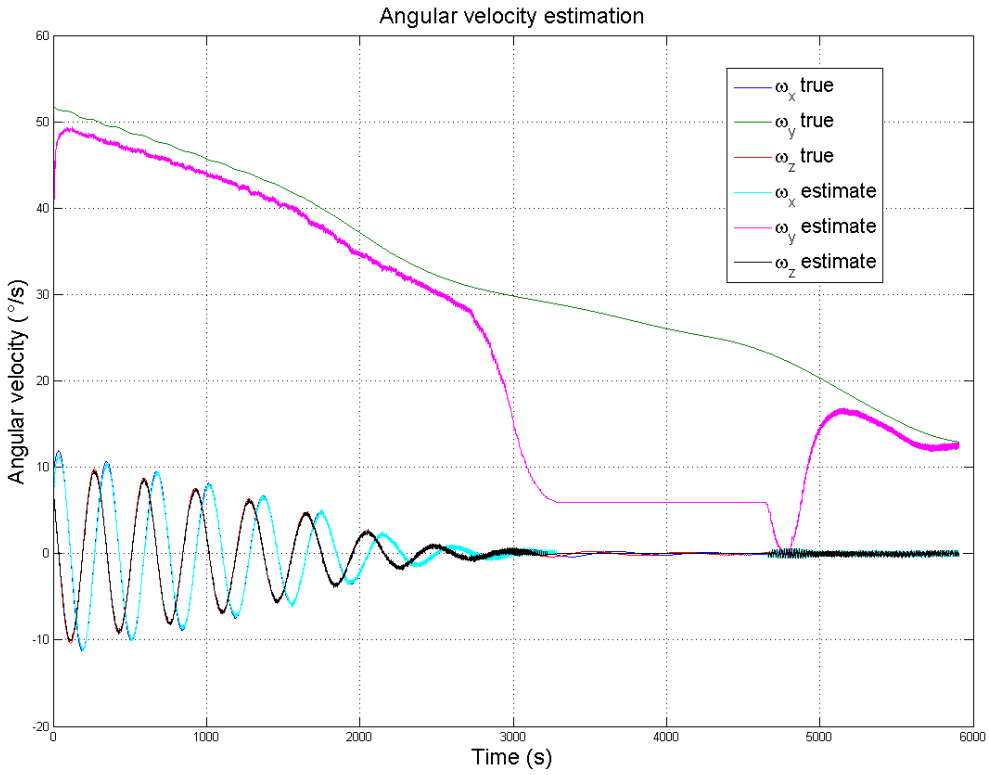

Figure 25. Angular velocity estimation failure in case of constant measurement values

In order to avoid this unacceptably large estimation errors, the filter is switched off when Sun LOS vector components cannot be correctly estimated. Adding this condition, the result is much better, as shown in Figure 26.

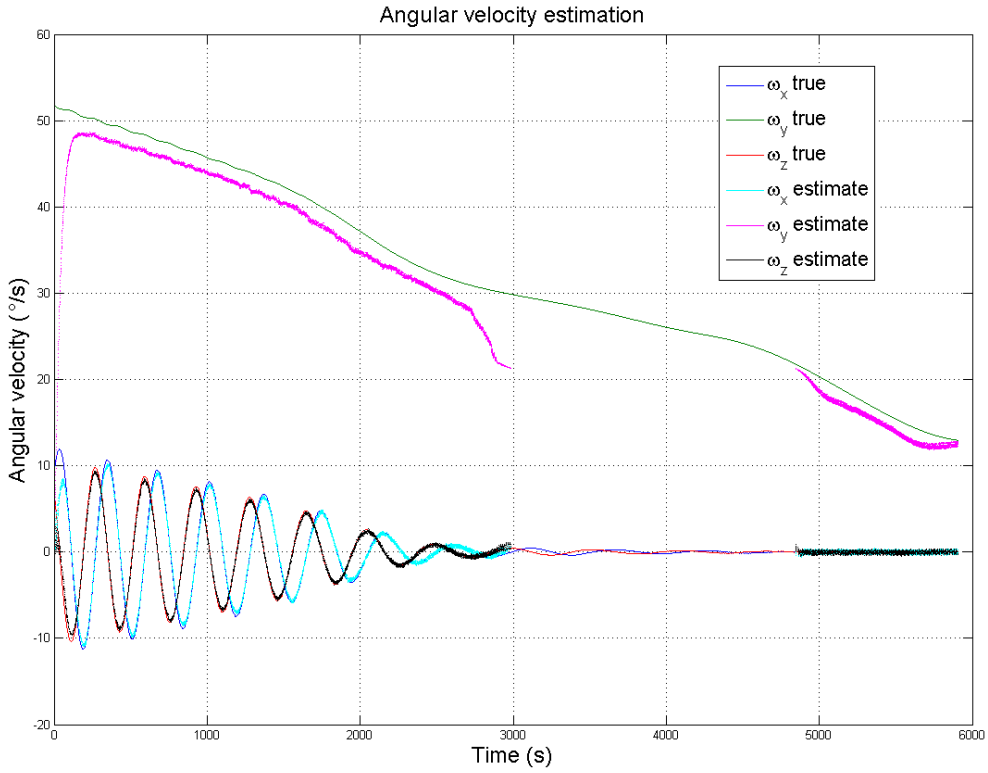

Figure 26. Angular velocity estimation in case of constant measurement values

Finally, in order to reduce the measurement noise on the reconstruction of the Sun position in the body-fixed frame using the solar cells outputs, the unity norm constraint can be considered:

$$\|\hat{S}\| = \sqrt{\hat{S}_x^2 + \hat{S}_y^2 + \hat{S}_z^2} = 1$$

The smallest component of the unity vector $\hat{S}$ is obtained by the smallest current of the currents given by the solar cells and hence, it is more influenced by the noise. Thus, it can be calculated from the equation above to reduce the noise influence. The sign ambiguity is solved knowing which of the six solar cells are illuminated by the Sun. Obviously, this method can be used if three of the six solar cells are hit by the Sun. For instance, let us consider the case when $|\hat{S}_x|$ is smaller than $|\hat{S}_y|$ and $|\hat{S}_z|$, then:

$$\hat{S}_x = \pm\sqrt{1 - \hat{S}_y^2 - \hat{S}_z^2}$$

where the positive sign is considered if the Sun hits the solar cell placed on the $+x$ semi-axis and the negative sign is used if the Sun hits the solar cell placed on the $-x$

semi-axis. The values $\hat{S}_x$, $\hat{S}_y$ and $\hat{S}_z$ are calculated in 3.8 and indicated as $\hat{r}_{SunEst,1}$, $\hat{r}_{SunEst,2}$ and $\hat{r}_{SunEst,3}$ respectively.

Implementing the improvements suggested by these Monte Carlo simulations, the estimation error ranges from $0.05\,°/s$, when the angular velocity norm is small, to $10\,°/s$ when the angular velocity norm is high ($\|\omega\| = 100\,°/s$).

5.4. New solution

In this section, a new arrangement of the solar cells on the satellite faces is studied in order to be able to correctly estimate the Sun position in all conditions. In fact, as widely explained in 5.3 and 3.8, the Sun position cannot be accurately estimated when the Sun LOS unity vector, $\hat{S}$ is almost perpendicular to a unity vector normal to the solar cells, $\hat{n}$ that is when:

$$\hat{S}_{body} \cdot \hat{n}_i < \cos \alpha_t$$

The threshold value of the co-elevation angle, $\alpha_t = 5°$ is approximated and it will be confirmed by new tests on solar cells. The possibility to correctly estimate the Sun position by solar cells output currents have benefits both for the angular rate estimation, as discussed in 5.3, and for attitude determination (see 6). Thus, new arrangements of the solar cells have been studied and a final solution is presented. In order to overcome this problem, two solar cells mounted on two inclined planes are considered on each satellite face (see Figure 27 and Figure 28). In this case, there are 12 solar cells on the satellite for Sun position estimation plus other 12 cells for redundancy. The inclination of the planes is opposed to each other and it is small but larger than α_t to avoid the shadowing of the solar panels and to ensure the validity of the current cosine law at the same time. Considering this new configuration, the Sun hits, at each time instant, a minimum of four solar cells to a maximum of six cells (leaving out the redundant cells) with an elevation angle larger than α_t. The orientation of the solar cells in the body-fixed frame can be mathematically described by the unity vectors normal to the cells:

$$\hat{n}_1 = [\cos i \ 0 \ \sin i]$$
$$\hat{n}_2 = [\cos i \ 0 \ -\sin i]$$
$$\hat{n}_3 = [\sin i \ \cos i \ 0]$$
$$\hat{n}_4 = [-\sin i \ \cos i \ 0]$$
$$\hat{n}_5 = [0 \ \sin i \ \cos i]$$
$$\hat{n}_6 = [0 \ -\sin i \ \cos i]$$
$$\hat{n}_7 = [-\cos i \ 0 \ \sin i]$$
$$\hat{n}_8 = [-\cos i \ 0 \ -\sin i]$$
$$\hat{n}_9 = [\sin i \ -\cos i \ 0]$$
$$\hat{n}_{10} = [-\sin i \ -\cos i \ 0]$$
$$\hat{n}_{11} = [0 \ \sin i \ -\cos i]$$
$$\hat{n}_{12} = [0 \ -\sin i \ -\cos i]$$

where i is the inclination of the cells with respect to each satellite face. In order to arrange these solar cells on ALMASat-EO, the surface area is reduced and consequently the short circuit current given by each cell is smaller. This leads to a lower signal-to-noise ratio (SNR) but the short circuit current at high co-elevation angles is still acceptable (see Table 7). As shown in Figure 27, each solar cell used as coarse sun sensor is cut leaving two electrical contacts to ensure redundancy.

Solar cell	Value	Unit
Short Circuit Current I_{sc} at $\alpha = 0°$	121.4	mA
Short Circuit Current I_{sc} at $\alpha = 85°$	10.6	mA
Inclination	11	°
Surface Area	7.24	cm^2

Table 7. Solar cells main parameters in new configuration

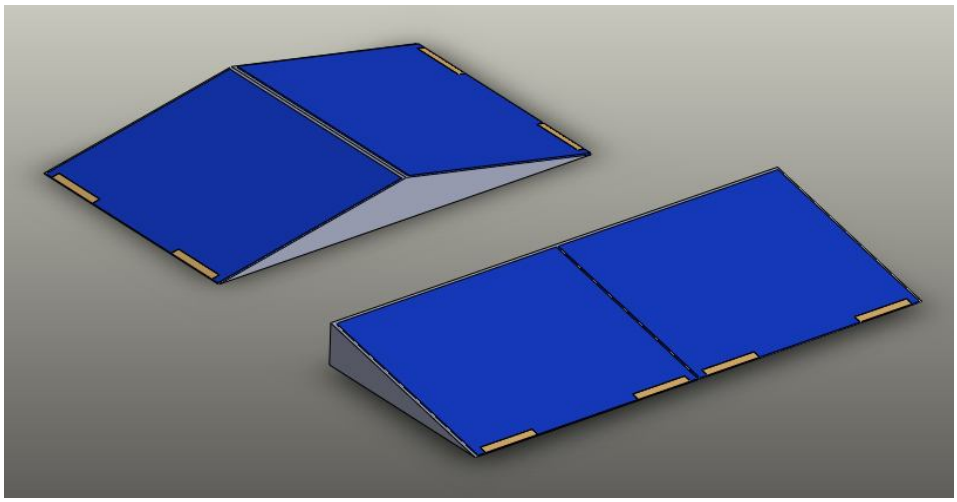

Figure 27. Solar cells used as coarse Sun sensor

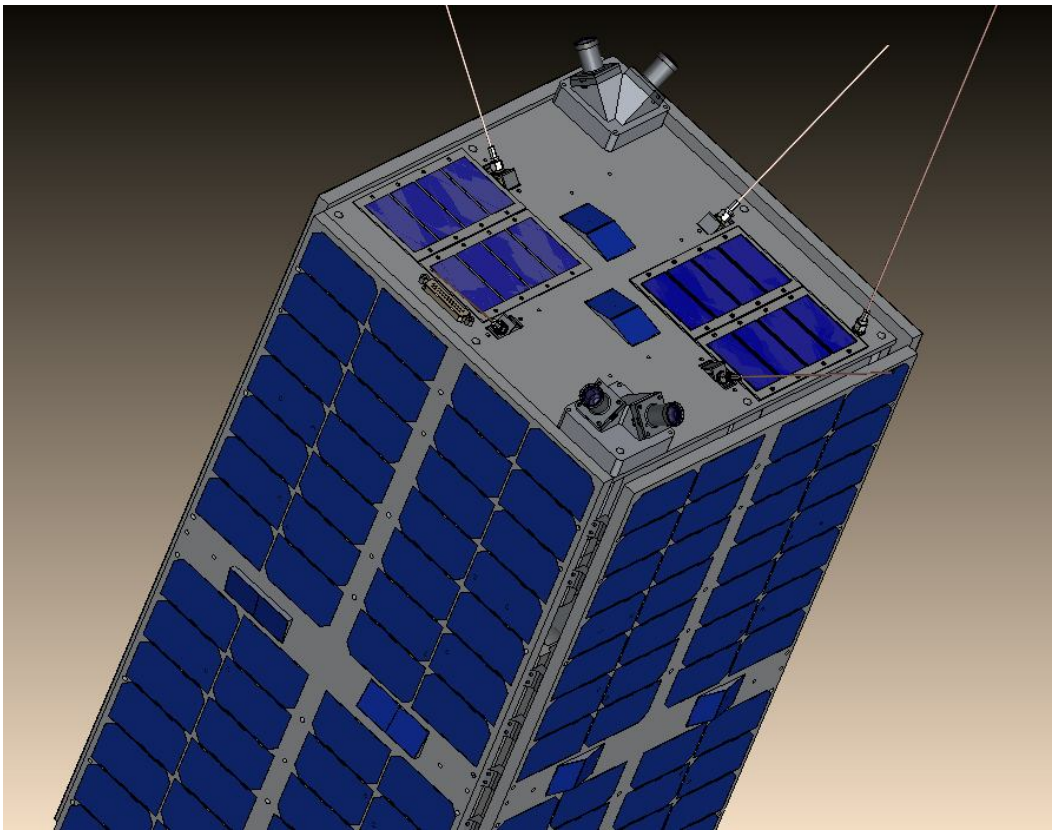

Figure 28. Solar cells arrangement on ALMASat-EO

To estimate the Sun LOS unity vector, $\hat{S}_{body}$ in the body-fixed frame, a new algorithm is implemented for this new configuration. The algorithm is based on the cones intersections. In fact, if the Sun hits a solar cell with a co-elevation angle, α_i then the Sun lies along a circle which is the intersection of the cone (defined around the unity vector normal to the cell, $\hat{n}_i$ and with the angle equal to the arc-length separation, α_i

between the Sun and $\hat{n}_i$) with the unity celestial sphere. That is to say the circle is the locus of possible Sun position corresponding to the angle measurement α_i. Considering another circle generated by the intersection between the unity celestial sphere and the cone defined around the unity vector, $\hat{n}_j$ normal to another solar cell illuminated by the Sun, two intersections between the circles on the unity sphere are defined. They are the two possible Sun positions, $\hat{S}_1$ and $\hat{S}_2$ on the unity sphere as shown in Figure 29.

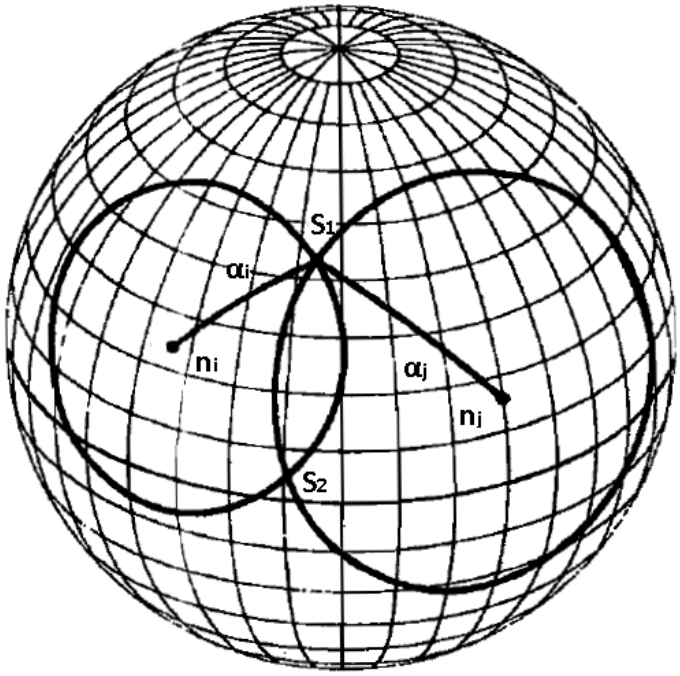

Figure 29. The two possible Sun positions on the unity celestial sphere.

As stated above, at least four solar cells are illuminated by the Sun. Thus, we can define a third circle, generated by the intersection between the unity celestial sphere and the cone defined around the unity vector, $\hat{n}_k$ normal to a third solar cell illuminated by the Sun, to solve the ambiguity between the two possible Sun LOS unity vectors. This geometrical problem is specified by three simultaneous equations in three unknowns (S_x, S_y, S_z):

$$\hat{S}_{body} \cdot \hat{n}_i = \cos \alpha_i$$

$$\hat{S}_{body} \cdot \hat{n}_j = \cos \alpha_j$$

$$\hat{S}_{body}^T \cdot \hat{S}_{body} = 1$$

The first two equations define the cones angles and the last one describes the unity norm constraint of the Sun LOS vector. These three equations may be solved using the following technique due to Grubin [1977]. Let:

$$x \equiv \frac{\cos\alpha_i - \hat{n}_i \cdot \hat{n}_j \cos\alpha_j}{1 - \left(\hat{n}_i \cdot \hat{n}_j\right)^2}$$

$$y \equiv \frac{\cos\alpha_j - \hat{n}_i \cdot \hat{n}_j \cos\alpha_i}{1 - \left(\hat{n}_i \cdot \hat{n}_j\right)^2}$$

$$z \equiv \pm\sqrt{\frac{1 - x\cos\alpha_i - y\cos\alpha_j}{1 - \left(\hat{n}_i \cdot \hat{n}_j\right)^2}}$$

$$C = \hat{n}_i \times \hat{n}_j$$

Then, the solutions for $\hat{S}_{body}$ are given by:

$$\hat{S}_{body} = x\hat{n}_i + y\hat{n}_j + zC$$

This equation gives the two possible ambiguous Sun LOS unity vector solutions. The ambiguity is solved repeating this routine considering a third cone. If the radicand in the equation for z is negative, then no real solutions exists; i.e., the cones do not intersect. However, in our problem there are always three intersecting cones which defines a unique solution.

In the real case problem, noise on the output currents should be taken into account. This is simulated as described in 3.8. In order to reduce the noise influence on the Sun position estimation, the algorithm takes into account that the highest solar cell output current corresponds to the most reliable co-elevation angle measurement since the SNR is the highest.

5.5. Results of simulations for the new solution

To test the effectiveness of this new proposed arrangement of the solar cells and the corresponding algorithm to estimate the Sun LOS unity vector, the scenario, described in 5.3, when the angular rate estimation was problematic (see Figure 25) is

considered. The angular velocity estimation in this scenario is shown in Figure 30. The filter performance are good over the entire orbital period differently from the case described in 5.3. The error slightly increases to a maximum of $1.5\,°/s$ in a small time interval when the Sun position variation in body axes is very close to zero. Comparing Figure 25 to Figure 30, the benefits of this new proposed solution for solar cells arrangement in angular velocity estimation is clearly proved.

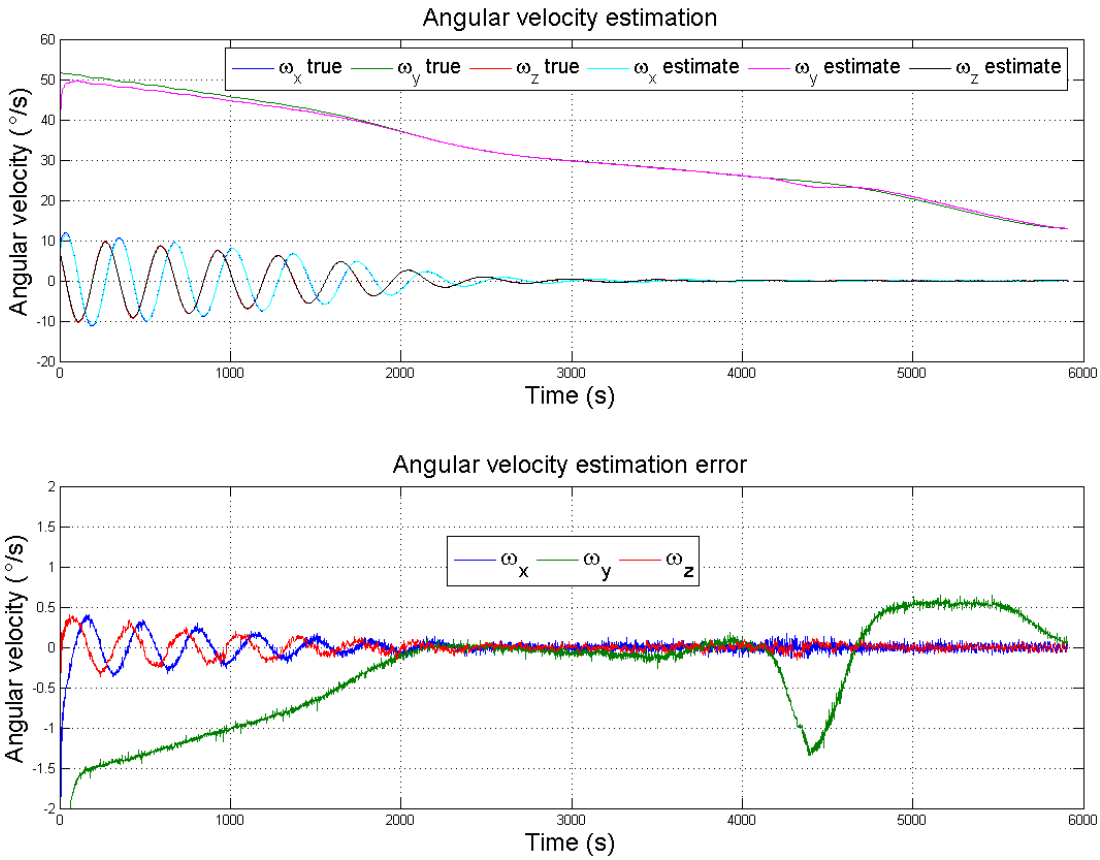

Figure 30. Angular velocity estimation using the new proposed solution

In order to statistically validate the angular rate estimation using the new solution described in 5.4, which consists of a new arrangement of the solar cells on the satellite and a new algorithm to estimate the Sun LOS vector, Monte Carlo simulations are performed. These simulations are run using the same parameters described in 5.2. The filter re-initialization after the eclipse period is also considered as suggested from the results previously obtained.

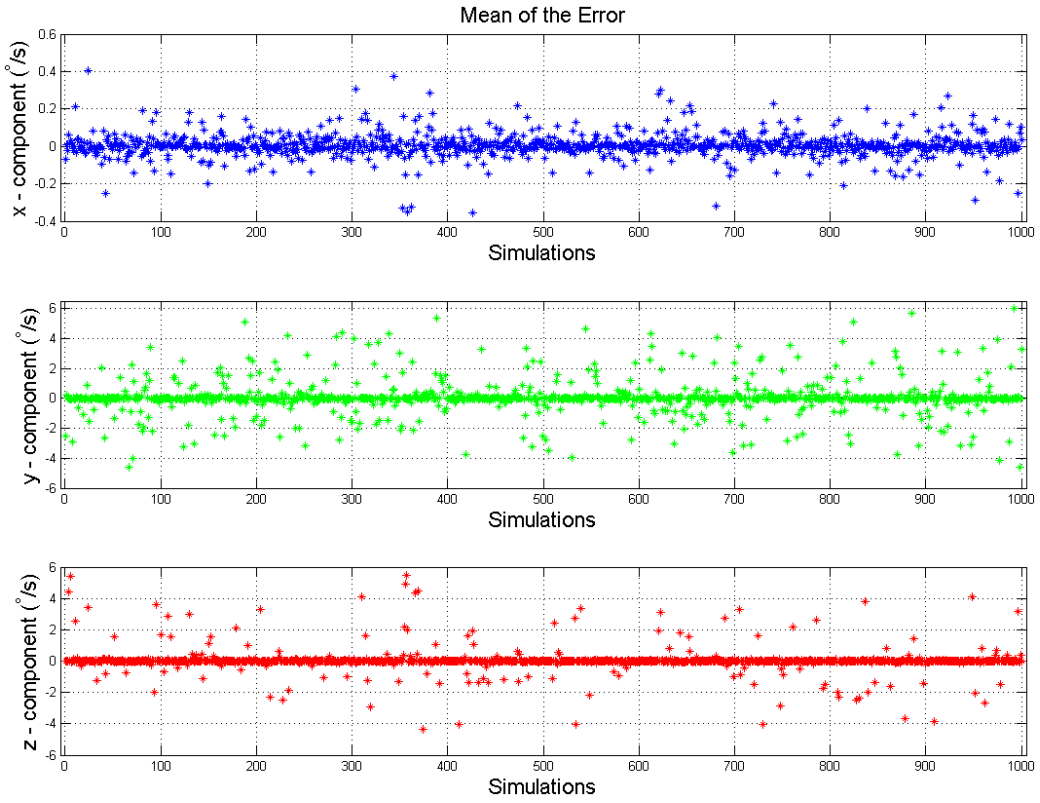

Figure 31. Mean of the error in Monte Carlo simulations for the new solution

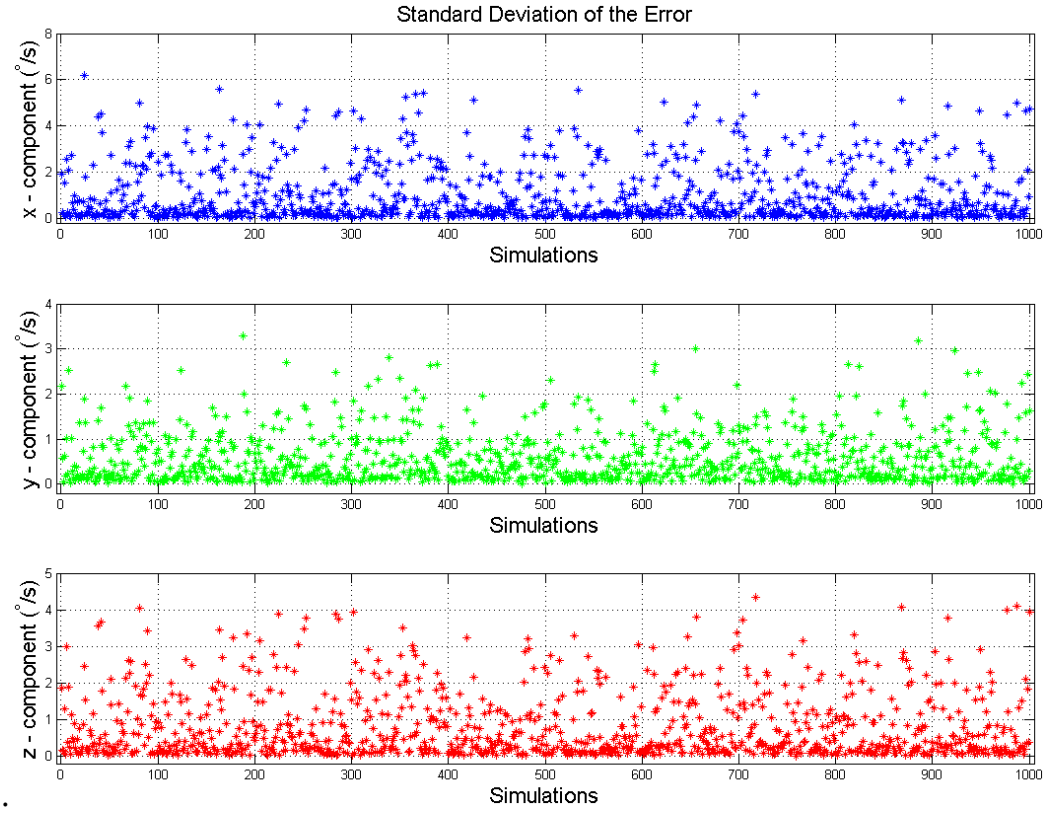

Figure 32. Standard deviation of the error in Monte Carlo simulations for the new solution

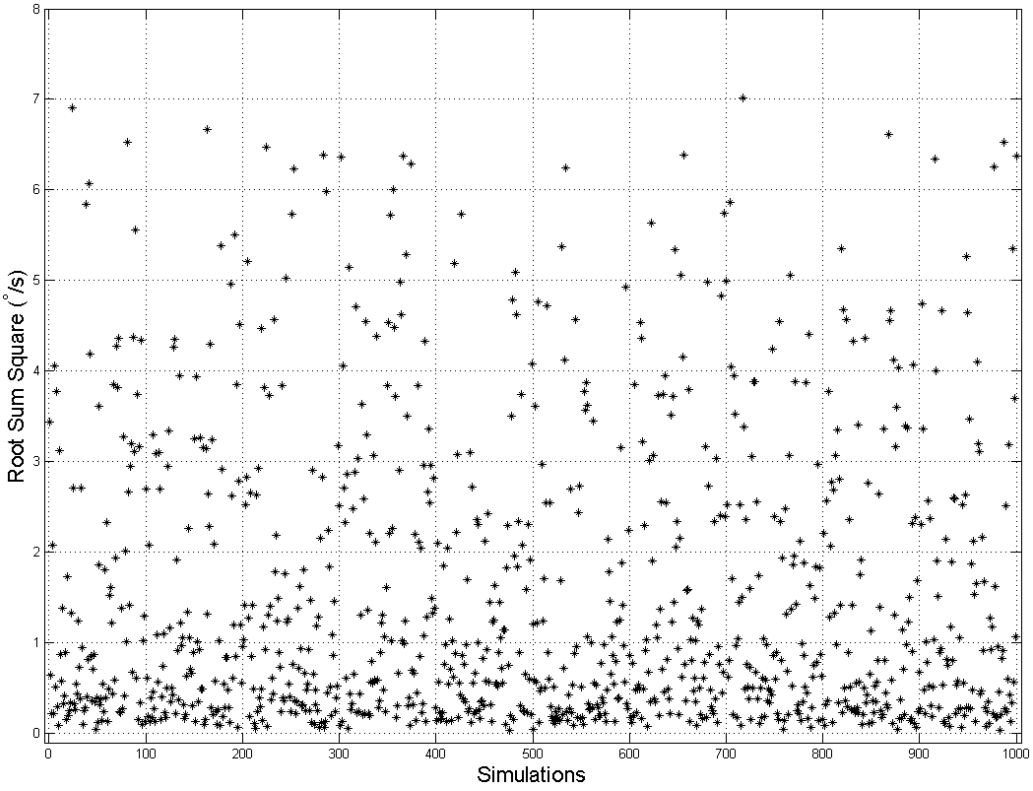

Figure 33. Root sum square of the standard deviation of the error in Monte Carlo simulations for the new solution

Figure 31, Figure 32 and Figure 33 show respectively the mean of the estimation error, the standard deviation of the estimation error and the root sum square of the standard deviation of the estimation error, Σ_{error} (see 5.2) for the Monte Carlo simulations.

Comparing Figure 31 with Figure 17 and Figure 32 with Figure 18 and Figure 33 with Figure 19, one can state that the angular rate estimation is more accurate using the new proposed solution.

By looking at the y-axis scale in Figure 31, it is possible to notice that the mean of the error of the angular velocity on the y-component and z-component are larger than those on the x-component. As described in 5.3 this is due to ALMASat-EO inertia matrix. The larger values in Figure 31 are still due to the smaller accuracy of filter estimation for high angular velocity while the larger values in Figure 32 are still due to the convergence time at the beginning and after the eclipse period. These values are smaller than those ones shown in Figure 18 thanks to the filter re-initialization.

6. Attitude determination

The problem of attitude determination (AD) from vector observations is to specify the orientation of the axes of a Cartesian coordinates system *B*, fixed to a rigid body (e.g. the satellite), in a given Cartesian coordinates system of reference *R*. The on-board attitude estimation represents a major task of the attitude and orbit determination and control subsystem (AODCS) as it is necessary to guarantee the spacecraft pointing accuracy as prescribed by the mission requirements. Several algorithms for spacecraft attitude estimation can be found in the literature and they are mainly divided into two categories:

- Single-point algorithms
- Filtering algorithms

Single-point algorithms sample the attitude hardware once and provides an estimate of the attitude at the time of sampling. Filters continuously sample the sensors and incorporate dynamic models of the attitude, in order to give an attitude estimate based on a weighted average of the predicted measurement and sensor data.

The single-point algorithms are based on the least square's problem published in 1965 by Wahba. The problem formulation is known as Wahba's problem, and the optimal solution is the attitude which minimizes Wahba's cost function:

$$J(A) = \frac{1}{2}\sum_{i=1}^{n} a_i \|b_i - Ar_i\|^2$$

where A is the attitude matrix, b_i is the measurement vector in the body-fixed frame, r_i is the reference vector in the reference frame and a_i are proper weights. The principle of attitude determination by Wahba's problem formulation is based on vector observations: it requires that two or more vectors can be measured in a spacecraft-fixed frame, and the same vectors must be known in a reference frame as well. By comparing the vector observations in reference and body-fixed frames, the attitude of the satellite may be estimated. Since Wahba formalized the problem in 1965, numerous solutions to Wahba's problem have been published. The TRIAD algorithm is a simple solution to Wahba's problem based on two vector observations. The

simplicity of the TRIAD algorithm still makes it attractive for on-board implementations as for ALMASat-1 mission. Davenport's Q-Method algorithm uses the quaternion attitude representation to parameterize Wahba's problem, which is formulated as an eigenvector problem. The Quaternion Estimator (QUEST) algorithm is an extension to Davenport's Q-Method algorithm, developed by Shuster in 1981, which avoids solving the eigenvalue problem, and instead formulates Wahba's problem as a characteristic equation. In 1988, Markley published an algorithm which solves Wahba's problem, in its original formulation using the attitude matrix (or direct cosine), by applying the Singular Value Decomposition (SVD) Method. This algorithm evolved into the Fast Optimal Attitude Matrix (FOAM) algorithm, published in 1993 by Markley, and is comparable to the QUEST algorithm in computational speed. In 1998, Mortari published the EULER-Q algorithm which solves Wahba's problem in terms of Euler angle and axis. In [20] an accurate description of several single-point algorithms can be found and in [21] several simulation results are illustrated.

Several extensions of the single-point algorithms exist, which make use of multiple sensor samples in order to improve the attitude estimates. The Filter QUEST, [Shuster, 1989], the Recursive Quaternion Estimator (REQUEST), [Bar-Itzhack, 1996] and its optimized version (OPTIMAL REQUEST), include past measurements that require accurate knowledge of the angular velocity in order to propagate the attitude between sample times. A filtering algorithm, which include multiple samples and dynamical descriptions of the system, was presented by Rudolph E. Kalman in 1960. From a statistical description of the system dynamics and measurements, the Kalman filter produces an optimal estimate of the state of the system. However, some extension to the Kalman filter is necessary in order to apply the filter in attitude determination. The problem is that the general used attitude parameters, the attitude matrix and the quaternion, are constrained parameters, which must be taken into account when calculating estimates. In 1985, Bar-Itzhack and Oshman derived an Extended Kalman Filter (EKF), which assumes an additive correction. The EKF linearizes a non-linear system around the current estimate of the system state and applies the linear Kalman filter equations on the linearized system. In 1997, Julier and Uhlmann published a new algorithm, known as the UKF. This algorithm is gaining recognition throughout the attitude determination research community, even though the EKF has been the

preferred ADCS algorithm for more than two decades. The EKF may experience problems with non-convergence, due to first order approximations of the system linearization. The improvement of the EKF has been branched in two direction, the Iterated Extended Kalman Filter (IEKF), and the UKF. The IEKF uses multiple iterations of the EKF in order to ensure convergence. The UKF works on the premise that approximating a Gaussian distribution is easier than approximating a non-linear function. The unscented transformation (UT) uses a set of samples, or sigma points that are determined from the previous estimate error covariance, process noise covariance and the previous state estimate of the state. Sigma points are then propagated through the nonlinear system in order to obtain the a priori error covariance and the a priori state estimate. The UKF has been adapted to attitude determination by Crassidis and Markley in 2003. The advantage of the UKF over the EKF is the fact that calculation of the first order Jacobians of the non-linear system models are avoided. In [21] an accurate description of some filtering algorithms is given and performance analysis of filtering algorithms can be found in [21] and [1].

6.1. Federated Unscented Kalman Filter

The filtering algorithms used for spacecraft attitude estimation are mainly centralized algorithms which do not satisfy requirement of multi-rate information synthesis, fault tolerance and system modularity. Thus, in this work, a distributed multi-sensor fusion architecture is considered in order to satisfy the aforementioned requirements. In particular, a federated version of the unscented Kalman filter (FUKF) is implemented in ALMASat-EO attitude determination subsystem and tested through simulations. The FUKF algorithm is preferred to the federated extended Kalman filter (FEKF) for its better precision and faster convergence speed [22].

Federated filtering consists of two parts: local filters (LF) and the master filter (MF). The LFs are UKFs parallel processed and independent of each other, and their estimated results are fused in the MF. In each LF, a local estimate is obtained using the measurement of local sensors. The MF uses the estimates of the LFs to update the global state estimate in a fusion process, and this result is used for the initialization of

LFs [23]. A scheme of the FUKF implemented for ALMASat-EO ADCS is illustrated in Figure 34:

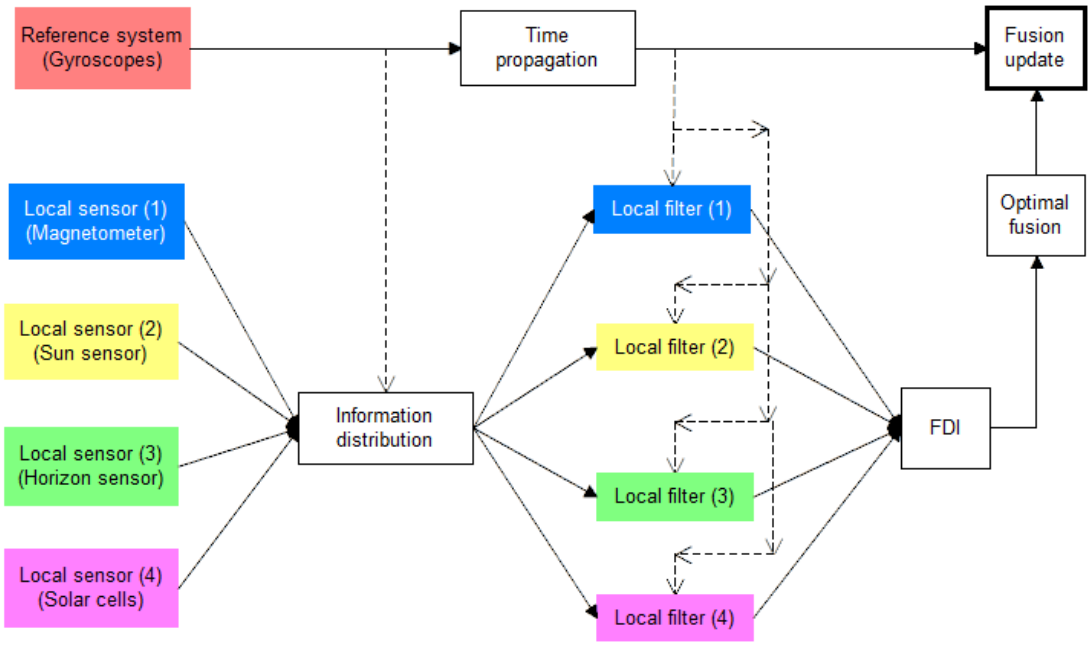

Figure 34. ALMASat-EO Federated Unscented Kalman Filter scheme

In this work, a multi-rate sampling and not periodical fusion system is considered since the sampling periods of sensors can be quite random and asynchronous. Sometimes, certain sensors may get out of their field of view during certain time spans. For example, when the spacecraft went into the shadow of the Earth, the sun sensor and the solar cells could not take part in the fusion process. This is also the case when the Earth is not in the FOV of the Earth horizon sensor. In addition, when fault occurred, the pertaining LF should be isolated [22]. For this purpose, a fault detection and isolation (FDI) algorithm is implemented before the MF. Fault detection usually requires continuous careful monitoring of the measured output data. In a normal case, the output data follow known patterns of evolution with limited random disturbance and measurement noise. However, the measured output data change their nominal evolution pattern when sensor failures occur. General fault detection algorithms are based on considering these differences between the evolution patterns and the measured output data [23].

In this approach, the global sampling period is supposed to be the same as the reference system, i.e. the gyroscopes, which is also the most rapid sensor in the system. Due to the on-board computer limited power, algorithm computational burden

should be considered. Hence, sigma points are only produced and propagated for those LFs whose dedicated sensor had new measurement. If there had no sensor sampled in the system, then the FUKF only propagates forward in time the state and its covariance without measurement correction, and sigma points are not calculated reducing the computation burden. This technique is called information-sharing process. At the beginning of each global sampling step, every LF is checked to acknowledge whether there is new measurement in its dedicated sensor and share fractions β^m, $m = 1, 2, \dots l$, where l is the number of LFs, are calculated:

$$\beta_{temp}^m = \begin{cases} 0 & \text{if local sensor } m \text{ did not sample} \\ \beta_0^m & \text{if local sensor } m \text{ sampled} \end{cases}$$

$$\beta^m = \beta_{temp}^m / \sum_{m=1}^{l} \beta_{temp}^m$$

where β_0^m represents the precision of the m-th LF and the following law of conservation of information should be fulfilled:

$$\sum_{m=1}^{l} \beta_0^m = 1$$

The information-sharing process can be written as:

$$(P_k^m)^{-1} = \beta^m (P_k)^{-1}, (Q_k^m)^{-1} = \beta^m (Q_k)^{-1}$$

where P_k is the covariance matrix and its inverse is known as the information matrix and Q_k is the process noise covariance matrix. According to [26], this matrix can be calculated as:

$$Q_k = \frac{\Delta t}{2} \begin{bmatrix} \left(\sigma_v^2 - \frac{1}{6}\sigma_u^2 \Delta t^2\right) I_{3\times 3} & 0_{3\times 3} \\ 0_{3\times 3} & \sigma_u^2 I_{3\times 3} \end{bmatrix}$$

where Δt is the gyroscope sampling time, σ_v^2 is the variance of the Rate Random Walk (RRW) noise term and σ_u^2 is the variance of the Angular Rate Walk (ARW) noise term.

Assuming that all local estimates are uncorrelated, the global estimate of the covariance matrix and error state, x_k is given by the following optimal fusion:

$$(P_k)^{-1} = \sum_{m=1}^{l} (P_k^m)^{-1}$$

$$x_k = P_k \sum_{m=1}^{l} (P_k^m)^{-1} x_k^m$$

Now it is possible to define the sensitivity factor S^m used for the FDI algorithm:

$$S^m = (x_k^m - x_k)^T (P_k^m + P_k)^{-1} (x_k^m - x_k)$$

When S^m is smaller than a threshold value, then the m-th sensor is considered to be working well, and therefore its output can be used in the optimal fusion. However, if S^m is larger than a threshold value, then the m-th sensor could be having some problems. In this case, global estimates should be obtained without using the output of the m-th sensor. The threshold value can be selected based on a Chi-square distribution and optimized in the experiment for the particular application [24].
For convenience, the UKF implemented in each LF is summarized below [26]:

1. *Initialization*

Determine the set of associated weights for the UKF algorithm:

$$W_0^m = \frac{\lambda}{\lambda + n}, W_0^c = \frac{\lambda}{\lambda + n} + (1 - \alpha^2 + \beta), W_i^m = W_i^c = \frac{1}{2(\lambda + n)}, i = 1, \dots, 2n$$

where n is the dimension of the error state vector, $\lambda = \alpha^2(n + \kappa) - n$ is a scaling parameter, α determines the spread of the sigma points around the error state and is usually set to a small positive value between $10^{-4} \leq \alpha \leq 1$ (e.g. 10^{-3} as suggested in [22] and [25]), κ is a secondary scaling parameter which is set to $3 - n$ minimizing the mean-squared-error up to the fourth order [26] or it is set to 0 (see [22] and [25]) avoiding negative values of κ which can lead to a possibility that the predicted covariance become non-positive semi-definite, and β is used to incorporate prior

knowledge of the distribution of the error state (for Gaussian distributions, $\beta = 2$ is optimal) [25].

Then initialize the attitude quaternion q_0^+, the error state vector $x_0^+ = \left[\delta p_0^{+T}\ b_0^{+T}\right]^T$ and the system covariance P_0^+. If no initial attitude quaternion estimate is available, the identity quaternion is chosen:

$$q_0^+ = [0\ 0\ 0\ 1]^T$$

The error state vector consists of a three-component attitude error vector, represented using a generalized Rodrigues parameters, and gyro bias estimates. The initial attitude error vector is set to zero: $\delta p_0^+ = 0$. The system covariance is a 6×6 matrix, where the upper 3×3 partition corresponds to attitude error angles and the lower 3×3 partition corresponds to gyro error bias.

2. Information-sharing and sigma points calculation

First, check new measurements and calculate information-share fractions, then apply Cholesky decomposition to $\overline{P_k} = P_k + Q_k$ to get N_k ($\overline{P_k} = N_k N_k^T$) and calculate sigma points sharing information among new sampled LFs:

$$\sigma_k^m(i) = \gamma col_i(N_k)/\sqrt{\beta^m},\ i = 1, 2, \dots, n$$

$$\sigma_k^m(i) = -\gamma col_{i-n}(N_k)/\sqrt{\beta^m},\ i = n+1, n+2, \dots, 2n$$

$$\chi_k(0) = x_k^+$$

$$\chi_k^m(i) = \sigma_k^m(i) + x_k^+,\ i = 1, 2, \dots, 2n$$

where $\gamma = \sqrt{n + \lambda}$. Note that the better the precision of the m-th LF, the larger the share factor β^m, the lower the dispersion degree of sigma points $\chi_k^m(i)$. Moreover, note that the Cholesky factorization is applied to $\overline{P_k}$ and not to $\overline{P_k}^m$ reducing the computation burden. Since the next steps of the algorithm are the same for each LF, the superscript m is omitted.

Now the vector $\chi_k(i)$ is partitioned into:

$$\chi_k(i) = \begin{bmatrix} \chi_k^{\delta p}(i) \\ \chi_k^{b}(i) \end{bmatrix}$$

where $\chi_k^{\delta p}$ is from attitude-error part and $\chi_k^{\delta b}$ is from the gyro bias part. The error quaternion corresponding to the sigma points $\delta q_k^+(i) = \left[\delta\rho_k^{+T}(i)\ \delta q_{4_k}^+(i)\right]^T$ is calculated using the inverse transformation from δp to δq:

$$\delta \mathrm{q}_{4k}^+(i) = \frac{-a\left\|\chi_k^{\delta p}(i)\right\|^2 + f\sqrt{f^2 + (1-a^2)\left\|\chi_k^{\delta p}(i)\right\|^2}}{f^2 + \left\|\chi_k^{\delta p}(i)\right\|^2}$$

$$\delta \mathrm{q}_k^{+\mathrm{T}}(i) = f^{-1}[a + \delta \mathrm{q}_{4k}^+(i)]\chi_k^{\delta p}(i),\ i = 1, 2, \ldots, 2n$$

with $a = 1$ and $f = 2(a + 1)$. The sigma point quaternion, generated by multiplying the error quaternion by the current estimate, is given by:

$$q_k^+(0) = q_k^+$$

$$q_k^+(i) = \delta q_k^+(i) \otimes \hat{q}_k^+, \qquad i = 1,2, \ldots, 2n$$

3. Time propagation

Sigma-point quaternions are propagated forward in time using the following equation:

$$q_{k+1}^-(i) = \Omega[\omega_k^+(i)]q_k^+(i), \qquad i = 0, 1, \ldots, 2n$$

with:

$$\Omega(\omega_k^+) = \begin{bmatrix} Z_k & \psi_k^+ \\ -\psi_k^{+\mathrm{T}} & \cos(0.5\|\omega_k^+\|\Delta t) \end{bmatrix}$$

$$Z_k = \cos(0.5\|\omega_k^+\|\Delta t)\, I_3 - [\psi_k^+ \times]$$

$$\psi_k^+ = \sin(0.5\|\omega_k^+\|\Delta t)\, \omega_k^+ / \|\omega_k^+\|$$

where Δt is the sampling interval of the gyro and $\omega_k^+(i)$ are the estimated angular velocities:

$$\omega_k^+(i) = \widetilde{\omega}_k - \chi_k^b(i), \qquad i = 0, 1, \ldots, 2n$$

Then, the propagated error quaternions are determined using the following equation:

$$\delta q_{k+1}^{-}(i) = q_{k+1}^{-}(i) \otimes [q_{k+1}^{-}(0)]^{-1}, \qquad i = 0, 1, \dots, 2n$$

where $q^{-1} = [-p^T \; q_4]^T$ is the inverse quaternion. Finally, the attitude error part of the propagated sigma points are given by:

$$\chi_{k+1}^{\delta p}(0) = 0$$

$$\chi_{k+1}^{\delta p}(i) = f\frac{\delta \mathrm{p}_{k+1}^{-}(i)}{a + \delta \mathrm{q}_{4_{k+1}}^{-}(i)}, \qquad i = 1, 2, \dots, 2n$$

with $\delta q_{k+1}^{-}(i) = \left[\delta \mathrm{p}_{k+1}^{-\mathrm{T}}(i) \;\; \delta \mathrm{q}_{4_{k+1}}^{-}(i)\right]^{\mathrm{T}}$ and the gyro bias part of the propagated sigma points are given by:

$$\chi_{k+1}^{b}(i) = \chi_{k}^{b}(i), \qquad i = 0, 1, \dots, 2n$$

assuming that the gyro bias is constant during the time interval $\Delta t = t_{k+1} - t_k$.
In the same time, the observation estimation is calculated as:

$$g_{k+1}(i) = A[q_{k+1}^{-}(i)] \cdot r_{k+1}, \qquad i = 0, 1, \dots, 2n$$

where r_{k+1} is the known reference vector at time t_{k+1} and A is the attitude matrix in terms of the attitude quaternion:

$$A(q) = \Xi^T(q)\Psi(q)$$

with:

$$\Xi(q) = \begin{bmatrix} q_4 I_3 + [\rho \times] \\ -\rho^T \end{bmatrix}, \qquad \Psi(q) = \begin{bmatrix} q_4 I_3 - [\rho \times] \\ -\rho^T \end{bmatrix}$$

The predicted mean error state, mean observation and covariance are given respectively by:

$$x_{k+1}^{-} = \sum_{i=0}^{2n} W_i^m \chi_{k+1}(i)$$

$$y_{k+1}^{-} = \sum_{i=0}^{2n} W_i^m g_{k+1}(i)$$

$$P_{k+1}^{-} = \sum_{i=0}^{2n} W_i^c [\chi_{k+1}(i) - x_{k+1}^{-}][\chi_{k+1}(i) - x_{k+1}^{-}]^T + Q_k$$

4. *Measurement update*

When new measurements came from the m-th sensor, the innovation can be calculated as:

$$v_{k+1} = \tilde{y}_{k+1} - y_{k+1}^{-}$$

where $\tilde{y}_{k+1}$ is the new attitude measurement in the body frame:

$$\tilde{y}_{k+1} = A(q_{k+1}) r_{k+1} + \nu_{k+1}$$

where ν_{k+1} is the measurement noise vector which satisfies:

$$E\{\nu\} = 0$$

$$E\{\nu\nu^T\} = \sigma^2 I_3$$

Then the innovation covariance, the cross-correlation covariance and the Kalman gain are given respectively by:

$$P_{k+1}^{vv} = \sum_{i=0}^{2n} W_i^c [g_{k+1}(i) - y_{k+1}^{-}] [g_{k+1}(i) - y_{k+1}^{-}]^T + R_{k+1}$$

$$P_{k+1}^{xy} = \sum_{i=0}^{2n} W_i^c [\chi_{k+1}(i) - x_{k+1}^{-}][g_{k+1}(i) - y_{k+1}^{-}]^T$$

$$K_{k+1} = P_{k+1}^{xy} (P_{k+1}^{vv})^{-1}$$

where R_{k+1} is the measurement noise covariance matrix and it is given by:

$$R_{k+1} = diag\left[\sigma_x^2 \; \sigma_y^2 \; \sigma_z^2\right]$$

where $\sigma_x, \sigma_y, \sigma_z$ are the standard deviations on each component of sensor measurement noise vector. Finally, the error state vector and the covariance matrix are updated:

$$x_{k+1}^{+} = x_{k+1}^{-} + K_{k+1} v_{k+1}$$

$$P_{k+1}^{+} = — K_{k+1} P_{k+1}^{vv} K_{k+1}^{T}$$

5. *Fault detection and isolation (FDI)*

Each LF output is checked for fault detection using the FDI algorithm reported above. In case of fault of the m-th sensor, the corresponding LF is isolated and its output is not used in the optimal fusion.

6. *Optimal fusion of covariance matrix and error state vector*

The updated error state vectors and covariance matrices coming from each LF are fused in the MF using the equations reported above.

7. *Attitude quaternion update and error state reset*

The attitude quaternion is updated using the following equation:

$$q_{k+1}^{+} = \delta q_{k+1}^{+} \otimes q_{k+1}^{-}(0)$$

where $\delta q_{k+1}^{+} = \left[\delta \rho_{k+1}^{+\mathrm{T}} \;\; \delta \mathrm{q}_{4_{k+1}}^{+}\right]^{\mathrm{T}}$ is represented by:

$$\delta \mathrm{q}_{4_{k+1}}^{+} = \frac{-a\|\delta \mathrm{p}_{\mathrm{k+1}}^{+}\|^2 + f\sqrt{f^2 + (1-a^2)\left\|\delta \mathrm{p}_{\mathrm{k+1}}^{+}\right\|^2}}{f^2 + \left\|\delta \mathrm{p}_{\mathrm{k+1}}^{+}\right\|^2}$$

$$\delta \mathrm{q}_{k+1}^{+} = f^{-1}\left[a + \delta \mathrm{q}_{4_{k+1}}^{+}\right]\delta \mathrm{p}_{\mathrm{k+1}}^{+}$$

with $x_{k+1}^{+} = \left[\delta \mathrm{p}_{\mathrm{k+1}}^{+\mathrm{T}} \;\; \mathrm{b}_{\mathrm{k+1}}^{+\mathrm{T}}\right]^{\mathrm{T}}$.

Finally, the attitude error part of the error state vector, $\delta \mathrm{p}_{\mathrm{k+1}}^{+}$ is reset to zero for the next propagation.

6.2. Filter Tuning

To get a good performance of the filter, it has to be tuned appropriately. The tuning factors of the filter include initial state error covariance P_0, process noise covariance Q, and measurement noise covariance R. Each tuning factor has its role in the filtering process. P_0 determines how fast the estimator converges initially and has no responsibility for the filter performance in the steady state. Q and R determines the tradeoff between the rapid tracking the state variations under the disturbance noise and the filtering of the measurement noise. In addition, Q and R also determines the filter stability in the steady state. The convergence speed is one of many factors that are used in evaluation of the filter performance in real-time. To make a filter converge rapidly, P_0 or Q have to be set large compared to R. However, Q and R affects the steady state performance of the filter [27]. Also the parameters α, β and κ can be considered as tuning parameters. Thus, several simulations are required to properly hand-tune the filter for best performance. An adaptive FUKF is not considered because of the limited on-board computational power.

6.3. Simulations

Simulations are performed to validate the effectiveness of the proposed algorithm. The sampling frequency of the sensors are reported in Table 8.

Sensor	Sampling frequency
Gyroscope	10 Hz
Magnetometer	1 Hz
Sun sensor	5 Hz
Earth horizon sensor	1 Hz
Solar cells	2 Hz

Table 8. Sensors's sampling frequency

The four attitude sensor measurements are considered asynchronous and the information sharing factors are chosen according to sensors' precision and considering the constraint that the sum is equal to one. In Table 9, the filter tuning parameters and

matrices values are used in simulations are reported. ALMASat-EO orbital parameters are considered in these simulation and they were reported in Table 1.

Simulation Parameters	*Value*
Covariance matrix	$P = \mathrm{diag}([100^2 I_{3\times3}\ I_{3\times3}])$
Process noise covariance matrix	$Q = diag([0.005 I_{3\times3}\ 10^{-5} I_{3\times3}])$
Measurement noise matrix	$R_{sun} = diag([0.0005^2\ 0.0017^2\ 0.0017^2])$ $R_{earth} = diag([0.0012^2\ 0.0017^2\ 0.0014^2])$ $R_{mag} = diag([0.0021^2\ 0.0030^2\ 0.0026^2])$ $R_{cell} = diag([0.0138^2\ 0.0253^2\ 0.0143^2])$
UKF parameters	$\alpha = 10^{-3}, \beta = 2, \kappa = 0$

Table 9. FUKF tuning parameters

The Sun sensor is switched on only when the satellite is three-axis stabilized; the magnetometer measurement is always available; the Earth horizon reading is available if the Earth is in the sensor's FOV (see 3.7 and Figure 36) and the solar cells readings are available if the satellite is not in eclipse (see Figure 35).

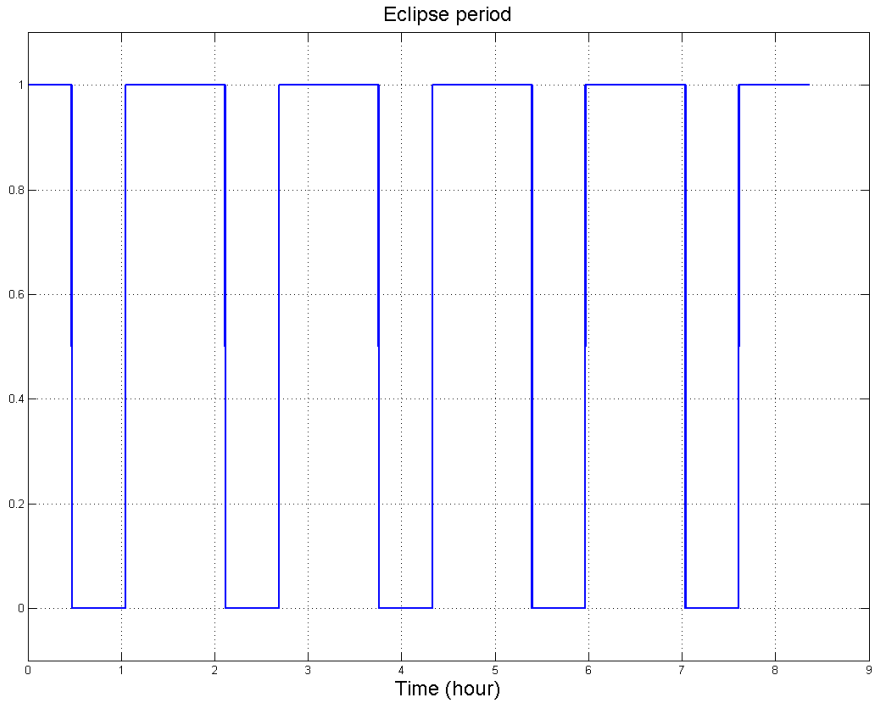

Figure 35. Eclipse periods. The satellite is in eclipse when the value is equal to zero.

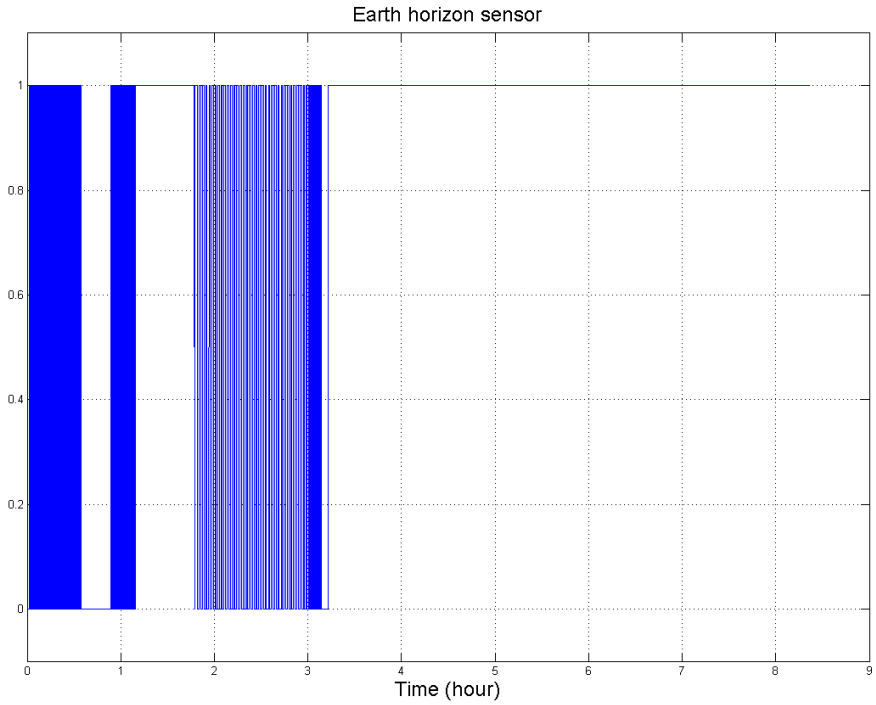

Figure 36. Earth in the horizon sensor FOV. The value is equal to one when the Earth is in the sensor FOV

First simulations showed that the filter estimation diverges when the magnetometer reading is the only available attitude measurement. This is the case when the Earth is not in the horizon sensor's FOV and the satellite is in eclipse. Thus, in these time periods, the attitude estimation filter is switched off to avoid a wrong attitude estimation reading by the ADCS. Since ALMASat-EO is a nadir pointing satellite, the Earth is always in the horizon sensor's FOV when the satellite is stabilized (see Figure 36); hence, in this mission phase the attitude is always correctly estimated. Other simulations suggested not to consider solar cells measurements, once the satellite is stabilized. In fact, during this phase, the attitude estimation is required to be very accurate and solar cells give a coarse estimation. Moreover, Sun sensors measurements are available and they are much more accurate than solar cells readings. However, in this phase, solar cells can be used as a back-up solution in case of Sun sensors failure.

6.4. Results of simulations

In this section the results of simulations to test the effectiveness of the new attitude determination system are reported in terms of quaternions and Euler angles

(see Appendix B). In particular, the accuracy of attitude estimation is investigated when the satellite is three-axis stabilized. Figure 37 and Figure 38 show the error in the attitude estimation performed by the FUKF in terms of quaternion components and Euler angles. The mean and standard deviation of the error in terms of Euler angles, once the satellite is completely three-axis stabilized are reported in Table 10.

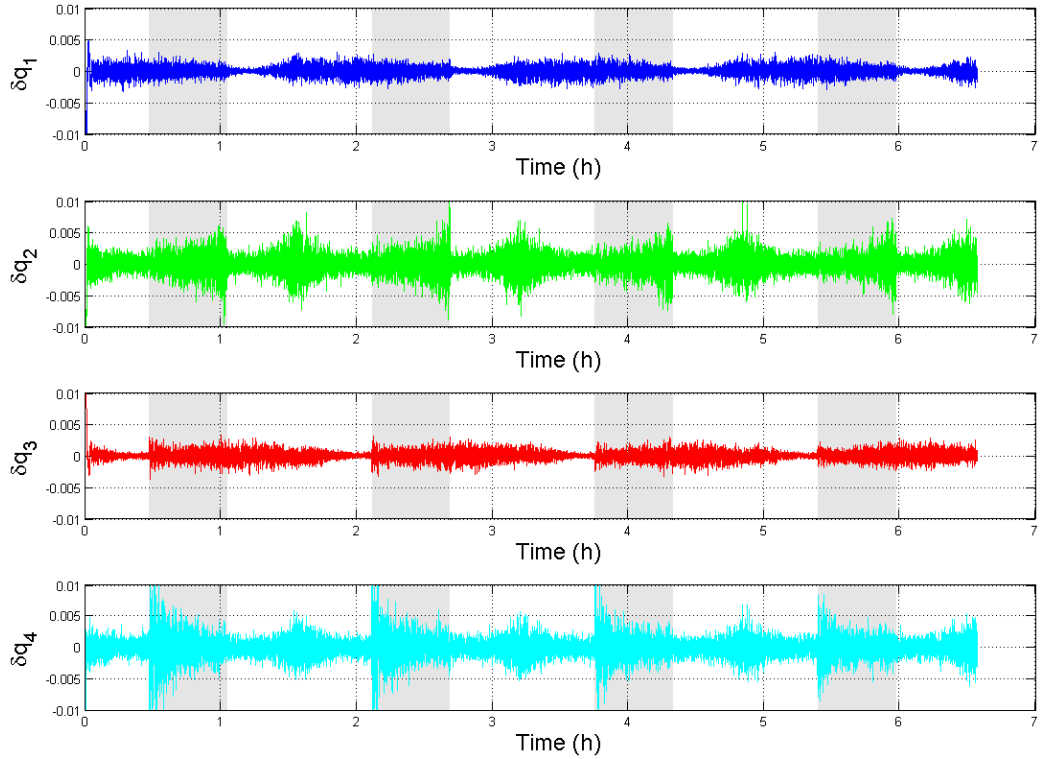

Figure 37. FUKF, attitude quaternion error. The shaded region illustrates the eclipse period.

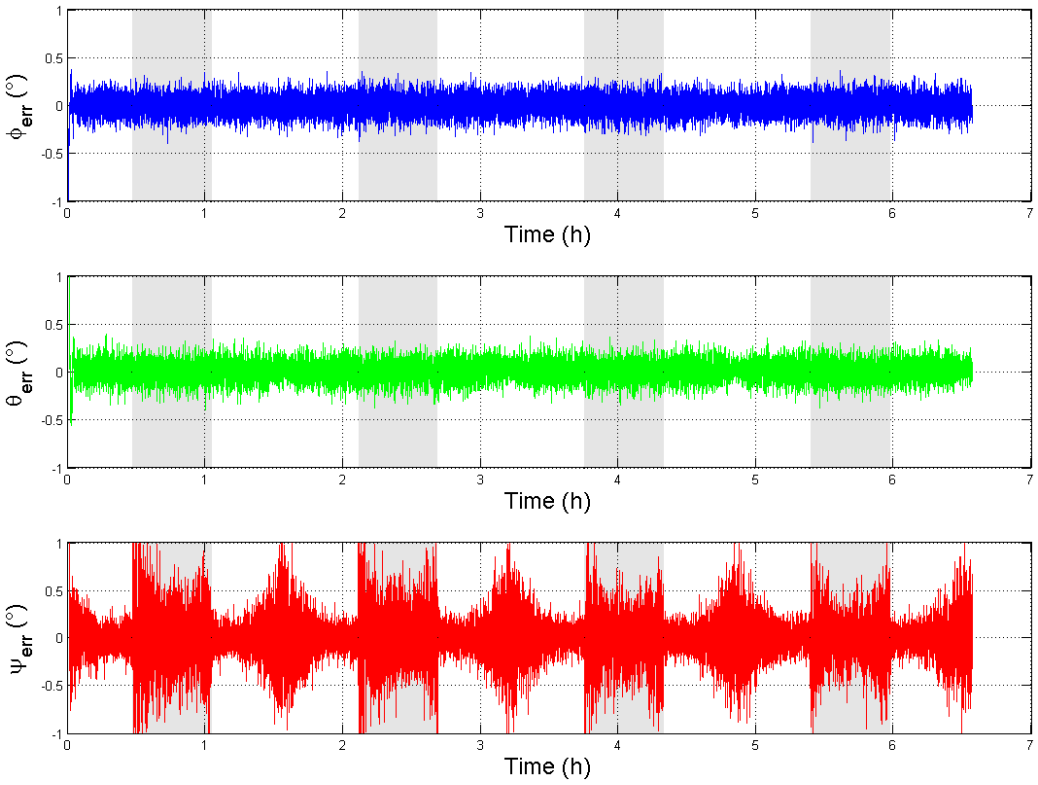

Figure 38. FUKF, Euler angles error. The shaded region illustrates the eclipse period.

Euler angles	$Roll\ \Phi$	$Pitch\ \Theta$	$Yaw\ \Psi$
Mean of the Error	0.0003 °	−0.0560 °	−0.0149 °
Standard deviation of the Error	0.1066 °	0.1013 °	0.2404 °

Table 10. FUKF estimation accuracy in terms of Euler angles

The results show that a good accuracy in attitude estimation is achieved using the FUKF. The angular error is larger for the yaw angle but it is still bounded between $-1°$ and $1°$. Moreover, the eclipse does not significantly affect the attitude estimation accuracy.

In order to fully validate the new attitude determination system, Monte Carlo simulations are performed. 300 simulations are run randomly varying the launch date over the year 2013. The statistical analysis consists of calculating the mean of the estimation error and the standard deviation of the error in terms of the attitude quaternion components $(\sigma_1, \sigma_2, \sigma_3, \sigma_4)$ and the corresponding Euler angles $(\sigma_\phi, \sigma_\theta, \sigma_\psi)$. Moreover, in order to have a statistical parameter which takes into account all four

components of the quaternion and all three Euler angles, the following parameters are calculated:

$$\Sigma_{error}^{q} = \sqrt{\sigma_1^2 + \sigma_2^2 + \sigma_3^2 + \sigma_4^2}$$

$$\Sigma_{error}^{angle} = \sqrt{\sigma_\phi^2 + \sigma_\theta^2 + \sigma_\psi^2}$$

The statistical analysis is performed once the satellite is completely three-axis stabilized and each simulation lasts two orbital periods, T_{orb}. The results are plotted in Figure 39, Figure 40 and Figure 41, in terms of attitude quaternion, and in Figure 42, Figure 43 and Figure 44, in terms of Euler angles.

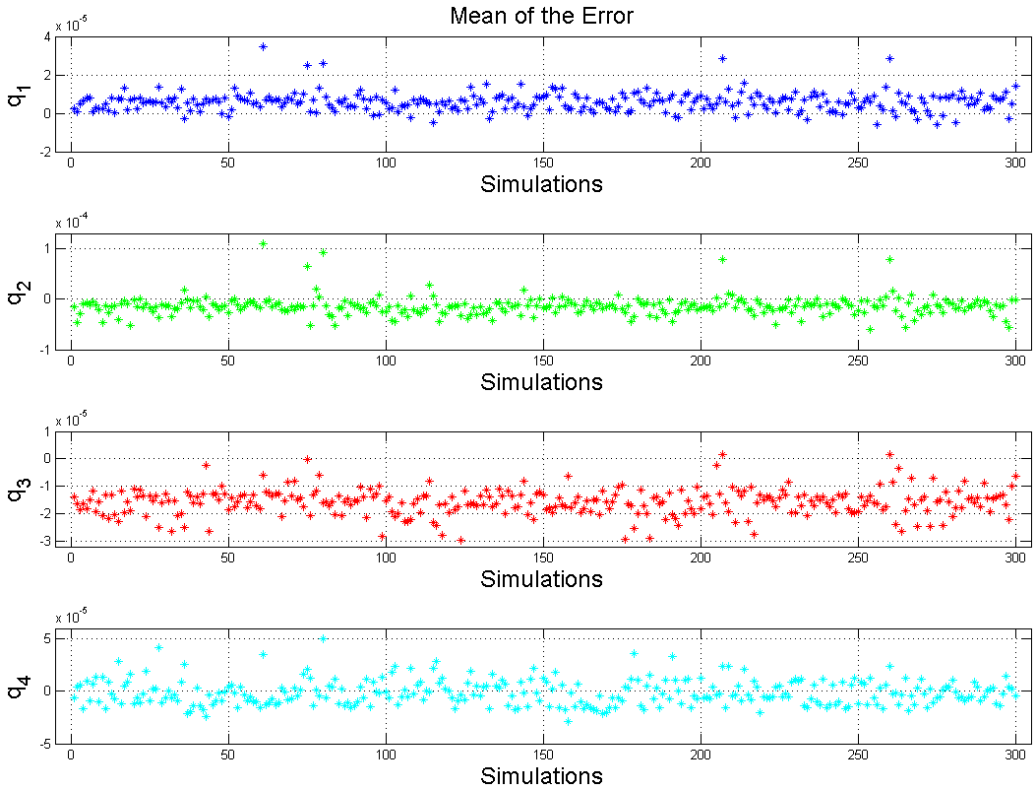

Figure 39. FUKF, Mean of the error in terms of quaternion in Monte Carlo simulations

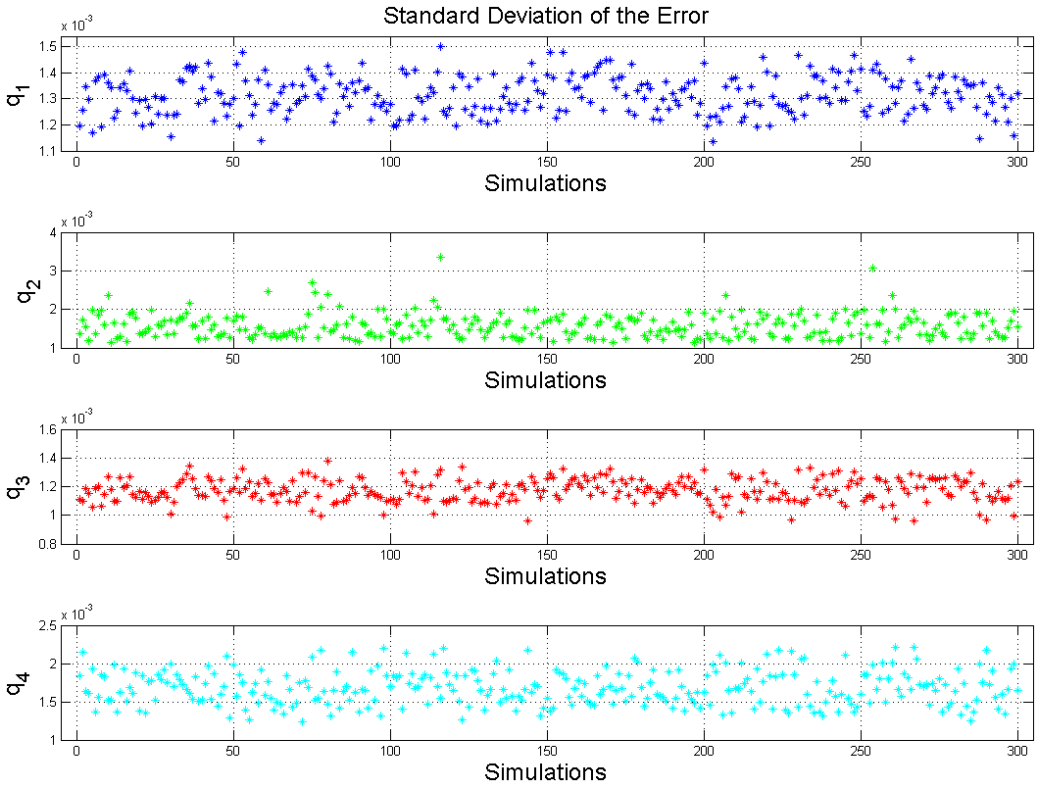

Figure 40. FUKF, Standard deviation of the error in terms of quaternion in Monte Carlo simulations

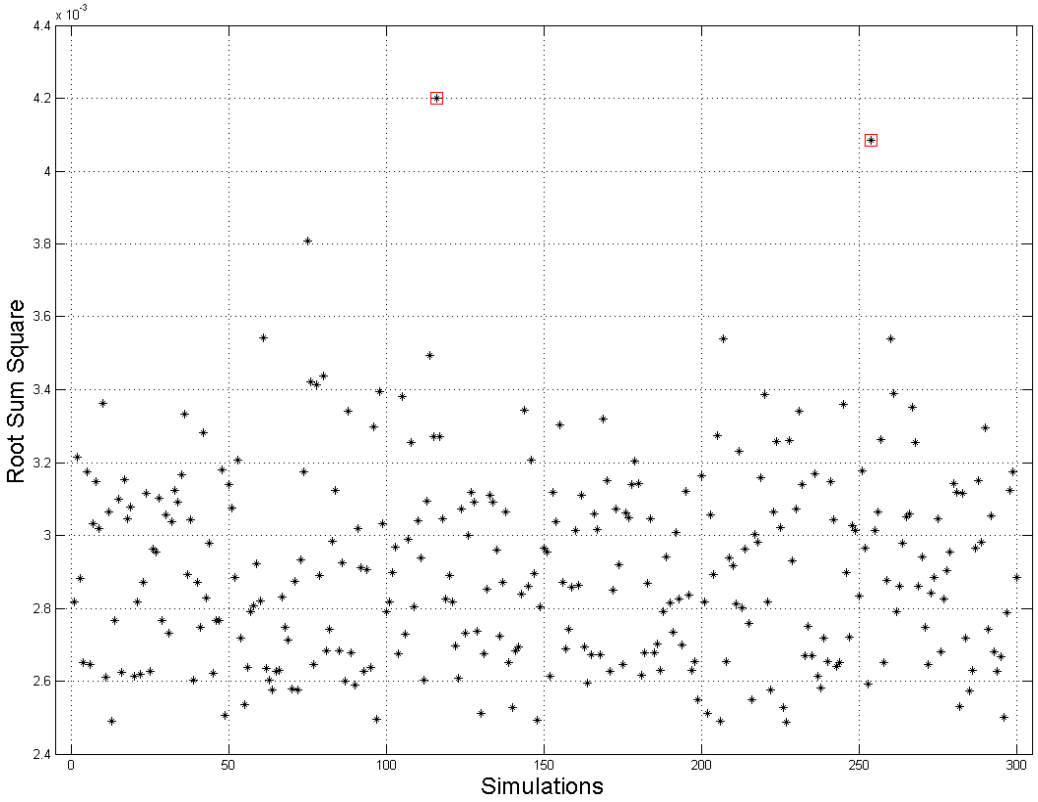

Figure 41. FUKF, Root sum square of the standard deviation of the error in terms of quaternion in Monte Carlo simulations

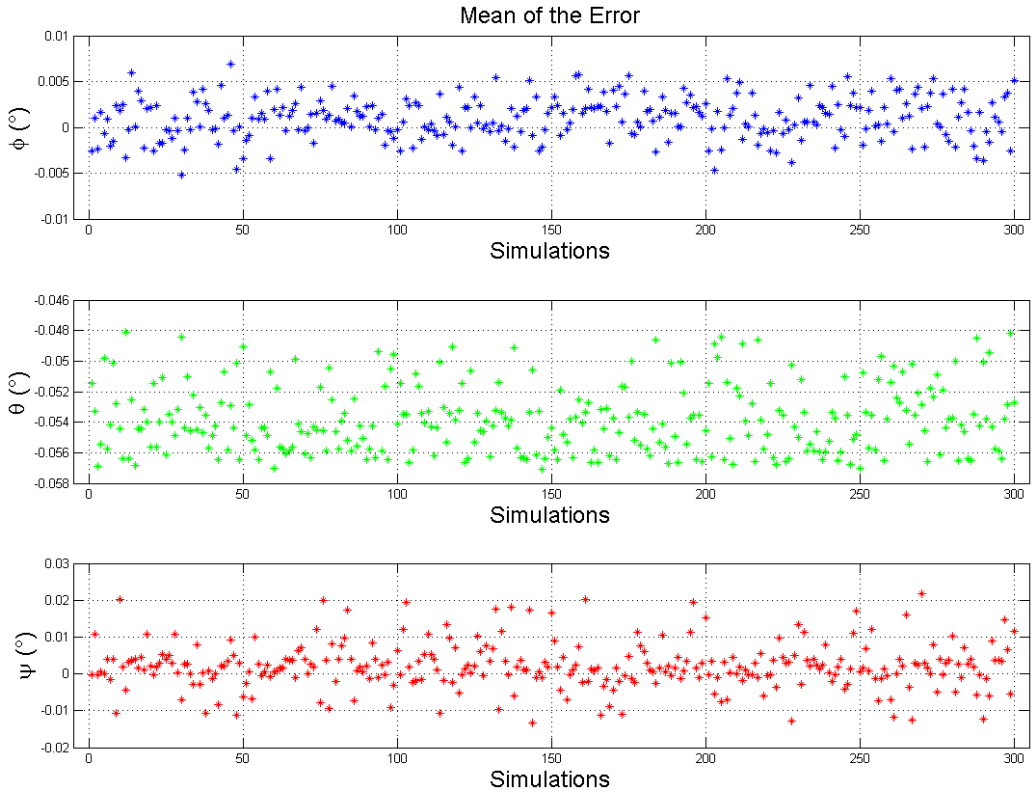

Figure 42. FUKF, Mean of the error in terms of Euler angles in Monte Carlo simulations

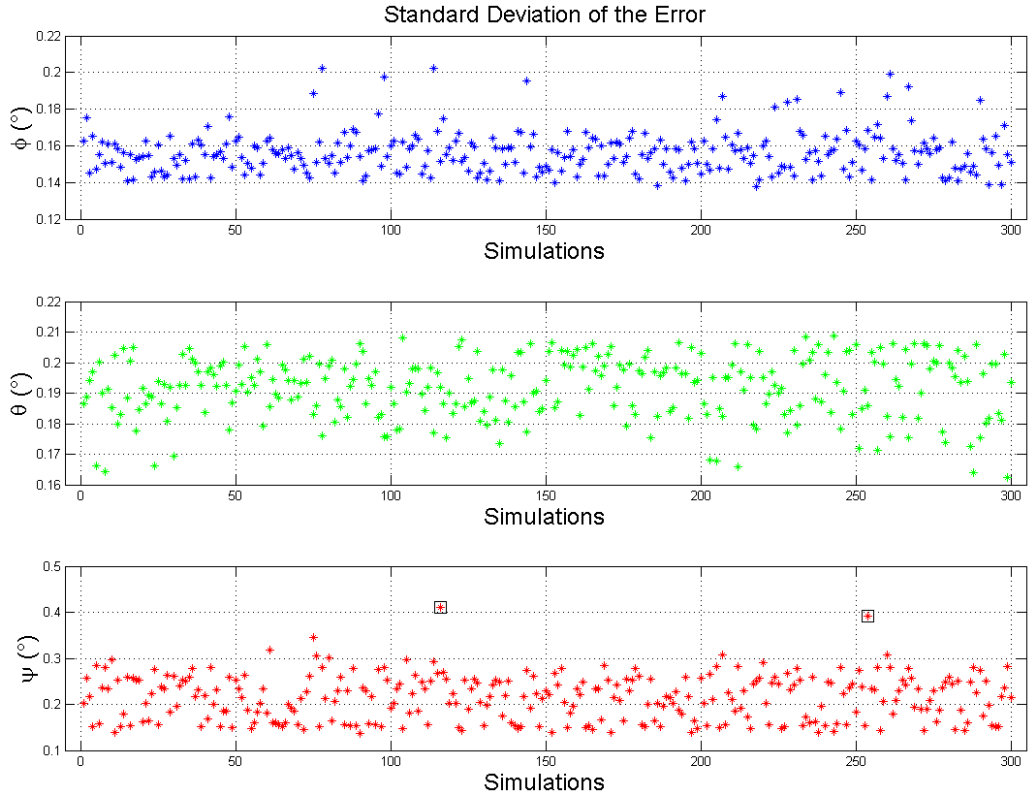

Figure 43. FUKF, Standard deviation of the error in terms of Euler angles in Monte Carlo simulations

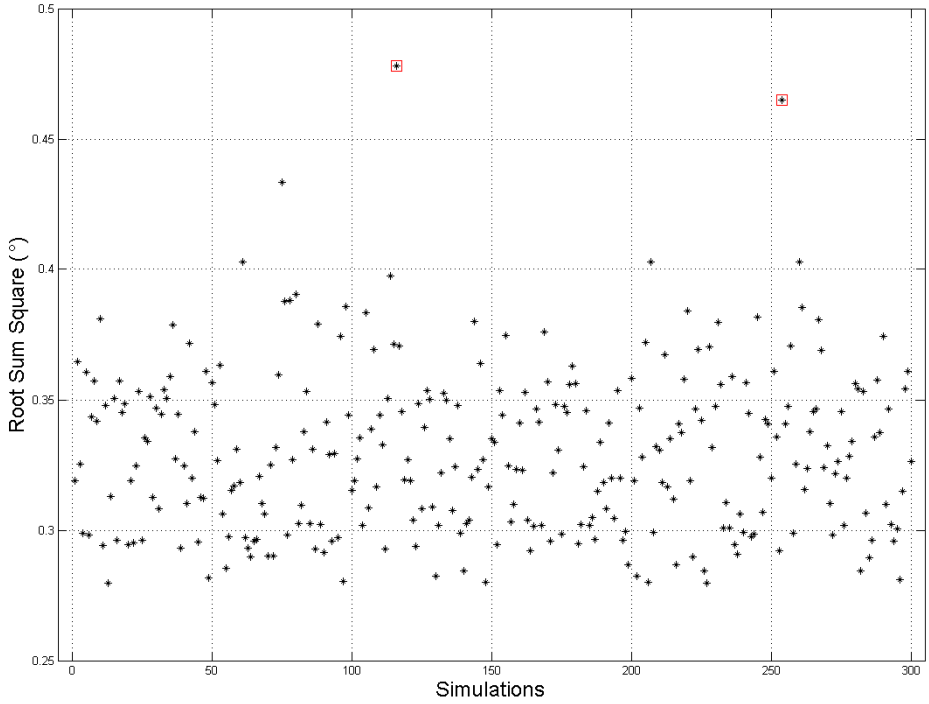

Figure 44. FUKF, Root sum square of the standard deviation of the error in terms of quaternion in Monte Carlo simulations

The results show the good performance of the FUKF in attitude estimation. The values obtained in Monte Carlo simulations are in the same order of magnitude as those reported in Table 10. By looking at the y-axis scale in Figure 43, it is possible to notice that the standard deviation of the error in yaw angle, ψ is larger than the standard deviation of the error in roll and pitch angle, ϕ and θ. This difference is due to the fact that the Earth horizon sensor is poor in yaw, as stated in Table 2. Furthermore, by looking at the particular cases highlighted by the root sum square of the standard deviation of the error in Figure 41 and Figure 44 and by the standard deviation of the error in yaw angle in the bottom panel of Figure 43, where the obtained values are much higher than the average (see the points marked by a rectangle), one can conclude that this is due to alignment between the measured nadir vector and the measured magnetic field vector. Figure 45 shows the time history of the angle, α between the measured nadir vector in body frame, $\tilde{E}_b$ and the measured magnetic field vector in body frame, $\tilde{B}_b$. During the eclipse period, they are the only available attitude reference measurements. Thus, if the corresponding measured vectors are aligned (see Figure 45 in the time range $1.3\,h < t < 1.4\,h$), the attitude estimation is less accurate

(see Figure 46). This is the worst-case for attitude estimation. In this case the estimated yaw angle is not accurate enough for three-axis attitude control.

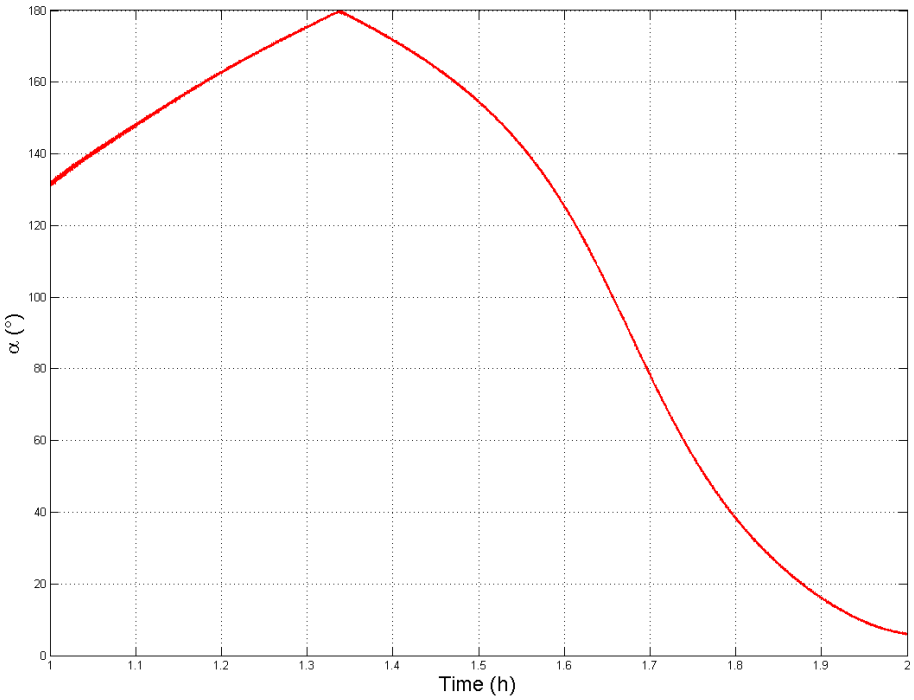

Figure 45. Time history of the angle between the measured nadir vector in body frame and the measured magnetic field vector in body frame

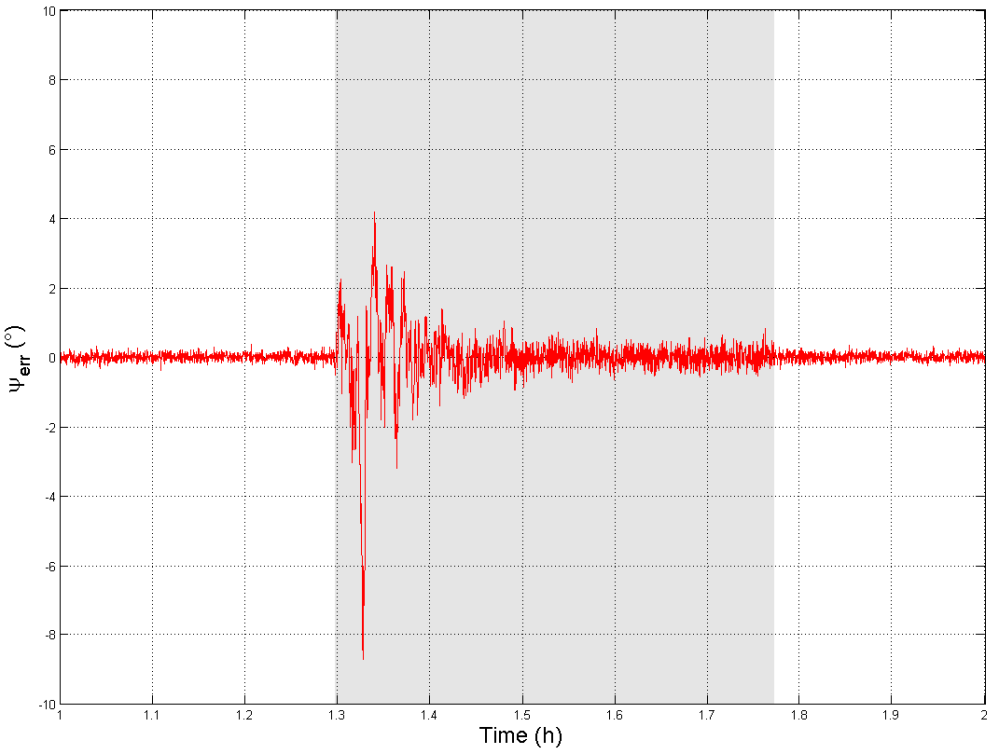

Figure 46. Time history of the error in the yaw angle, ψ. The shaded region illustrates the eclipse period.

7. Conclusion and future work

The results from the simulations clearly show that the mission requirements can be fulfilled in terms of angular rate and attitude estimation using the proposed solutions.

Monte Carlo verification of the EKF for angular rate estimation using solar cells output currents offered important indications for software and hardware implementations. They have been tested by means of simulations and showed the benefits on angular rate estimation. A first arrangement of the solar cells on the satellite has been designed.

The utility in fusing the various sensors measurements to estimate the attitude has been demonstrated by simulating the performance of the FUKF using ALMASat-EO orbital parameters. Monte Carlo simulations are also performed to fully validate the FUKF.

The MATLAB/Simulink simulation model has been improved by adding the solar cells, gyroscope and hysteresis rods model.

In order to have an accurate result of the solar cells performance used to estimate the satellite angular velocity, they need to be tested. In this way a calibration curve of the current versus the angle of incidence of solar rays can be obtained. Moreover, testing the current readings, the minimum value of short-circuit current that can be distinguished from the noise can be defined.

An experimental characterization is also required to check the performance of the gyroscope. A method to cancel out the initial gyro bias error needs to be identified and tested to reach the expected accuracy in angular rate measurement.

Hysteresis rods need to be experimentally tested as described in [16] to calculate accurately their magnetic parameters and influence on the overall satellite system.

The ultimate goal could be to implement the FUKF and the algorithm to reconstruct the Sun position using solar cell measurements on a microcontroller and running the algorithms in hardware-in-the-loop simulation to have more realistic performance information.

Appendix A

AZURSPACE
SOLAR POWER GMBH

28% Triple Junction GaAs Solar Cell

Type: TJ Solar Cell 3G28C

More than 1 million 3G28C cells delivered

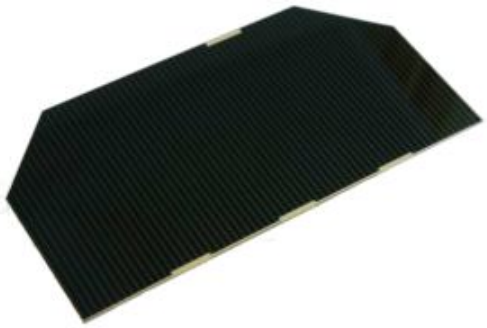

This cell type is a GaInP/GaAs/Ge on Ge substrate triple junction solar cell (efficiency class 28%).
The cell is equipped with an integrated bypass diode, which protects the adjacent cell in the string.

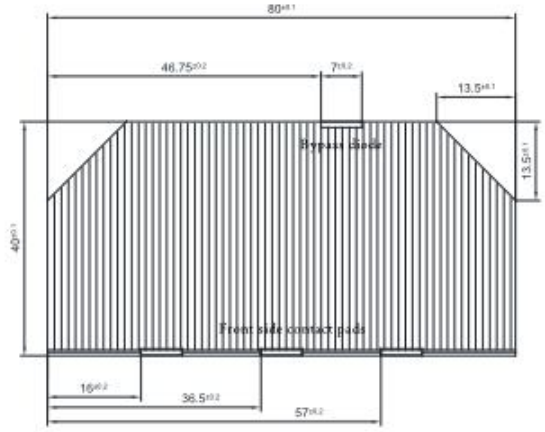

3G28C

Space

28% Triple Junction GaAs Solar Cell
Type: TJ Solar Cell 3G28C

Design and Mechanical Data

Base Material	GaInP/GaAs/Ge on Ge substrate
AR-coating	TiO_x/Al_2O_3
Dimensions	40 x 80 mm ± 0.1 mm
Cell Area	30.18 cm^2
Average Weight	≤ 86 mg/cm^2
Thickness (without contacts)	150 ± 20 µm
Contact Metallization Thickness (Ag/Au)	4 – 10 µm
Grid Design	Grid system with 3 contact pads

Electrical Data

		BOL	2,5E14	5E14	1E15
Average Open Circuit V_{oc}	[mV]	2667	2560	2534	2480
Average Short Circuit I_{sc}	[mA]	506.0	500.9	500.9	485.8
Voltage at max. Power V_{mp}	[mV]	2371	2276	2229	2205
Current at max. Power I_{mp}	[mA]	487.0	482.1	472.4	457.8
Average Efficiency η_{bare} (1367 W/m^2)	[%]	28.0	26.6	25.5	24.5
Average Efficiency η_{bare} (1353 W/m^2)	[%]	28.3	26.9	25.8	24.7

Standard: CASOLBA 2005 (05-20MV1, etc); Spectrum: AMO WRC = 1367 W/m^2; T = 28 °C

Acceptance Values

Voltage V_{op}	2300 mV	
Min. average current $I_{op\ avg}$ @ V_{op}	485 mA	(higher I_{op} on demand)
Min. individual current $I_{op\ min}$ @ V_{op}	455 mA	

Shadow protection

Integrated protection diode T = 25°C ± 3°C	$V_{forward}$ (605 mA) ≤ 2.5 V $I_{reverse}$ (2.8 V) ≤ 100µA

Temperature Gradients (25°C - 80°C)

			BOL	2,5E14	5E14	1E15
Open Circuit Voltage	$\Delta V_{oc}/\Delta T\uparrow$	[mV/°C]	- 6.0	- 6.4	- 6.2	- 6.3
Short Circuit Current	$\Delta I_{sc}/\Delta T\uparrow$	[mA/°C]	0.32	0.33	0.31	0.39
Voltage at max. Power	$\Delta V_{mp}/\Delta T\uparrow$	[mV/°C]	- 6.1	- 6.8	- 6.3	- 6.4
Current at max. Power	$\Delta I_{mp}/\Delta T\uparrow$	[mA/°C]	0.28	0.36	0.20	0.29

Threshold Values

Absorptivity	≤ 0.91 (with CMX 100 AR)
Pull Test	> 1.6 N at 45° welding test (with 12.5µm Ag stripes)

3G28C

Issue date:
2012-04-17

HNR 0002490-00-02
Page 2 of 2

AZUR SPACE Solar Power GmbH
Theresienstr. 2
74072 Heilbronn
phone: +49 7131 67 2603
telefax: +49 7131 67 2727
e-mail: info@azurspace.com
website: www.azurspace.com

MANAGEMENTSYSTEM
DIN EN ISO 9001:2000
DIN EN ISO14001:2005
OHSAS 18001:1999
DQS certificated. Reg. 052403

Space

Triaxial Inertial Sensor with Magnetometer

ADIS16400/ADIS16405

FEATURES

- Triaxial, digital gyroscope with digital range scaling
  - ±75°/sec, ±150°/sec, ±300°/sec settings
  - Tight orthogonal alignment, <0.05°
- Triaxial, digital accelerometer, ±18 *g*
- Triaxial, digital magnetometer, ±2.5 gauss
- Autonomous operation and data collection
  - No external configuration commands required
  - 220 ms start-up time
  - 4 ms sleep mode recovery time
- Factory-calibrated sensitivity, bias, and axial alignment
  - ADIS16400 calibration temperature: +25°C
  - ADIS16405 calibration temperature range: −40°C to +85°C
- SPI-compatible serial interface
- Embedded temperature sensor
- Programmable operation and control
  - Automatic and manual bias correction controls
  - Bartlett-window FIR length, number of taps
  - Digital I/O: data-ready, alarm indicator, general-purpose
  - Alarms for condition monitoring
  - Sleep mode for power management
  - DAC output voltage
  - Enable external sample clock input up to 1.2 kHz
  - Single-command self-test
- Single-supply operation: 4.75 V to 5.25 V
- 2000 *g* shock survivability
- Operating temperature range: −40°C to +105°C

APPLICATIONS

- Unmanned aerial vehicles
- Platform control
- Digital compassing
- Navigation

FUNCTIONAL BLOCK DIAGRAM

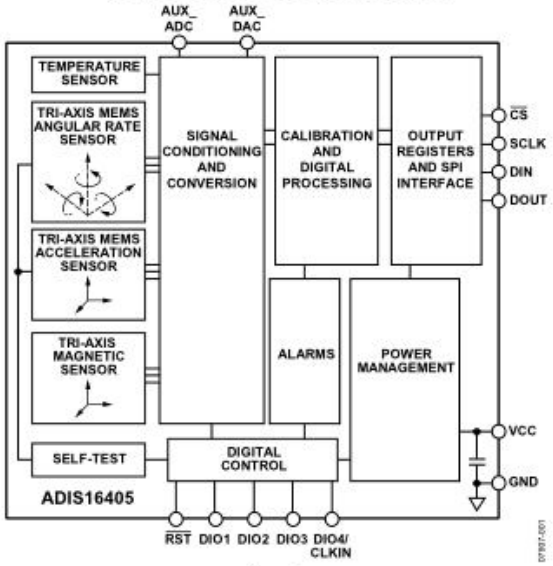

Figure 1.

GENERAL DESCRIPTION

The ADIS16400/ADIS16405 *i*Sensor® products are complete inertial systems that include a triaxal gyroscope, a triaxial accelerometer, and a triaxial magnetometer. The ADIS16400/ADIS16405 combine industry-leading *i*MEMS® technology with signal conditioning that optimizes dynamic performance. The factory calibration characterizes each sensor for sensitivity, bias, alignment, and linear acceleration (gyroscope bias). As a result, each sensor has its own dynamic compensation for correction formulas that provide accurate sensor measurements over a temperature range of −40°C to +85°C. The magnetometers employ a self-correction function to provide accurate bias performance over temperature, as well.

The ADIS16400/ADIS16405 provide a simple, cost-effective method for integrating accurate, multi-axis inertial sensing into industrial systems, especially when compared with the complexity and investment associated with discrete designs. All necessary motion testing and calibration are part of the production process at the factory, greatly reducing system integration time. Tight orthogonal alignment simplifies inertial frame alignment in navigation systems. An improved serial peripheral interface (SPI) and register structure provide faster data collection and configuration control. By using a compatible pinout and the same package as the ADIS1635x and ADIS1636x families, upgrading to the ADIS16400/ADIS16405 requires only firmware changes to accommodate additional sensors and register map updates.

These compact modules are approximately 23 mm × 23 mm × 23 mm and provide a flexible connector interface that enables multiple mounting orientation options.

Rev. B

One Technology Way, P.O. Box 9106, Norwood, MA 02062-9106, U.S.A.
Tel: 781.329.4700 www.analog.com
Fax: 781.461.3113

SPECIFICATIONS

T_A = −40°C to +85°C, VCC = 5.0 V, angular rate = 0°/sec, dynamic range = ±300°/sec, ±1 *g*, unless otherwise noted.

Table 1.

Parameter	Test Conditions	Min	Typ	Max	Unit
GYROSCOPES					
Dynamic Range		±300	±350		°/sec
Initial Sensitivity	Dynamic range = ±300°/sec	0.0495	0.05	0.0505	°/sec/LSB
	Dynamic range = ±150°/sec		0.025		°/sec/LSB
	Dynamic range = ±75°/sec		0.0125		°/sec/LSB
Sensitivity Temperature Coefficient	ADIS16400: −40°C ≤ T_A ≤ +85°C		±250		ppm/°C
	ADIS16405: −40°C ≤ T_A ≤ +85°C		±40		ppm/°C
Misalignment	Axis-to-axis, Δ = 90° ideal		±0.05		Degrees
	Axis-to-frame (package)		±0.5		Degrees
Nonlinearity	Best fit straight line		0.1		% of FS
Initial Bias Error	1 σ		±3		°/sec
In-Run Bias Stability	1 σ, SMPL_PRD = 0x01		0.007		°/sec
Angular Random Walk	1 σ, SMPL_PRD = 0x01		2.0		°/√hr
Bias Temperature Coefficient	ADIS16400: −40°C ≤ T_A ≤ +85°C		±0.025		°/sec/°C
	ADIS16405: −40°C ≤ T_A ≤ +85°C		±0.01		°/sec/°C
Linear Acceleration Effect on Bias	Any axis, 1 σ (MSC_CTRL, Bit 7 = 1)		0.05		°/sec/*g*
Bias Voltage Sensitivity	VCC = 4.75 V to 5.25 V		0.32		°/sec/V
Output Noise	±300°/sec range, no filtering		0.9		°/sec rms
Rate Noise Density	f = 25 Hz, ±300°/sec, no filtering		0.05		°/sec/√Hz rms
3 dB Bandwidth			330		Hz
ACCELEROMETERS					
Dynamic Range		±18			*g*
Initial Sensitivity		3.285	3.33	3.38	mg/LSB
Sensitivity Temperature Coefficient	ADIS16400: −40°C ≤ T_A ≤ +85°C		±120		ppm/°C
	ADIS16405: −40°C ≤ T_A ≤ +85°C		±50		ppm/°C
Misalignment	Axis-to-axis, Δ = 90° ideal		0.2		Degrees
	Axis-to-frame (package)		±0.5		Degrees
Nonlinearity	Best fit straight line, ±17 *g*		0.1		% of FS
Initial Bias Error	1 σ		±50		*mg*
In-Run Bias Stability	1 σ		0.2		*mg*
Velocity Random Walk	1 σ		0.2		m/sec/√hr
Bias Temperature Coefficient	ADIS16400: −40°C ≤ T_A ≤ +85°C		±1.35		*mg*/°C
	ADIS16405: −40°C ≤ T_A ≤ +85°C		±0.3		*mg*/°C
Bias Voltage Sensitivity	VCC = 4.75 V to 5.25 V		2.5		*mg*/V
Output Noise	No filtering		9		*mg* rms
Noise Density	No filtering		0.5		*mg*/√Hz rms
3 dB Bandwidth			330		Hz
MAGNETOMETER					
Dynamic Range		±2.5	±3.5		gauss
Initial Sensitivity	25°C	0.49	0.5	0.51	mgauss/LSB
Sensitivity Temperature Coefficient	25°C, 1 σ		600		ppm/°C
Axis Nonorthogonality	25°C, axis-to-axis		0.25		Degrees
Axis Misalignment	25°C, axis-to-base plate and guide pins		0.5		Degrees
Nonlinearity	Best fit straight line		0.5		% of FS
Initial Bias Error	25°C, 0 gauss stimulus		±4		mgauss
Bias Temperature Coefficient			0.5		mgauss/°C
Output Noise	25°C, no filtering		1.25		mgauss rms
Noise Density	25°C, no filtering, rms		0.066		mgauss/√Hz
3 dB Bandwidth			1540		Hz

Appendix B

The parameterization of the attitude is used to describe the orientation of a body-fixed reference system frame with respect to an orbital reference system or an ECI reference system.

Let us consider an orthogonal, right-handed triad $\hat{u}$, $\hat{v}$, $\hat{w}$ of unit vectors fixed in the body reference system, such that:

$$\hat{u} \times \hat{v} = \hat{w}$$

It is clear that specifying the components of $\hat{u}$, $\hat{v}$, $\hat{w}$ along the three axes of the orbital or ECI reference system will fix the orientation completely. This requires nine parameters which can be regarded as the elements of a 3×3 matrix, A, called attitude matrix:

$$A = \begin{bmatrix} u_1 & u_2 & u_3 \\ v_1 & v_2 & v_3 \\ w_1 & w_2 & w_3 \end{bmatrix}$$

Each of these elements is the cosine of the angle between a body unit vector and a reference axis; u_1, for example, is the cosine of the angle between $\hat{u}$ and the reference 1-axis. For this reason, A is also referred as the direction cosine matrix (DCM). The elements of DCM are not all independent. For example, the fact that $\hat{u}$ is a unit vector requires:

$$\hat{u}_1^2 + \hat{u}_2^2 + \hat{u}_3^2 = 1$$

and the orthogonality of $\hat{u}$ and $\hat{v}$ means that:

$$u_1 v_1 + u_2 v_2 + u_3 v_3 = 0$$

These relationships can be summarized by the statement that the product of A and its transpose is the identity matrix:

$$AA^T = I \;\rightarrow\; A^{-1} = A^T$$

This means that A is a real orthogonal matrix. Also, the determinant of A is defined as:

$$\det(A) = \hat{u} \cdot (\hat{v} \times \hat{w})$$

and since $\hat{u}$, $\hat{v}$, $\hat{w}$ is a right-handed triad, $\det(A) = 1$. Thus, A is a proper real orthogonal matrix which maps vectors from the reference frame to the body frame preserving the lengths of vectors and the angles between them, and hence, it represents a rotation.

It can be also shown that A has at least one eigenvector with eigenvalue unity. That is, there exists a unit vector, $\hat{e}$ that is unchanged by A:

$$A\hat{e} = \hat{e}$$

The vector $\hat{e}$ has the same components along the body axes and the reference axes. Thus, $\hat{e}$ is a vector along the axis of rotation. The existence of $\hat{e}$ demonstrates the Euler's theorem: the most general displacement of a rigid body with one point fixed is a rotation about some axis.

Other parameterization, as summarized in Table 11 [4], may be more convenient than the DCM for specific applications. In the simulator, the attitude is described and propagated using the Euler symmetric parameters, also known as quaternions, which are also used for attitude estimation. Euler angles are also used, especially during the three-axis spacecraft control.

Parameterization	**Notation**	**Advantages**	**Disadvantages**	**Common Applications**
Direction Cosine Matrix	A	No singularities No trigonometric functions Convenient product rule for successive rotations	Six redundant parameters	In analysis, to transform vectors from one reference frame to another
Euler axis/angle	$\hat{e}$, Φ	Clear physical interpretation	One redundant parameter Axis undefined when $\sin\Phi = 0$ Trigonometric functions	Commanding slew maneuvers

Euler symmetric parameters (Quaternion)	q_1, q_2, q_3, q_4 $\|q\|$	No singularities No trigonometric functions Convenient product rule for successive rotations	One redundant parameter No obvious physical interpretation	Onboard inertial navigation
Gibbs vector	g	No redundant parameters No trigonometric functions Convenient product rule for successive rotations	Infinite for 180° rotation	Analytic studies
Euler angles	ϕ, θ, ψ	No redundant parameters Physical interpretation is clear in some cases	Trigonometric functions Singularity at some angle value No convenient product rule for successive rotations	Analytic studies Input/Output onboard attitude control of 3-axis stabilized spacecraft

Table 11. Alternative Representations of Three-Axis Attitude

A parameterization of the DCM in terms of quaternion has proved to be quite useful in spacecraft work. Quaternions were first devised by William Rowan Hamilton, a 19th century Irish mathematician. They are defined in terms of Euler axis/angle as:

$$q = \begin{bmatrix} q_1 \\ q_2 \\ q_3 \\ q_4 \end{bmatrix} = \begin{bmatrix} p \\ q_4 \end{bmatrix} = \begin{bmatrix} e \sin\frac{\Phi}{2} \\ \cos\frac{\Phi}{2} \end{bmatrix}$$

The quaternion components are not independent but they satisfy the constraint equation of unit norm:

$$\|q\|^2 = qq^T = q_1^2 + q_2^2 + q_3^2 + q_4^2 = 1$$

The DCM can be expressed in terms of quaternion as:

$$A = \begin{bmatrix} q_1^2 - q_2^2 - q_3^2 + q_4^2 & 2(q_1q_2 + q_3q_4) & 2(q_1q_3 - q_2q_4) \\ 2(q_1q_2 - q_3q_4) & -q_1^2 + q_2^2 - q_3^2 + q_4^2 & 2(q_2q_3 + q_1q_4) \\ 2(q_1q_3 + q_2q_4) & 2(q_2q_3 - q_1q_4) & -q_1^2 - q_2^2 + q_3^2 + q_4^2 \end{bmatrix} =$$

$$= (q_4^2 - p^2)I + 2qq^T - 2q_4[q\times]$$

Conversely, the quaternion components can be expressed in terms of the DCM elements as:

$$4q_i^2 = 1 + A_{ii} - Ajj - A_{kk} = 1 - \mathrm{trA} + 2A_{ii}$$

$$4q_4^2 = 1 + A_{ii} + A_{jj} + A_{kk} = 1 - \mathrm{tr}A + 2\mathrm{tr}A$$

$$4q_i q_j = A_{ij} - A_{ji}$$

$$4q_i q_4 = A_{jk} - A_{kj}$$

where $\{i, j, k\}$ is a cyclic permutation of $\{1, 2, 3\}$ and trA denotes the trace of the DCM. The equations above, represent all the four ways to calculate the quaternion components from the DCM. In fact, to minimize numerical inaccuracy, Shepperd's algorithm first compares the rhs of the first two equations to see which of the quaternion components is the largest and then calculates the other components using the other two equations [25]. The sign ambiguity is not a problem because q and $-q$ represents the same attitude since they lead to the same DCM.

Successive rotations can be represented by a simple quaternion multiplication:

$$q'' = q' \otimes q = \begin{bmatrix} q_4' & q_3' & -q_2' & q_1' \\ -q_3' & q_4' & q_1' & q_2' \\ q_2 & -q_1' & q_4' & q_3' \\ -q_1' & -q_2' & -q_3' & q_4' \end{bmatrix} \begin{bmatrix} q_1 \\ q_2 \\ q_3 \\ q_4 \end{bmatrix}$$

The residual rotation of q'' with respect to q', or error quaternion, δq, is obtained such as:

$$\delta q = q'' \otimes (q')^{-1}$$

where $(q')^{-1} = [-q_1 \ -q_2 \ -q_3 \ q_4]$ is the inverse quaternion.

In the simulator control block, Euler angles are also computed from the DCM in order to perform a three-axis stabilization control. The DCM is the result of a rotation sequence which can be expressed as the product of three rotation matrices, with the first rotation matrix on the right and the last on the left:

$$R_{231}(\phi, \psi, \theta) = R_2(\theta) R_3(\psi) R_1(\phi) =$$

$$= \begin{bmatrix} c\theta c\psi & c\theta s\psi c\phi + s\theta s\phi & c\theta s\psi s\phi - s\theta c\phi \\ -s\psi & c\psi c\phi & c\psi s\phi \\ s\theta c\psi & s\theta s\psi c\phi - c\theta s\phi & s\theta s\psi s\phi + c\theta c\phi \end{bmatrix}$$

where c and s indicate the cosine and the sine function respectively. The three rotation matrices are defined as:

$$R_1(\phi) = \begin{bmatrix} 1 & 0 & 0 \\ 0 & c\phi & s\phi \\ 0 & -s\phi & c\phi \end{bmatrix}$$

$$R_2(\theta) = \begin{bmatrix} c\theta & 0 & -s\theta \\ 0 & 1 & 0 \\ s\theta & 0 & c\theta \end{bmatrix}$$

$$R_3(\psi) = \begin{bmatrix} c\psi & 0 & -s\psi \\ 0 & 1 & 0 \\ s\psi & 0 & c\psi \end{bmatrix}$$

The subscript denotes the rotation axis and ϕ, θ, ψ are the roll, pitch and yaw angle respectively. These angles can be calculated from the DCM in the following way:

$$\phi = \tan^{-1} \frac{A_{23}}{A_{22}}$$

$$\theta = \tan^{-1} \frac{A_{31}}{A_{11}}$$

$$\psi = -\sin^{-1} A_{21}$$

Other sequences of Euler angles rotations are possible. Since two successive rotations about a single axis are not allowed, because the product of these rotations is equivalent to a single rotation about this axis, there are only 12 possible axis sequences.

Bibliography

[1] M. Bosco, V. Fabbri, P. Tortora, *'ALMASat-EO Attitude Determination Algorithms: Evaluation, Implementation And Numerical Simulation'*, 8th International ESA Conference on Guidance, Navigation & Control Systems, June 2011.

[2] K. Svartveit, *'Attitude Determination of the NCUBE satellite'* Department of Engineering Cybernetics, June 2003.

[3] J. R. Wertz, W. J. Larson, *'Space Mission Analysis and Design'*, Third Edition, Microcosm press, Springer, New York USA, 1999.

[4] J. R. Wertz, *'Spacecraft Attitude Determination and Control'*, Kluwer Academic Publishers, The Netherlands, 1978.

[5] Claudia C. Meruane Naranjo, *'Analysis and Modeling of MEMS based Inertial Sensors'*, KTH, Stockholm, 2008.

[6] Nelson J., *'The Physics of Solar Cells'*, Imperial College Press, U.K., May 2003.

[7] Liu S., Dougal R. A., *'Dynamic Multiphysics Model for Solar Array'*, IEEE Trans. on Energy Conversion, Vol. 17, No. 2, June 2002.

[8] Sera S., Teodorescu R. Rodriguez P., *PV panel model based on datasheet values'*, IEEE International Symposium on Industrial Electronics, ISIE 2007, 4-7 June 2007.

[9] Xiao W., Dunford W.G., Capel A., *'A novel modeling method for photovoltaic cells'*, IEEE Power Electronics Specialists Conference, Aachen, Germany, 2004.

[10] Bellini A., Bifaretti S., Iacovone V., Cornaro C., *'Simplified Model of a Photovoltaic Module'*, IEEE, September 2009.

[11] F. R. Hoots, R. L. Roehrich, T. S. Kelso, *'Spacetrack Report No. 3'*, Celestrack, 31 December 1988.

[12] V. Fabbri, *'Sistema di determinazione d'assetto S/W Determinatore'*, ALMASat-1 project, Microsatellites and Space Microsystems Laboratory, II Faculty of Engineering, University of Bologna, April 2012.

[13] Bhanderi D., *'Spacecraft Attitude Determination with Earth Albedo Corrected Sun Sensor Measurements'* Ph.D. Thesis, August 2005.

[14] Palli A., *'Analisi Termica del MicroSatellite ALMASat'*, Elaborato Finale di Laurea, II Faculty of Engineering, University of Bologna, 2005.

[15] Jason Tuthill, *'Design and Simulation of a Nano-Satellite Attitude Determination System'*, Thesis, Naval Postgraduate School, Monterrey (California), December 2009.

[16] M. Bosco, *'Passive Magnetic Attitude Control System'* Relazione di Preparazione alla Tesi, II Faculty of Engineering, University of Bologna, 2012.

[17] Oshman Y., Dellus F., *'Spacecraft Angular Velocity Estimation Using Sequential Observations of a Single Directional Vector'* Journal of Spacecraft and Rockets, Vol. 40, No. 2, March-April 2003.

[18] Viscito L., Cerise M. C., *'Rate and Attitude Determination Using Solar Array Currents'* AIAA.

[19] Tortora P., Oshman Y., Santoni F., *'Spacecraft Angular Rate Estimation from Magnetometer Data Only Using an Analytic Predictor'* Journal of Guidance, Control and Dynamics, Vol. 27, No. 3, May-June 2004.

[20] M. Bosco, *'Algoritmi per la determinazione d'assetto'*, Relazione di Tirocinio, II Faculty of Engineering, University of Bologna, 2010.

[21] M. Bosco, *'Studio e Simulazione di Algoritmi di Determinazione d'Assetto per il Microsatellite ALMASat-EO'*, Elaborato Finale di Laurea, II Faculty of Engineering, University of Bologna, 2010.

[22] C. Fan, Z. Meng, G. Zhang, Z. You, *'Federated Sigma Point Filter for Multi-Sensor Attitude and Rate Estimation of Spacecraft'*, Proceedings of SPIE, Vol. 7129 712929, 2008.

[23] J. Bae, Y. Kim, *'Attitude Estimation for Satellite Fault Tolerant System Using Federated Unscented Kalman Filter'*, IJASS 11 (2), 80-86 (2010).

[24] J. Bae, S. Yoon, Y. Kim *'Fault-Tolerant Attitude Estimation for Satellite Using Federated Unscented Kalman Filter'*, Advances in Spacecraft Technologies, Dr J. Hall (Ed.)

[25] M. Ilyas, J. K. Lim, J. G. Lee, C. G. Park, *'Federated Unscented Kalman Filter Design for Multiple Satellites Formation Flying in LEO'*, International Conference on Control, Automation and Systems 2008.

[26] J.L. Crassidis, F.L. Markley *'Unscented Filtering for Spacecraft Attitude Estimation'*, Journal of Guidance, Control, and Dynamics, Vol. 26, No. 4, July-August 2003.

[27] S.-W. Kim, M. Abdelrahman, S.-Y. Park, K.-H. Choi, *'Unscented Kalman Filtering for Spacecraft Attitude and Rate Determination using Magnetometer'*, J. Astron. Space Sci. 26 (1), 31-46 (2009).

[28] Markley F. L., *'Unit Quaternion from Rotation Matrix'*, Journal of Guidance, Control and Dynamics, Vol. 31, No. 2, March-April 2008.

Acknowledgments

I would like to acknowledge Professor Paolo Tortora, the head of the Microsatellite and Space Microsystems Laboratory at the II Faculty of Engineering of the University of Bologna, for his support.

I express my gratitude to MSc Valentino Fabbri, AODCS and GNC engineer at ALMASpace S.r.l., for sharing his knowledge, giving fruitful comments and for the time during my BSc and MSc thesis work.

Furthermore I want to show appreciation to the members of the ALMASat team, especially Alessandro Tambini for the suggestions and the discussions.

Un ringraziamento particolare va inoltre ai miei genitori per il loro supporto economico e morale durante tutto il periodo dei miei studi.

Infine, un riconoscimento va a tutti coloro che hanno incoraggiato le mie scelte universitarie.